OHMIC CONTACTS TO BETA SILICON CARBIDE : ELECTRICAL AND METALLURGICAL CHARACTERIZATIONS

Thesis by

Jen-Sue Chen

In Partial Fulfillment of the Requirements

for the Degree of

Doctor of Philosophy

California Institute of Technology

Pasadena, California 91125

1995

(Defended July 5, 1994)

ACKNOWLEDGMENTS

In my five years at Caltech, I owed too much to too many people for their kindness and help. Among these, I would like to first express my appreciation to my advisor, Professor Marc-Aurele Nicolet, for his support and guidance, as well as providing an inspiring research environment and letting me continually create and kill projects in these years.

I am indebted to Dr. Elzbieta Kolawa for her invaluable discussions in forming this thesis and lots of other "scientific and nonscientific" advice. My gratitude also goes to Dr. Simon Nieh for his help in the very beginning of my Caltech life and in Hughes Research Labs during the summer of 1993. I also sincerely appreciate Dr. Andreas Bächli for his fruitful discussions about the contact resistivity measurement and how to travel in Europe.

I wish to have my special thanks to Carol Garland. Her kindness and encouragement make the electron microscopy lab become my favorite place in Caltech. Without her, the transmission electron micrographs shown in this thesis may mostly disappear.

One of the great things about Caltech is that you can keep bugging people as much as you want. I would like to salute those victims who were more or less bugged by me through out these years. They include Drs. or becoming Drs. Jason *Super* Reid, Tom Workman, Tab Stephens, Wen-Shu Liu, Donald Lie, Xin Sun, Richard Liu, Cho-Jen Tsai, Lawrence Anthony, Dave Lee, Mohit Jain, and Channing Ahn, who claimed that he would do anything for me. Many thanks also to Rob Gorris and Mike Easterbrook for their technical assistance.

Rindge Shima and Ron Ruiz are the two JPL people who have my great appreciation. Ron had helped me on lots of scanning electron microscopy works. Those beautiful SEM pictures shown in this thesis are all his credit. For Rindge, the kindest person I have ever met, there is no word to describe my gratitude to him. It was my real

fortune to know him, and it is my deepest sorrow that he couldn't see me finishing this thesis. His gentleness will always be the warmest memory in my heart.

Organizations which provide support for this thesis include the Army Research Office and LETI in Grenoble, France. I am grateful to Professor Ronald Madar and Laurence Baud for our collaboration on the SiC project and their hospitality when I was in France.

Last but not least, my deepest gratitude goes to my family, especially Mom and Dad, for their love and blessings. It is to them that I dedicate this thesis.

PREFACE

This thesis contains the major part of my work done at Caltech, which is contact metallization of β-SiC. All the material contained in this thesis is published, or accepted for publication, or in preparation for publication. All my publications are listed separately in Appendix I, which gives a comprehesive overview of all the investigations I have carried out at Caltech.

ABSTRACT

Thermally induced reactions between a sputter-deposited Re, Pt or Ta film and a single crystalline (001) β-SiC substrate in vacuum at temperatures from 300 to 1200°C for 30 min or 1 h are investigated by MeV He^{++} backscattering spectrometry, x-ray diffraction, secondary ion mass spectrometry, transmission and scanning electron microscopies. The contact resistivities of the as-deposited and the annealed Pt, Re, and Ta contacts to β-SiC are characterized using circular transmission line.

No reaction between Re and SiC is observed for all annealing conditions. The average grain size of the as-deposited Re film is 220 nm and increases to 280 nm after annealing at 1100°C for 30 min. A strong $\{0001\}_{Re}$ fiber texture is also observed after annealing. The chemical stability of Re thin films on SiC is consistent with an earlier study in the ternary Re-Si-C system which shows that Re and its silicides have tie lines with SiC at 1600°C. This finding also coincides with our calculations of the free energy of reactions from critically assessed thermodynamic data for rhenium silicides and SiC.

Backscattering spectrometry shows that Pt reacts with SiC at 500°C. The product phase identified by x-ray diffraction is Pt_3Si. At 600-900°C, the main reaction product is Pt_2Si but the depth distribution of the Pt atoms changes with annealing temperature. Samples annealed at 500-900°C have a double-layer structure with a silicide surface layer and a carbon-silicide mixed layer below. At 900°C, the phases in the mixed layer become stratified, with a continuous carbon layer in direct contact with the substrate. When the sample is annealed at 1000°C, the surface morphology deteriorates with the formation of some dendrite-like hillocks; both Pt_2Si and PtSi are detected by x-ray diffraction.

The SiC-Pt interaction is resolved at an atomic scale with high-resolution electron microscopy. It is found that the grains of the sputtered Pt film first align themselves preferentially along an orientation of $\{111\}_{Pt}//\{001\}_{SiC}$ without reaction between Pt and SiC. A thin amorphous interlayer then forms at 400°C. At 450°C, a new crystalline phase nucleates discretely at the Pt-interlayer interface and projects into or across the amorphous interlayer towards the SiC, while the undisturbed amorphous interlayer between the newly-formed crystallites maintains its thickness. These nuclei grow extensively down into the substrate region at 500°C and the rest of the Pt film is converted to Pt_3Si.

No significant reaction between Ta and SiC is observed at 800°C or below. At 900°C, the main product phases are Ta_2C and carbon-stabilized Ta_5Si_3. A minor amount of unreacted Ta is also present. After annealing at 1000°C, all the tantalum has reacted; the reaction zone possesses a multilayered structure of β-SiC/TaC/carbon-stabilized Ta_5Si_3/α-Ta_5Si_3/Ta_2C. At 1100°C, the reacted layer has an interface with the SiC substrate that is still quite flat, but has a rough surface due to the formation of macroscopic voids within the reacted layer. The equilibrium products predicted by the phase diagram are TaC and $TaSi_2$. This final state is reached upon annealing at 1200°C for 1 h. At that point, the reacted layer has a laterally very uneven structure and morphology.

Contact resistivities of the as-deposited and annealed Pt, Re, and Ta films on n-type, single-crystalline (001) β-SiC are determined using a circular contact pattern and the method of the circular transmission line. The β-SiC substrates used in the experiment are n-type doped either non-intentionally to a carrier concentration of $\sim 10^{17}$ cm^{-3}, or by nitrogen implantation and annealing to a concentration of 5×10^{19} cm^{-3}. A resistance-network model is developed to derive an analytic expression for the angular dependence of the voltage distribution along the rings when they have a non-negligible resistance. By applying this model, the resistance between two concentric contacts can be extracted and will yield the

correct contact resistivity when one uses the formulae of the circular transmission line model that ignores the finite resistance of the rings.

On the non-intentionally doped β-SiC substrates, Pt contacts are non-ohmic regardless of the heat treatment. The as-deposited Ta and Re contacts are ohmic with contact resistivities of 5×10^{-5} Ωcm^2 and 4×10^{-4} Ωcm^2, respectively. Upon annealing at 500 °C for 30 min, the resistivity of Ta increases slightly while that of Re decreases slightly. Both Ta and Re contacts become non-ohmic by annealing at 900 °C for 30 min.

The as-deposited Ta, Pt, and Re contacts are all ohmic on the nitrogen-implanted β-SiC substrate. The contact resistivity of the as-deposited Ta contact is the lowest and in the order of high 10^{-7} Ωcm^2, stays about the same at 500 °C and degrades to 4.3×10^{-6} Ωcm^2 at 1000 °C. The as-deposited Re contact has the highest contact resistivity of 1×10^{-4} Ωcm^2 but it improves to 1×10^{-5} Ωcm^2 upon annealing at 900 °C. The contact resistivity of the as-deposited Pt contacts is 6×10^{-6} Ωcm^2 and increases to 1×10^{-5} Ωcm^2 at 500 °C. After annealing at 900 °C for 30 min, the Pt contact on the nitrogen-implanted β-SiC is no longer ohmic. The results are compared with the reactions that take place in those systems.

TABLE OF CONTENTS

Acknowledgments ii

Preface iv

Abstract v

Table of Contents viii

Chapter 1 Metal-SiC Contacts - An Introduction 1

1.1 Physical Properties of SiC 1

1.2 Contact Metallurgy 4

1.3 Electrical Characterization 6

References 13

Chapter 2 Experimental Procedures 17

2.1 Metal Deposition and Annealing 17

2.2 Analysis Techniques 18

Chapter 3 Stability of Rhenium Thin Films on Single Crystal (001) β-SiC 19

3.1 Interface Structure 19

3.2 Thermodynamics 25

3.3 Discussion 29

References 30

Chapter 4 Solid-State Reaction of Pt Thin Film With Single-Crystal (001) β-SiC 31

4.1 Reaction Characterization 31

4.2 Thermodynamic Considerations 43

4.3 Formation of Carbon Precipitates 45

4.4 Interdiffusion Between SiC and Pt Upon Annealing 45

4.5 Formation of the Amorphous Interlayer 47

References 48

Chapter 5 Reaction of Ta Thin Film With Single Crystalline (001) β-SiC 49

5.1 Reaction Characterization 49

5.2 Thermodynamic Considerations 60

5.3 Diffusion Path at 1000 °C 62

5.4 Formation of Voids 63

References 64

Chapter 6 Measurement of Contact Resistivity 65

6.1 Contact Resistivity Measurement with Circular Patterns 65

6.2 Effect of the Finite Metal Resistance - A Resistance Network Model 68

6.3 Extracting Contact Resistivity With the $R_{1,sym}$ and $R_{2,sym}$ Obtained From the Resistance Network Model 75

6.4 Contact Resistivity of Re, Pt and Ta Films on n-type β-SiC 79

6.5 Comparison of Contact Resistivity Results with Interfacial Reactions Results 81

References 83

Chapter 7 Further Thoughts 84

Summary and Conclusions 86

Appendix I Work Published by Jen-Sue Chen 88

Appendix II Contact Resistivity Measurement Using a Circular Transmission Line Model of Homogeneous Substrate Sheet Resistance 91

Reference 96

Chapter 1
Metal-SiC Contacts - An Introduction

Silicon carbide (SiC) is one of the most promising semiconductors for high-temperature electronics as well as high-power devices [1]. The main reasons are its high thermal and chemical stability combined with a wide bandgap (see section 1.1). Silicon carbide is also used in fiber-reinforced metal-matrix composites because of its high strength, light weight and superior chemical stability. For both electrical and composites applications, the interface between metal and silicon carbide is of great interest. In electronics, this interface determines the properties of the electrical contact (ohmic or rectifying). In metal-matrix composites, the same interface influences the load transfer between the metal matrix and the silicon carbide reinforcement and affects the mechanical properties of the composites [2, 3]. There exist numerous studies for the reaction between SiC and bulk metals, in connection with metal-matrix composites [4-11]. However, thermal reaction between SiC and thin metal films (on the order of 10 nm to 1 μm) has not been widely studied yet. This thesis is concerned mainly with the solid-state reactions between SiC and thin metal films of submicron scale over a wide temperature range as well as their corresponding electrical characteristics. In this chapter, we first review the general properties of SiC and secondly the development of metal contacts to SiC.

1.1 Physical Properties of SiC

Silicon carbide is a stoichiometric compound with tetrahedral Si-C atomic arrangement. SiC crystallizes in more than hundred different modifications, called polytypes [12]. The many polytypes differ from one another only in the stacking sequence of the hexagonal close-packed double layers of silicon and carbon atoms. Depending on the stacking order, cubic, hexagonal or rhombohedral structures are produced. The polytype of

SiC therefore can be described in terms of the stacking order along the c-axis of the hexagonal frame of reference. The hexagonal close-packed planes are normally labeled A, B and C, indicating the three possible positions for the contiguous planes. The stacking order of the common SiC polytypes are listed in Table 1.1.

Table 1.1 Selected SiC polytypes

shorthand notation	Ramsdell notation	Stacking sequence
β	3C	ABC ABC ...
α	6H	ABCACB ABCACB ...
α	4H	ABAC ABAC ...
α	2H	AB AB AB ...
α	15R	ABCBACABACBCACB ABC...

The most common nomenclature for the SiC polytypes is the Ramsdell notation which is a number followed by a letter. The number is the number of the close-packed layers in a stacking repeat sequence and the letter designates the structure (C: cubic; H: hexagonal, R: rhombohedral). The cubic SiC (3C) is also known as β-SiC. This is the polytype used for the present investigation. All the other polytypes are known as α-SiC.

The applicability of SiC for microelectronics and composites originates from its specific material characteristics. The general physical properties of SiC are tabulated in Table 1.2. This table is compiled from the SiC data base in Ref. 13. References of the individual properties can be found in Ref. 13.

Table 1.2 Physical properties of SiC [13]

Property	type	value	unit	Temp. (°C)
lattice constant	β	a=4.3596	Å	24
	6H	a=3.0806; c=15.1173	Å	24
density	β	3.210	g/cm^3	27
	6H	3.211	g/cm^3	27
thermal expan. coef.	β	2.47	10^{-6} °C^{-1}	20
		~4.5		427
	6H	4.2 (a-axis)	10^{-6} °C^{-1}	427
		4.7 (c-axis)		427
melting point* (decomposes)	β	2830±40	°C	
thermal conductivity	6H	4.9	W cm^{-1} °C^{-1}	27
bandgap	β	2.2	eV	27
	6H	2.86	eV	27
electron mobility	β	900 ($n=10^{16}$)	$cm^2 V^{-1}s^{-1}$	27
	6H	260 ($n=1.5\times10^{17}$)	$cm^2 V^{-1}s^{-1}$	27
hole mobility	6H	50 ($p=10^{17}$)	$cm^2 V^{-1}s^{-1}$	27
saturated electron drift velocity	6H	2×10^7	cm s^{-1}	27
breakdown field	6H	2 - 4×10^6	V cm^{-1}	27
dielectric constant	β	9.72		27
	6H	9.66 (⊥ c-axis)		27
		10.03 (∥ c-axis)		

*$T_{decomposition}$ = 2545±40 °C, in T. B. Massalski, *Binary Alloy Phase Diagrams*, 1990.

1.2 Contact Metallurgy

Studies on the structural evolution of the reaction between SiC and thin metal films (thicknesses of 10 nm to 1 μm) now exist for Ti [14], Nb [7, 15], Ta [15-17], Mo [18], Re [18], Co [20] and Pt [21, 22]. Although this is only a minor part of the transition metals, we may try to discern the general trends. To this end, it is convenient to subdivide the transition metals into early transition metals (including the Sc, Ti, V, Cr groups and Mn), which form stable compounds with both Si and C, and the late transition metals (including Re and the Fe, Co and Ni groups) which form only stable silicides. Table 1.3 lists the existent silicides and carbides for the transition metals of group IVB - VIIIB.

Among these metals, Re takes a unique position in that it is thermodynamically stable with SiC up to at least 1100°C as was established theoretically and confirmed experimentally [19].

Thin Co [20] and Pt [21, 22] films on SiC yield a common structure upon annealing at 1000°C for 2 min for Co and at 500-900°C for 30 min for Pt. The reacted layer adjacent to SiC contains amorphous or graphitic carbon, mixed with silicides, possibly in a stratified fashion. The presence of a carbonaceous layer in these contacts will certainly affect their mechanical and electrical applications.

For the thermal reaction of thin films of the early transition metals with SiC, an obvious similarity between Nb and Ta is the appearance of a multilayered structure of the general form $SiC/MC_m/M_xSi_yC_z/MC_n/M$, where M=Nb, Ta [7, 15]. This multilayered structure is also observed in our study for Ta [17, Chapter 5]. In the case of Mo, the carbide layer adjacent to the SiC is apparently missing and the $M_xSi_yC_z$ layer is replaced by a Mo-silicide layer [18]. For Ti, the ternary compound is also replaced by Ti-silicide, but it is the carbide layer adjacent to the metal that does not fully develop [16]. These differences may simply be due to an incomplete characterization of the evolution of the reaction and needs substantiated by more detailed studies.

Table 1.3 Transition Metal (IVB - VIIIB) Silicides and Carbides

IV B		**V B**		**VI B**		**VII B**		**VIII B**		**VIII B**		**VIII B**	
Ti 22		V 23		Cr 24		Mn 25		Fe 26		Co 27		Ni 28	
Ti3Si	Ti2C	V3Si	V2C*	Cr3Si	Cr23C6	Mn3Si*	α	α1	(Fe3C)	Co3Si*	(Co3C)	Ni4Si	(Ni3C)
Ti5Si3	TiC	V5Si3*	V4C3-x	Cr5Si3	Cr7C3	Mn5Si2	Mn23C6	α2		Co2Si*	(Co2C)	Ni3Si*	
Ti5Si4		V6Si5	VC	CrSi	Cr3C2	Mn5Si3	Mn3C	Fe2Si		CoSi		Ni31Si12	
TiSi		VSi2	V6C5	CrSi2		MnSi	Mn5C2	Fe5Si3		(Co2Si3)		Ni5Si2	
TiSi2			V8C7			MnSi1.75-x	Mn7C3	FeSi		CoSi2		Ni2Si*	
								FeSi2*				Ni3Si2	
												NiSi	
												NiSi2*	
Zr 40		Nb 41		Mo 42		Tc 43		Ru 44		Rh 45		Pd 46	
Zr3Si	ZrC	(Nb7Si)	Nb2C*	Mo3Si	β*			Ru2Si		Rh2Si		Pd5Si	
Zr2Si		Nb3Si*	Nb4C3-x	Mo5Si3	η			Ru5SI3		Rh5Si3		Pd9Si2	
Zr5Si3		Nb5Si3*	NbC1-x	MoSi2*	δ			Ru4Si3		Rh20Si13		Pd3Si	
Zr3Si2		NbSi2	Nb6C5		MoC			RuSi*		Rh3Si2		Pd2Si*	
Zr5Si4*								Ru2Si3*		RhSi*		PdSi	
ZrSi*										Rh4Si5			
ZrSi2										Rh3Si4			
Hf 72		Ta 73		W 74		Re 75		Os 76		Ir 77		Pt 78	
Hf2Si	HfC	Ta3Si	Ta2C*	W5Si3	β*	Re2SI	(Re2C)	OsSi		Ir3Si		Pt3Si*	
Hf3Si2		Ta2Si	ζ	WSi2	γ	ReSi		Os2Si3		Ir2Si		Pt12Si5*	
Hf5Si4		Ta5Si3*	TaC		δ	ReSi1.8		OsSi2		IrSi		Pt2Si*	
HfSi		TaSi2								Ir2Si3		Pt6Si5	
HfSi2		(Ta4.5Si)								Ir4Si5		PtSi	
										Ir3Si4		(Pt2Si3)	
										IrSi2		(Pt4Si9)	
										IrSi3*			

Ref.: Binary Alloy Phase Diagrams, 2nd ed., ASM, 1990.
( ): meta-stable phase
*: polymorphic phases exist

The experimental results discussed here were obtained with either cubic or hexagonal, single-crystalline SiC substrates. The effects of polytype or crystallinity of SiC on the interfacial reactions are not clearly determined yet.

The morphology of the reaction zone and the reaction products between SiC and bulk metals [4-11] differ considerably from the thin-film cases discussed here. This may be analogous to the well-known phenomenon of the difference in the phase formation for bulk and thin-film binary diffusion couples [23].

1.3 Electrical Characterization

The electrical properties of metal contacts on SiC are still in an early stage of investigation. Table 1.4 to Table 1.7 list the Schottky or ohmic performance of metal contacts on SiC found in the literature. The classification in these tables is based on the parameters that primarily determine the electrical properties of the contacts. The parameters listed in these tables include the polytype of the SiC substrate and the type and concentration of the free charge carriers, as well as the heat treatment of the contacts. Crystal face is another parameter which may affect the contact property, especially for the 6H-SiC, which may be terminated on the (0001)Si face or the $(000\bar{1})$C face. However, only a few papers in the literature have discussed this effect and they are marked by an asterisk with the polytype notation (e.g., 6H*). Waldrop et al. [Wa92, Wa93] have reported that Ag, Al, Ni and Ti have a significantly larger Schottky barrier height for C-Face compared to Si-face, but it is the other way around for Au. Rastegaeva et al. [Ra92] reported that the contact resistivity of the tungsten contact to the $(000\bar{1})$C face of n-6H-SiC is 2-2.5 times greater than that of to the (0001)Si face. The reason for these differences is not yet known.

Since the barrier heights of the Schottky contacts are very sensitive to the surface states, factors like crystalline quality and orientation of the SiC substrate, surface preparation, and deposition procedures will all affect the performance of Schottky contacts. Because of

this, different experimentalists measured various barrier heights for a given metal. No conclusive correlation between the metal work function and the barrier height has emerged [20].

We are more concerned about ohmic contacts than Schottky contacts. The contact resistivity of the ohmic contacts are listed in the tables if they are available in the literature. Two general trends for ohmic contacts on SiC appear from these literature data. First, for the SiC substrate of carrier concentration 10^{16}-10^{18} cm^{-3}, most of the ohmic contacts are obtained after heat treatments, with a few exceptions for Al [Ed88], Ti [[Ch91], Ta [Che94], W [Ba94, Ch91] and Re [Che94] on n-type SiC that are ohmic as-deposited. However, for the heavily-doped SiC ($\geq 10^{19}$ cm^{-3}), the semiconductor is nearly degenerated so that most of the as-deposited metal contacts are ohmic [Che94, Pe93]. Second, the specific contact resistances are generally in the range of 10^{-2} to 10^{-4} Ω-cm^2. It is still difficult to conclude what metals tend to form ohmic contacts on SiC. The heat treatment and carrier concentration of the SiC substrate seem to be the prevailing factors in determining the ohmicity of the contacts.

Table 1.4 Elemental metal contacts

Notations: Nd, Na: carrier concentration, in cm^{-3}.

β, p or 6H, p : p-type substrate. All others: n-type substrate.

6H*: different contact properties on $(000\bar{1})C$ and (0001)Si.

as-d: as-deposted contacts.

S: Schottky contact.

Ωic : ohmic contact; contact resistivity in Ω-cm^2.

metal	type	Nd, Na	annealing	electrical	Ref.
Ti	β	$\sim 10^{17-18}$	as-d	Ωic	[Ch91]
			300°C, 30 min, in Ar	Ωic (1.7)	
			300°C, 90 min, in Ar	Ωic (7.6×10^{-3})	
			600°C, 10 min, in Ar	Ωic (9.2×10^{-3})	
	6H*	$2\text{-}7\times10^{16}$	as-d to 400°C, 30 s, in ?	S	[Wa93]
	6H	$\sim 10^{16}$	as-d to 700°C, 60 min, UHV	S	[Sp93]
	6H	$\geq 10^{19}$	as-d	Ωic (10^{-3}-10^{-4})	[Pe93]
Hf	6H	$\sim 10^{17}$	as-d to 700°C, 60 min, UHV	S	[Po93]
Ta	β	$\sim 10^{17}$	as-d to 500°C 30 min, in vac	Ωic (10^{-4}-10^{-5})	[Che94]
			900°C, 30 min	non-Ωic	
	β	$\sim 5\times10^{19}$	as-d to 1000°C 1 h, in vac	Ωic (10^{-7}-10^{-6})	[Che94]
	6H	$\geq 10^{19}$	as-d.	Ωic (10^{-3}-10^{-4})	[Pe93]
Cr	β	5×10^{16}	as-d	non-Ωic	[Ed88]
			1250°C, 300s, in vac.	Ωic (7×10^{-2})	
Mo	6H	$\geq 10^{19}$	as-d	Ωic (10^{-3}-10^{-4})	[Pe93]
W	β	2×10^{17}	23°C	Ωic (2.4×10^{-1})	[Ge89]
			900°C, 30 min, in vac.	Ωic (8×10^{-2})	
	β	$\sim 10^{17}$	as-d	Ωic (10^{-3})	[Ba94]

metal	type	Nd, Na	annealing	electrical	Ref.
W	β	$\sim 10^{17-18}$	as-d	Ωic (1.5×10^{-2})	[Ch91]
			300°C, 30 min, in Ar	Ωic (6×10^{-3})	
			300°C, 390 min, in Ar	Ωic (1.5×10^{-2})	
			600°C, 10 min, in Ar	Ωic (2.3×10^{-2})	
	6H*	3×10^{18}	burn-in @1400-1600°C		[Ra92]
			27-677°C,	Ωic (2×10^{-3})	
Re	β	$\sim 10^{17}$	as-d to 500°C 30 min, in vac	Ωic ($\sim 10^{-4}$)	[Che94]
			900°C, 30 min	non-Ωic	
	β	$\sim 5\times10^{19}$	as-d to 900°C 30 min, in vac	Ωic (10^{-4}-10^{-5})	[Che94]
Co	6H	3×10^{18}	as-d	S	[Po94]
			800°C, 20 min, in UHV	leaky	
			1000°C, 2 min, in UHV	Ωic (2.5×10^{-2})	
Ni	β	5×10^{16}	as-d	non-Ωic	[Ed88]
			1250°C, 300s, in vac.	Ωic (1.4×10^{-1})	
	6H	4×10^{17}	1000°C, 20 s	Ωic(1.7×10^{-4})	[Ke91]
	6H	3×10^{17}	1200°C, 3 min, in Ar	Ωic	[Ya87]
	6H	$2\text{-}7\times10^{16}$	as-d to 600°C, 30 s, in ?	S	[Wa93]
	6H	4.7×10^{18}	as-d	non-Ωic	[Cr92]
			950C, 5 min, in H2-Ar	Ωic ($\times10^{-2}$)	
	6H	10^{17-18}	as-d	S	[Pe92]
			825°C, 2 min, in 3%H2-N2	S	
	6H	9.8×10^{17}	as-d	non-Ωic	[Ad94]
			1050°C, 5 min, in ?	Ωic (10^{-3}–10^{-4})	
	6H	$7\text{-}9\times10^{18}$	950C, 2 min, in vac	10^{-7}–10^{-6}	[Cr94]
Pt	β	$5\times10^{16-17}$	as-d to 800°C, 20 min , in ?	S	[Pa89]
	β	$\sim 10^{17}$	as-d to 900°C, 30 min , in vac	non-Ωic	[Che94]
	β	$\sim 5\times10^{19}$	as-d to 500°C, 30 min , in vac	Ωic ($\sim 10^{-6}$)	[Che94]
			900°C, 30 min , in vac	non-Ωic	
	6H	$\times10^{17}$	as-d to 750°C, 20 min,UHV	S	[Po93]

metal	type	Nd, Na	annealing	electrical	Ref.
Ag	6H, 15R	2×10^{17}	as-d	S	[Ha68]
	6H, p	5×10^{18}	as-d	S	[Ha68]
	6H*	$2\text{-}7\times10^{18}$	as-d	S	[Wa92]
Au	β	$5\text{-}9\times10^{17}$	as-d	S	[Yo85]
	β	$5\times10^{16\text{-}17}$	as-d - 500°C, 1.5 h, in Ar	S	[Io87]
			700°C, 0.5 h, in Ar	Ωic	
	Hex	?	as-d	S	[Me64]
	6H, 15R	2×10^{17}	as-d	S	[Ha68]
	6H, p	5×10^{18}	as-d	S	[Ha68]
	6H	10^{17}	as-d	S	[Wu74]
	6H*	$2\text{-}7\times10^{16}$	as-d	S	[Wa92]
	6H, p	2×10^{16}	as-d	S	[Po94]
		$10^{18}\text{-}10^{19}$	as-d	S	[Po94]
Al	β	5×10^{16}	as-d	Ωic	[Ed88]
			900°C, 180-300 s, in vac.	S	
	β, p	1×10^{16}	as-d	high ρ	[Ed88]
			847°C, 180s, in vac.	Ωic (3.1×10^{-2})	
	Hex	?	as-d	S	[Me64]
	6H, 15R	2×10^{17}	as-d	S	[Ha68]
	6H, p	5×10^{18}	as-d	S	[Ha68]
	6H	3×10^{17}	as-d	leaky	[Ya87]
			660°C, 3 min, in Ar	S	
	6H, p	1×10^{18}	as-d	S	[Cr92]
			700C, 10 min, in H2-Ar	Ωic (1.7×10^{-3})	
	6H*	$2\text{-}7\times10^{16}$	as-d	S	[Wa92]
	6H*	$2\text{-}7\times10^{16}$	as-d to 600°C, 30 s, in ?	S	[Wa93]
	6H, p	8×10^{18}	as-d	non-Ωic	[Ad94]
			800C, 10 min, in ?	Ωic ($10^{-2}\text{-}10^{-3}$)	

Table 1.5 Metal-alloy contacts

Alloy	type	Nd, Na	annealing	electrical	Ref.
$Ta_{.03}Au_{.97}$	β	5×10^{16}	as-d	non-Ωic	[Ed88]
			1250°C, 300s, in vac.	Ωic (3×10^{-2})	
Ni-Cr (60%-40% weight %)	6H	4.7×10^{18}	as-d	non-Ωic	[Cr92]
			950C, 5 min, in H2-Ar	Ωic (1.8×10^{-3})	
Ti-W (10%-90% weight %)	6H		as-d	non-Ωic	[Cr92]
		4.7×10^{18}	600C, 5 min, in H2-Ar	Ωic (7.8×10^{-4})	
		2×10^{18}	600C, 5 min, in H2-Ar	non-Ωic	
Ni-Mo	6H	$\sim10^{17-18}$	as-d to 825°C, 2 min	non-Ωic	[Pe92]
			925°C, 2 min, in 3%H2-N2	Ωic ($2\text{-}7\times10^{-4}$)	
Al-Ti	6H, p	5×10^{15}	1000 °C, 5 min	Ωic (2.9×10^{-2})	[Cr93]
		1.6×10^{16}		Ωic (5.5×10^{-3})	
		1×10^{17}		Ωic (1.7×10^{-3})	
		1×10^{18}		Ωic (8.3×10^{-4})	
		1.5×10^{19}		Ωic (4.2×10^{-4})	
		2×10^{19}		Ωic (1.5×10^{-5})	

Table 1.6 Multilayered metal contacts

metal layers	type	Nd, Na	annealing	electrical	Ref.
Ta/Au (100/300nm)	β	$\sim10^{16}$	800°C 1h, in forming gas	Ωic (2×10^{-3})	[Mc92]
W/Au (100/300nm)	β	$\sim10^{16}$	800°C 1h, in forming gas	Ωic (1×10^{-3})	[Mc92]
Ti/W/Au (30/100/300nm)	β	$\sim10^{16}$	800°C 1h, in forming gas	Ωic (5×10^{-3})	[Mc92]
Ni/Ti/W	6H	1×10^{18}	1050°C, 5 min, in ?	Ωic ($10^{-3}\sim10^{-4}$)	[Ad94]
Al/Pt/W	6H, p	8×10^{18}	800-850°C, 10 min, in ?	Ωic ($10^{-2}\sim10^{-3}$)	[Ad94]

Table 1.7 Silicides contacts

Silicide	type	Nd, Na	annealing	electrical	Ref.
$TiSi_2$	β	~10^{17-18}	RTA, 1000°C, 10s	Ωic (1.4×10^{-1})	[Ch91]
			300°C, 10-390 min, in Ar	Ωic (1.4×10^{-2})	
			450°C, 10-390 min, in Ar	Ωic (1×10^{-4})	
	6H	≥10^{19}	as-d	Ωic (10^{-3}-10^{-4})	[Pe93]
$TaSi_2$	β	5×10^{16}	as-d	non-Ωic	[Ed88]
			850°C, 300s, in vac.	Ωic (2×10^{-2})	
	6H	~10^{17-18}	as-d to 825°C, 2 min	S	[Pe92]
			925°C, 2 min, in 3%H2-N2	leaky	
	6H	≥10^{19}	as-d	Ωic (10^{-3}-10^{-4})	[Pe93]
$MoSi_2$	6H	~10^{17-18}	as-d to 825°C, 2 min	S	[Pe92]
			925°C, 2 min, in 3%H2-N2	leaky	
	6H	≥10^{19}	as-d	Ωic (10^{-3}-10^{-4})	[Pe93]
WSi_2	β	~10^{17-18}	RTA, 1000°C, 10s	Ωic (3.7×10^{-2})	[Ch91]
			300°C, 390 min, in Ar	Ωic (2×10^{-2})	
			450°C, 10 min, in Ar	Ωic (3×10^{-4})	
			450°C, 390 min, in Ar	Ωic (3.9×10^{-4})	
Al/$TaSi_2$	β	1×10^{16}	as-d to 800°C 1800s	non-Ωic	[Ed88]
			1200°C, 1800s, in vac	Ωic (2×10^{-1})	

REFERENCES (Chapter 1)

1. R. F. Davis, G. Kelner, M. Shur, J. W. Palmour, and J. A. Edmond, Proc. of the IEEE, vol. 79, p. 677 (1991).
2. A. G. Metcalfe, ed., "*Composite Materials: Interfaces in Metal matrix composites,*" Chap. 3 and 4, Academic Press, New York, 1974.
3. B. Maruyama, E. V. Barrera, and L. Rabenberg, in "*Metal matrix composites: processing and interfaces,*" edited by R. K. Everett and R. J. Arsenault, p. 181, Academic Press, San Diego, 1991.
4. P. Martineau, R. Pailler, M. Lahaye, and R. Naslain, J. Mat. Sci., 19, 2749 (1984).
5. M. B. Chamberlain, Thin Solid Films, 72, 305 (1980).
6. T. C. Chou, A. Joshi, and J. Wadsworth, J. Mat. Res. 6, 796 (1991).
7. T. C. Chou, A. Joshi, and J. Wadsworth, J. Vac. Sci. Technol., A9, 1525 (1991).
8. R. C. J. Schiepers, F. J. J. van Loo, and G. de With, J. Am. Ceram. Soc. 71, C-284 (1988).
9. M. Backhaus-Ricoult, Ber. Bunsenges. Phys. Chem. 93, 1277 (1989).
10. M. Backhaus-Ricoult, Acta Metall. Mater. Vol. 40. Suppl, S95 (1992).
11. S. Sambasivan and W. T. Petuskey, J. Mater. Res. 7, 1473 (1992).
12. Aijt Ram Verma and P. Krishna, *Polymorphism and Polytypism in Crystals*, John Wiley and Sons, New York, 1966.
13. Landolt-Börnstein, Numerical Data and Function Relationships in Science and Technology, New Series III, Vol. 17a, editor: O. Madelung, pp. 132-142, 442-449, Springer-Verlag Berlin, New York, 1982.
14. J. S. Bow, L. M. Porter, M. J. Kim, R. W. Carpenter, and R. F. Davis, Ultramicroscopy 52, 289 (1993).
15. A. Joshi, H. S. Hu, L. Jesion, J. J. Stephens, and J. Wadsworth, Metall. Trans. 21A, 2829 (1990).
16. K. M. Gieb, C. Wilson, R. G. Long, and C. W. Wilmsen, J. Appl. Phys. 68, 2796 (1990).

17. J. S. Chen, E. Kolawa, M-A. Nicolet, R. P. Ruiz, L. Baud, C. Jaussaud, and R. Madar, to be published in J. Appl. Phys., August, 1994.

18. S. Hara, K. Suzuki, A. Furuya, Y. Matsui, T. Ueno, I. Ohdomari, S. Misawa, E. Sakuma, S. Yoshida, Y. Ueda, and S. Suzuki, Jap. J. Appl. Phys., 29, L394 (1990).

19. J. S. Chen, E. Kolawa, M-A. Nicolet, L. Baud, C. Jaussaud, R. Madar, and C. Bernard, J. Appl. Phys. 75, 897 (1994).

20. L. M. Porter, Ph.D. Thesis, North Carolina State University, Raleigh, NC, 1993.

21. J. S. Bow, L. M. Porter, M. J. Kim, R. W. Carpenter, and R. F. Davis, Mat. Res. Soc. Symp. Proc. Vol 280, (Materials Research Society, Pittsburg, 1993), p. 571.

22. J. S. Chen, E. Kolawa, M-A. Nicolet, R. P. Ruiz, L. Baud, C. Jaussaud, and R. Madar, J. Mat. Res. 9, 648 (1994).

23. K. N. Tu, J. W. Mayer, and L. C. Feldman, *Electronic Thin Film Science for Electrical Engineers and Materials Scientists,* Chap. 12, Macmillan Publishing, New York, 1992.

References for Tables 1.4 to 1.7

[Ad94] S. Adams, J. Leonard, S. Liu, and S. R. Smith, High Temperature Electronics Conf., Charlotte, June 5-10, 1994.

[Ba94] L. Baud, C. Jaussaud, and R. Madar, J. S. Chen, A. Bächli, M-A. Nicolet, European Materials Research Society Spring Meeting, Strasbourg, France, May 24-27, 1994.

[Ch91] M. I. Chaudhry, W. B. Berry, and M. V. Zeller, Int. J. Electronics, 71, 439 (1991).

[Che94] J. S. Chen, A. Bächli, M-A. Nicolet, L. Baud, C. Jaussaud, and R. Madar, European Materials Research Society Spring Meeting, Strasbourg, France, May 24-27, 1994.

[Cr92] J. Crofton, J. M. Ferrero, P. A. Barnes, J. R. Williams, M. J. Bozack, C. C. Tin, C. D. Ellis, J. A. Spitznagel, and P. G. MaMullin, in *Amorphous and Crystalline Silicon Carbide IV*, edited by C. Y. Yang, M. M. Rahman, and G. L. Harris, p. 176, Springer-Verlag, Berlin, 1992.

[Cr93] J. Crofton, P. A. Barnes, J. R. Williams, and J. A. Edmond, Appl. Phys. Lett. 62, 384 (1993).

[Cr94] J. Crofton, P. G. McMullin, J. R. Williams, M. J. Bozack, High Temperature Electronics Conf., Charlotte, June 5-10, 1994.

[Ed88] J. A. Edmond, J. Ryu, J. T. Glass, and R. F. Davis, J. Electrochem. Soc., 135, 359 (1988).

[Ge89] K. M. Geib, J. E. Mahan, and C. W. Wilmsen in *Amorphous and Crystalline Silicon Carbide and Related Materials II*, eds. M. M. Rahman, C. Y.-W. Yang and G. L. Harris, p. 224, Spring-Verlag Berlin, Heiderlberg, 1989.

[Ha68] S. H. Hagen, J. Appl. Phys., 39, 1458 (1968).

[Io87] D. E. Ioannou, N. A. Papanicolaou, and P. E. Nordquist,, IEEE Trans. Elec. Dev. ED-34, 1694 (1987).

[Ke91] G. Kelner, S. Binari, M. Shur, and J. Palmour, Elec. Lett. 27, 1038 (1991).

[Mc92] P. G. McMullin, J. A. Spitznagel, J. R. Szedon, and J. A. Costello, in *Amorphous and Crystalline Silicon Carbide and Related Materials III*, eds. G. L Harris, M. G. Spencer and C. Y.-W. Yang, p. 275, Spring-Verlag Berlin, Heiderlberg, 1992.

[Me64] C. A. Mead and W. G. Spitzer, Phys. Rev., 134, A713 (1964).

[Pa89] N. A. Papanicolaou, A. Christou, and M. L. Gipe, J. Appl. Phys. 65, 3526 (1989).

[Pe92] J. B. Petit and M. V. Zeller, Mat. Res. Soc. Symp. Proc., Vol. 242, p. 567, 1992.

[Pe93] J. B. Petit, P. G. Neudeck, C. S. Salupo, D. J. Larkin, and J. A. Powell, abstract for the International Conference on Silicon Carbide and Related Materials, Washington D. C., Nov. 1-3, 1993.

[Po93] L. M. Porter, R. C. Glass, R. F. Davis, J. S. Bow, M. J. Kim, and R. W. Carpenter, Mat. Res. Soc. Symp. Proc., Vol. 282, p. 471, 1993.

[Po94] L. M. Porter, R. C. Glass, R. F. Davis, J. S. Bow, M. J. Kim, and R. W. Carpenter, High Temperature Electronics Conf., Charlotte, June 5-10, 1994.

[Ra92] M. G. Rastegaeva and A. L. Syrkin, Sensors and Actuators A, 33, 95 (1992).

[Sp91] L. M. Spellman, R. C. Glass, R. F. Davis, T. P. Humphreys, H. Jeon, R. J. Nemanich, S. Chevacharoenkul, and N. R. Parikh, Mat. Res. Soc. Symp. Proc., Vol. 221, p. 99, 1991.

[Wa92] J. R. Waldrop, R. W. Grant, Y. C. Wang, and R. F. Davis, J. Appl. Phys. 72, 4757 (1992).

[Wa93] J. R. Waldrop and R. W. Grant, Appl. Phys. Lett. 62, 2685 (1993).

[Wu74] S. Y. Wu and R. B. Campbell, Solid-St. Electro. 17, 683 (1974).

[Ya87] K. Yasuda, T. Hayakawa, and M. Saji, IEEE Trans. Elec. Dev. ED-34, 2002 (1987).

[Yo85] S. Yoshida, K. Sasaki, E. Sakuma, S. Misawa, and S. Gonda, Appl. Phys. Lett. 46, 766 (1985).

Chapter 2
Experimental Procedures

2.1 Metal Deposition and Annealing

Single-crystalline (001) β-SiC ~5 μm in thickness was grown on the (001) Si substrates by CVD. By x-ray rocking curve, the full width of half maximum of the β-SiC (400) peak is 0.15°. As a reference, the full width of half maximum of the Si substrate (400) peak is 0.1°. The Si/SiC substrate was degreased in organic solvent baths and chemically etched with dilute HF for ~2 minutes before loading into the deposition chamber.

Re, Pt and Ta films were deposited on the SiC side of the substrate by rf sputtering with Ar gas. The resulting thickness of the film is about 40, 70 and 320 nm for Re, Pt and Ta, respectively. The base pressure of the sputtering system used is 5×10^{-7} Torr. The Si/SiC/metal (metal=Re, Pt or Ta) wafer was then cut into several pieces (~ 0.8 cm × 1 cm) and some of them were annealed in a tube vacuum furnace for 1 h or 30 min at temperatures ranging from 300°C to 1100°C at a pressure lower than 5×10^{-7} Torr. 1100°C/30 min is the maximum allowable excursion of our tube vacuum furnace. One Ta sample was sealed in a quartz ampoule under vacuum (~ 10^{-6} Torr) and then annealed at 1200°C for 1 h in another furnace to reach the final equilibrium state of the SiC/Ta system.

For contact resistivity measurement, both as-grown SiC and nitrogen-implanted SiC were used as the substrates. The as-grown SiC has a non-intentional doping concentration of ~10^{17} cm^{-3} and a sheet resistance of about 250 Ω/square. Some of these samples were implanted four times with nitrogen of different energies and doses to obtain an approximately uniform doping concentration of 5×10^{19} cm^{-3} in the first 250 nm of the SiC. The implanted samples were annealed in Ar at 1200 °C for 30 min to activate the dopants. The sheet resistance of the implanted samples is about 125 Ω/square.

The circular pattern with concentric contacts (see Chapter 6) were fabricated on SiC by photolithography. Prior to loading into the deposition chamber, the substrate was chemically etched in dilute HF for ~2 min. The base pressure of the deposition system is 5×10^{-7} Torr. There followed a blanket deposition of Re, Pt and Ta films by rf sputtering with Ar gas. The resulting thickness of the Re film is ~300 nm, that of the Pt film is ~ 200 nm, and that of the Ta film is ~320 nm. The circular contacts on the SiC substrates were then formed by lift-off. Heat treatments of the contacts were also carried out in a vacuum tube furnace at 500 °C and 900 °C for 30 min, with a pressure lower than 5×10^{-7} Torr. Some of the Ta contacts were also annealed at 1000 °C for 1 h and 1100 °C for 30 min.

2.2 Analysis Techniques

All samples, as-deposited and after thermal annealing, were characterized by 3 MeV $^{4}He^{++}$ backscattering spectrometry for depth profiles of composition, and by Debye-Scherrer x-ray diffraction using a glancing angle of beam incidence and an Inel position-sensitive detector for phase identification. The surface and cross-sectional morphologies of selected samples were examined by scanning electron microscopy. Samples for cross-sectional scanning electron microscopy were fractured in liquid nitrogen. The cross-sectional microstructure of selected samples were characterized by transmission electron microscopy on a Philips EM430 microscope operating at 300 kV. To obtain the cross-sectional specimen, samples were glued face-to-face, mechanically thinned down to ~20 μm, and finally milled by Ar-ions to electron transparency. Secondary-ion mass spectrometry was performed with a 6 keV Xe ion sputtering beam at an incident angle of 60°. The concentrations were obtained by using the sensitivity factors for the elements. The concentration sensitivity limits of C, Si, Re, Pt and Ta for these spectra are 10^{18}, 10^{16}, 10^{17}, 10^{17} and 10^{17}-10^{18} cm^{-3}, respectively.

The details regarding the contact resistivity measurement are described in Chapter 6.

Chapter 3
Stability of Rhenium Thin Films on Single Crystal (001) β-SiC

3.1 Interface Structure

The SiC/Re samples annealed individually at 700°C, 800°C, 900°C, 1000°C, 1100°C for 30 min all have backscattering spectra that differ insignificantly from that of the as-deposited sample (see Fig. 3.1 for the spectra of the as-deposited and 1100°C-annealed samples). X-ray diffraction spectra of all samples only contain diffraction peaks of rhenium metal, which indicates that no significant reaction between Re and SiC has occurred upon annealing.

Plan-view transmission electron micrographs and the corresponding selected-area diffraction patterns are shown in Fig. 3.2 for the as-deposited sample and a 1100°C-annealed sample. The average grain size in the as-deposited sample is about 220 nm (Fig. 3.2(a)); for the 1100°C-annealed sample, it is about 280 nm (Fig 3.2(b)). However, more small grains (< 40 nm) exist in the as-deposited sample than in the 1100°C-annealed sample. Also, the gaps between grains is wider (~3 nm) in the 1100°C-annealed sample than in the as-deposited sample (<1.5 nm).

For the as-deposited SiC/Re sample, all {hkil} diffraction rings of the hexagonal Re structure are seen, even though the {hkil, l≠0} rings are relatively weak (see inset diffraction pattern of Fig. 3.2(a)). On the other hand, after annealing at 1100°C, only {hki0} diffraction rings are clearly present (inset diffraction pattern of Fig. 3.2(b)). This implies that the 1100°C-annealed Re film are composed of grains with {0001} fiber texture (orientational relationship: $\{0001\}_{Re}//\{001\}_{SiC}$). The circular uniformity of all diffraction rings in Fig. 3.2(b) indicates that the Re grains are randomly oriented around the $\{0001\}_{Re}$

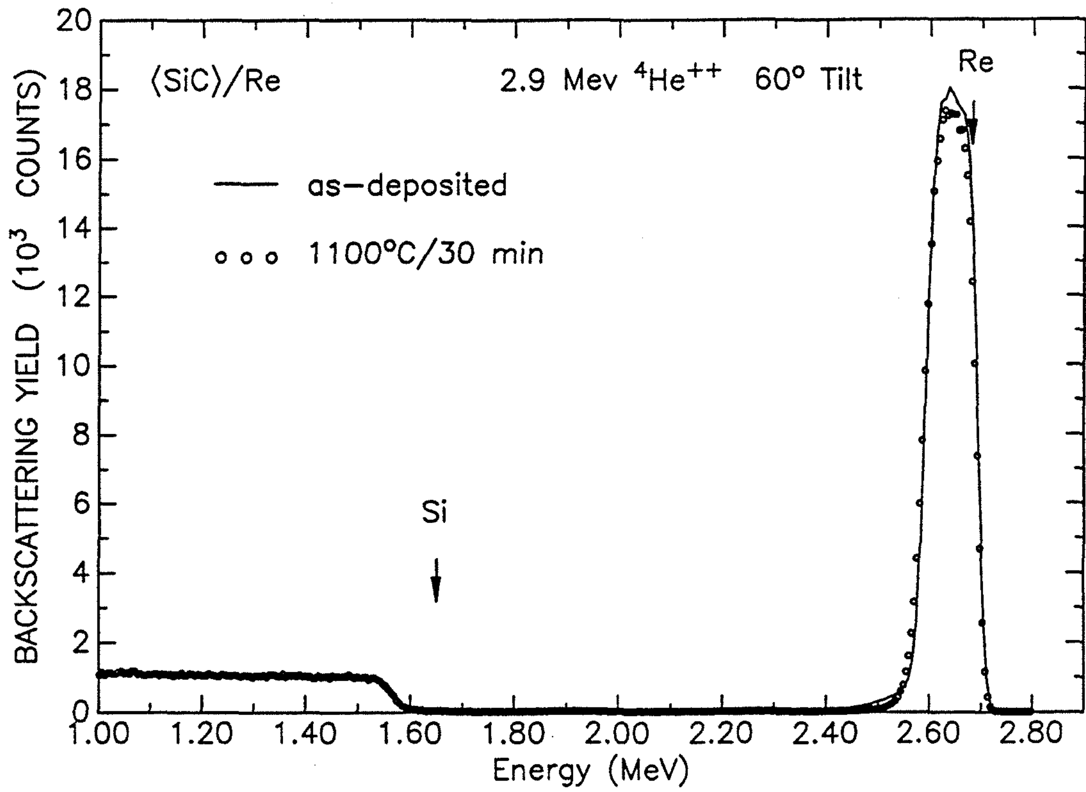

Fig. 3.1 2.9 MeV $^4He^{++}$ backscattering spectra of <β-SiC>/Re samples before and after annealing at 1100°C for 30 min.

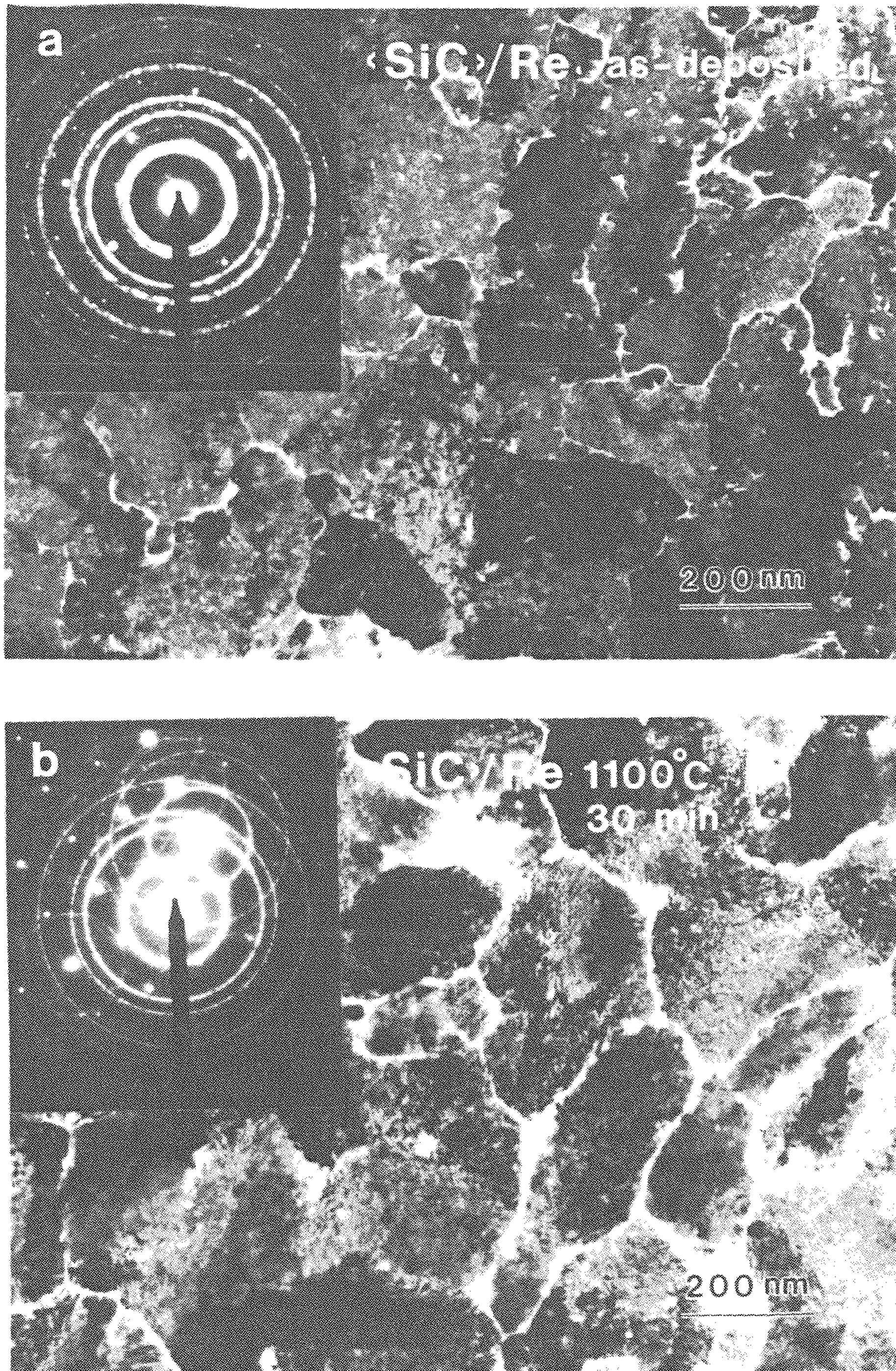

Fig. 3.2 Bright-field, plan-view transmission electron micrographs of (a) the as-deposited <β-SiC>/Re sample and (b) the 1100°C-annealed <β-SiC>/Re sample. The inset selected-area diffraction patterns are taken from the region shown in the corresponding micrograph. The diffraction spots are originated from the single-crystal SiC while the diffraction rings are originated from the polycrystalline Re.

fiber axis. The diffraction rings centered on some of SiC diffraction spots are due to the double diffraction; the electrons diffracted by SiC again act as incident electrons for a second scattering from Re.

Figure 3.3 is a cross-sectional transmission electron micrograph of the SiC/Re sample after annealing at 1100°C for 30 min. The lateral uniformity of the Re film does not deteriorate by the annealing. A sharp interface between Re and SiC is shown and no Si signal is detected in the Re film by energy-dispersive analysis of x-rays (EDAX). The gap between two grains is consistent with the observation in the plan-view transmission electron micrograph.

Figure 3.4 shows the depth profiles of Re, Si and C before and after annealing at 1100°C for 30 min obtained by secondary ion mass spectrometry. The sharpness of the SiC/Re interface changes insignificantly. This result is consistent with those of the backscattering analysis (Fig. 3.1), x-ray diffraction, and transmission electron microscopy (Fig. 3.3). The Re tail seen in the SiC layer is because of the roughness on the bottom surface of the erosion crater. The Si and C signals shown on the surface should be surface contamination.

<SiC>/Re 1100°C 30min

Fig. 3.3 A bright-field cross-sectional transmission electron micrograph of a <SiC>/Re sample after annealing at 1100°C for 30 min.

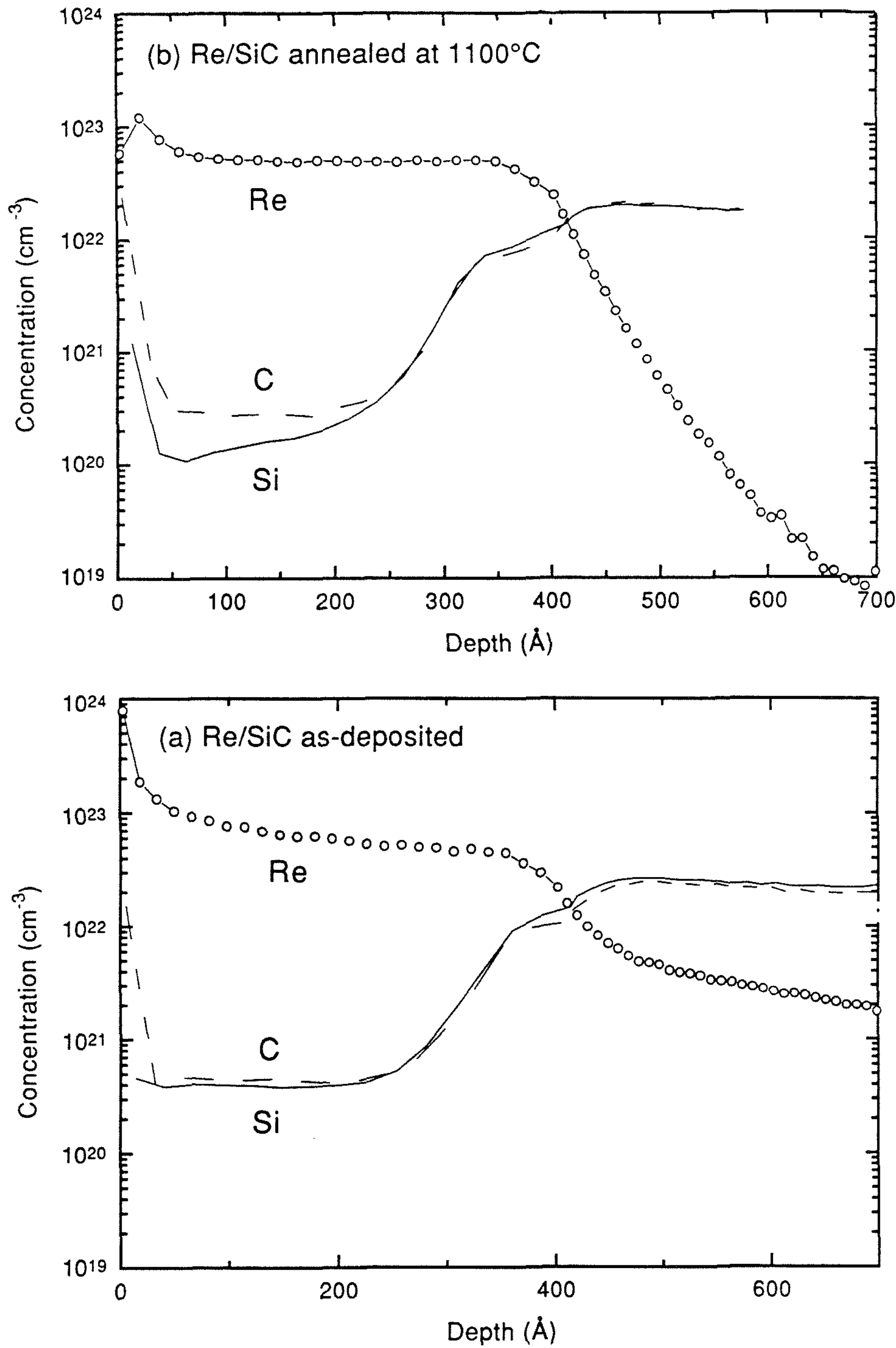

Fig. 3.4 SIMS depth profiles of Re, Si and C for <β-SiC>/Re samples (a) before, and (b) after annealing at 1100°C for 30 min.

3.2 Thermodynamics

To investigate the chemical stability of Re on SiC, we have calculated the isothermal section of the ternary phase diagram for 1100°C. The computation was performed with the GEMINI1 software developed by Thermodata [1]. The program minimizes the total Gibbs free energy of the system. For the calculation, enthalpies of formation at 298K, $\Delta H^{\circ}_{f,\,298}$, absolute entropies at 298K, S°_{298}, and the heat capacity, $c_p(T)$, are needed for each binary phase in the system. It is assumed that ternary phases do not exist and $c_p(T)$ can be represented by the equation $a+bT+cT^2+dT^{-2}$. Table 3.1 lists the values adopted for the calculation. Jorda et al. [2] reported that the phase commonly referred to as Re_5Si_3 is actually Re_2Si. We have found that the modification introduced in the calculation by such a change in stoichiometry is quite small; the conventional nomenclature for that phase has therefore been retained.

Table 3.2 and 3.3 list the thermodynamic data of rhenium silicides commonly found in the literature, as well as those adopted (listed in table 3.1) from Scientific Group Thermadata Europe [3] or after an assessment of the available data by the Gemini1 software.

The result of this thermodynamic calculation is represented in Fig. 3.5. This calculated phase diagram agrees with that determined experimentally by Searcy and Finnie [4] for a temperature of 1600°C and leads credence to the assumption that ternary compounds are absent [5]. We thus conclude that the SiC-Re couple is thermodynamically stable. This calculation explains the absence of any detectable reactions at the SiC/Re interface in our experiments.

Table 3.1a. Enthalpy of formation at 298K, $\Delta H^\circ_{f,298}$, and absolute entropy at 298K, S°_{298}, for different species of the Re-Si-C system.[a]

	$\Delta H^\circ_{f,298}$ (kJ/g-atom)	S°_{298} (J/K g-atom)
Re	0	36.5263
Si	0	18.8196
C	0	5.74
Re_5Si_3	-19.66	31.98
ReSi [b]	-20.56	27.68
$ReSi_2$	-30.12	24.68
SiC	-36.61	8.30

[a] from database SGTE: Scientific Group Thermadata Europe.

[b] unstable below 1650°C.

Table 3.1b. Heat capacity equations for different species of the Re-Si-C system: c_p(J/K g-atom) = $a+bT+cT^2+dT^{-2}$ (T in K).

	a	10^3xb	10^5xc	10^{-5}xd	Temperature limits (K)
Re	23.689	5.446	0.0	0.0	298 - 3453
Si	22.832	3.826	0.0021	-3.533	298 - 1685
C	-3.172	44.277	-1.701	0.0	298 - 400
C	-7.062	59.246	-3.288	0.7071	400 - 600
C	11.057	18.555	-0.701	-10.16	600 - 900
C	20.301	4.457	-0.0936	-22.115	900 - 1400
C	23.484	1.293	-0.00445	-31.923	1400 - 2700
Re_5Si_3	23.845	5.648	0.0	-1.757	298 - 2000
ReSi	26.296	4.811	0.0	-1.883	298 - 2000
$ReSi_2$	22.594	3.682	0.0	-2.036	298 - 2000
SiC	12.538	22.11	-1.036	-4.257	298 - 800
SiC	23.643	2.603	-0.0384	-16.309	800 - 1800

Table 3.2 Enthalpy of formation of rhenium silicides at 298K (kJ/g-atom).

Reference	Re_5Si_3	ReSi	$ReSi_2$
Chart [a]	-19.7±8	-26.4±10	-30.1±10
Searcy and Finnie [b]		-25.5	-28.7
Machlin [c]		-32.1	
Niessen [d]	-27.0	-28.0	-16.0
Miedema [e]		-29.3	
Baud [f]	-19.66	-20.56	-30.12

[a] T. G. Chart, High temperatures-High pressures, 5, 241 (1973).

[b] A. W. Searcy and L. N. Finnie, J. Am. Ceram. Soc., 45, 268 (1962).

[c] E. S. Machlin, CALPHAD Comput. Coupling Phase Diagrams Thermochem., 5, 1 (1981).

[d] A. K. Niessen, J. Less Comm. Met., 82, 75 (1981).

[e] A. R. Miedema, J. Less Comm Met., 46, 67 (1976).

[f] from database SGTE: Scientific Group Thermadata Europe.

Table 3.3. Entropy of formation of rhenium silicides at 298K (J/K g-atom).

	Re_5Si_3	ReSi	$ReSi_2$
Chart [a]	2.1±2.0	0.0±2.0	0.0±2.0
Baud [b]	2.095	-3.03	-0.03623

[a] T. G. Chart, High temperatures-High pressures, 5, 241 (1973).

[b] from database SGTE: Scientific Group Thermadata Europe and present assessment.

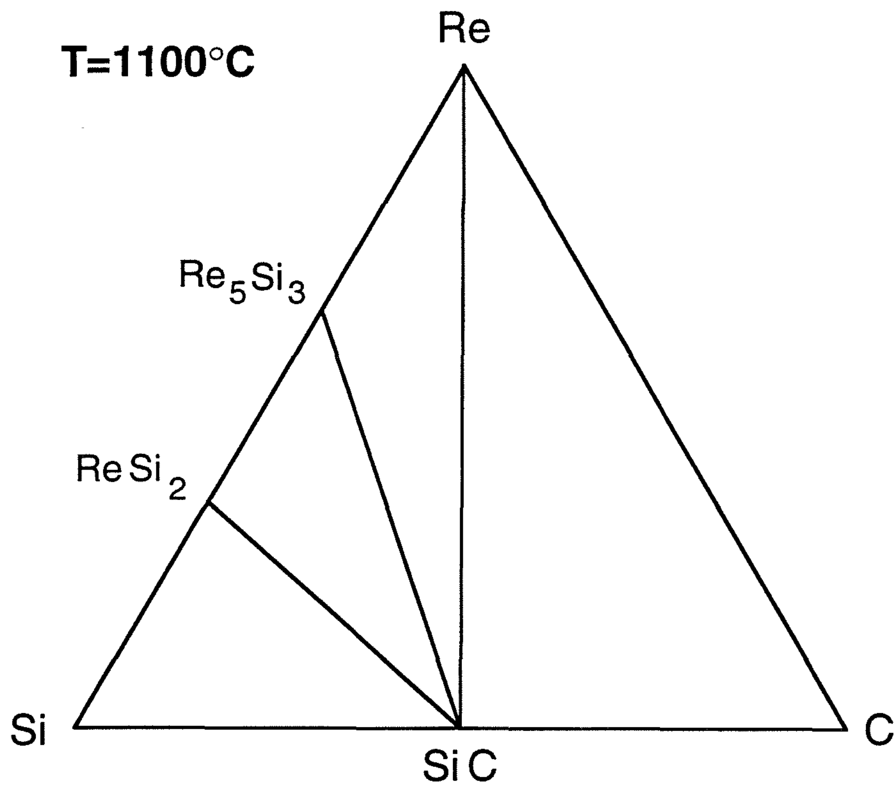

Fig. 3.5 The isothermal section of the Re-Si-C phase diagram calculated for 1100°C.

3.3 Discussion

The thermodynamic stability of Re and β-SiC has both advantages and drawbacks, as far as electronic applications are concerned. A stable metal greatly simplifies the metallurgy of a contact to a semiconductor made with such a metal. The disadvantage is that the electrically active interface of that contact coincides with a previously open surface of the semiconductor. Such contacts tend to pose demanding technological challenges of surface preparation to assure the reproducibility and reliability of the electrical characteristics of the contact. In contrast, silicon integrated circuits manufactured today have electrical contacts whose primary interface with Si is formed *in situ* by solid-phase reaction of a transition metal with Si. This approach favors the reproducibility of the contact, but requires the existence of a stable and laterally uniform reaction product such as $TiSi_2$ or $CoSi_2$, and necessitates the addition of a diffusion barrier to suppress deleterious reactions of the overlying interconnection metal (e.g., Al, W) with the silicide. That approach is impossible with Re and β-SiC, at least at $T \leq 1100°C$. It thus becomes important to investigate electrically the characteristic of the β-SiC/Re contact, and its sensitivity to surface preparation conditions.

In addition to Re, there are two rhenium silicides that are also stable in contact with SiC (see Fig. 3.5). $ReSi_2$ has a high bulk resistivity (~7000 μΩ-cm [6] at room temperature that has been attributed to a semiconducting nature of $ReSi_2$. That of Re_2Si (Re_5Si_3) is not found in the literature. The resistivity of Re is 19.3 μΩ-cm [7]. From the resistivity point of view, Re thus is the preferred choice for contact applications.

REFERENCES (Chapter 3)

1. B. Cheynet and A. Rivet, Saint-Martin-d'Heres, France, 1991.

2. J. L. Jorda, M. Ishikawa, and J. Muller, J. Less-Comm. Met. 85, 27 (1982).

3. Scientific Group Thermadata Europe: Domaine Universitaire, BP 66, F-38042, Saint-Martin-d'Heres, France.

4. A. W. Searcy and L. N. Finnie, J. Ame. Ceram. Soc. 45, 268 (1962).

5. The calculations based on the parameters of Table I predict that at 1127°C the Re-SiC tie line is replaced by a Re_5Si_3-C tie line, which disagrees with the results of ref. 4.

6. G. V. Samsonov and I. M. Vinitskii, *Handbook of Refractory Compounds*, p. 232, IFI/Plenum, New York, 1980.

7. C. T. Lynch, ed., *Handbook of Materials Science*, Vol. I, p. 103, CRC Press, Boca Raton, Florida, 1974.

8. Aijt Ram Verma and P. Krishna, *Polymorphism and Polytypism in Crystals*, p. 16, John Wiley and Sons, New York, 1966.

Chapter 4
Solid-State Reaction of Pt Thin Film With Single-Crystal (001) β-SiC

4.1 Reaction Characterization

4.1.1. Backscattering Spectrometry

Figure 4.1 shows the backscattering spectra of SiC/Pt samples before and after annealing at 500°C, 600°C, or 900°C for 30 min. The total counts of the Pt signals in all spectra are kept the same assuming no Pt loss during reaction. The spectrum of the 450°C-annealed sample is not shown, but it is perfectly overlapping with that of as-deposited sample, even with the beam incident at 60° from the sample normal. At T≥500°C, the height of Pt signal decreases and the low-energy edge broadens with increasing annealing temperature. Concurrently, a plateau-like Si signal is observed for all these samples. The height of this Si signal for the samples annealed at 600°C or 900°C is almost the same and is a little higher than that of the 500°C-annealed sample. The general broadening of the Pt signal at its low-energy side could be due to a lateral nonuniformity of either the surface or the interface morphology. The general shape of the Pt signal suggests that Pt reacts with SiC and forms two layers of different composition. This bilayer structure can be seen clearly by cross-sectional transmission electron microscopy and will be discussed in section 4.1.5.

We have estimated the atomic ratio of Pt:Si near the surface of the reacted layer from the height ratio of the Pt and Si signals at the position of their surface-energy edge. The stopping cross-section factor for scattering from Pt and Si in the reacted Pt-Si layer was first assumed to be equal, and then recalculated by iteration, assuming that the reacted layer near the surface consists of only Pt and Si, no carbon. The atomic ratio of Pt/Si near the surface thus derived for the samples annealed at 500°C, 600°C, and 900°C are 2.9±0.1, 1.9±0.1 and 1.8±0.1, respectively. Also, the surface heights of Pt signals out of Pt_3Si, Pt_2Si and PtSi,

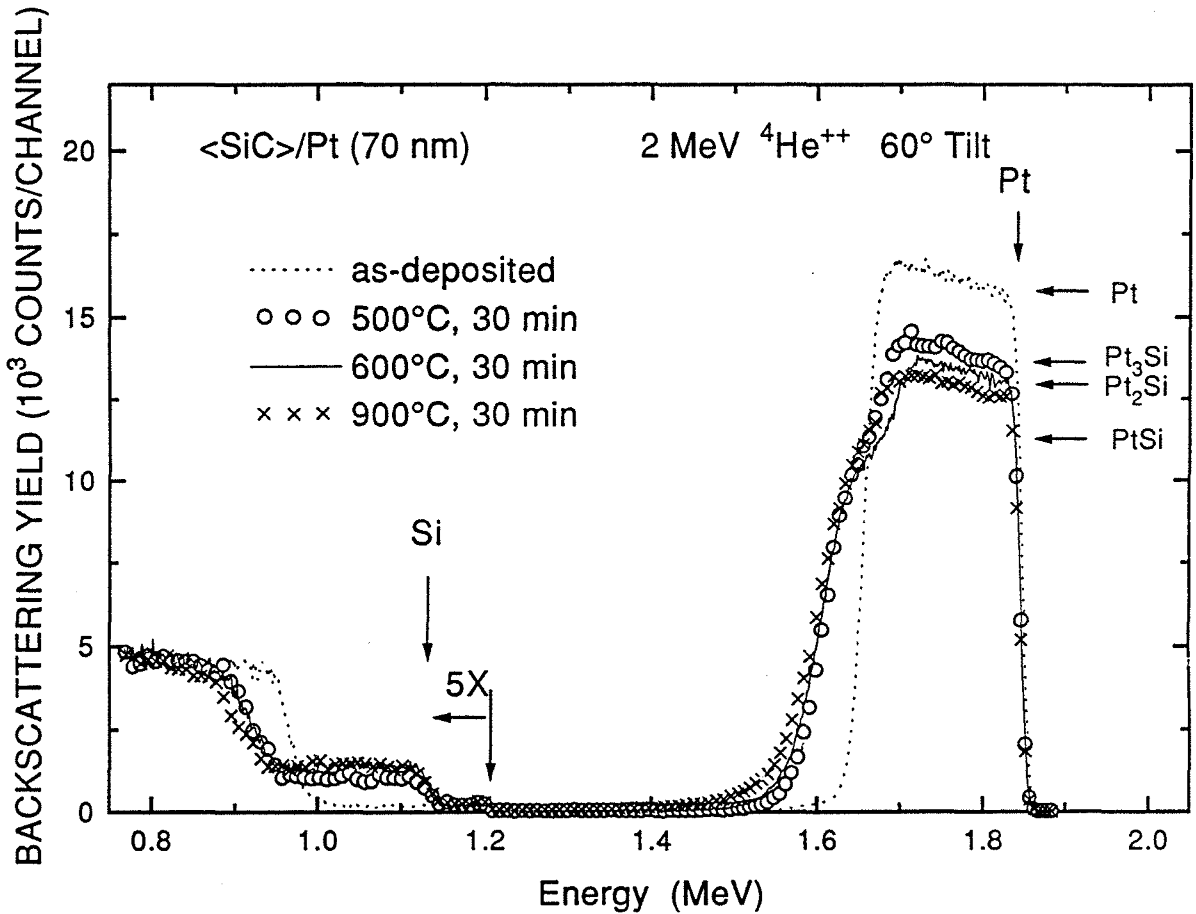

Fig. 4.1. 2.0 MeV $^4He^{++}$ backscattering spectra of <β-SiC>/Pt samples before and after annealing at 500, 600, or 900°C for 30 min. The sample was tilted by 60° and the scattering angle of the detected particles was 170°. Surface energies of Pt and Si, as well as the surface heights of Pt signals out of Pt, Pt_3Si, Pt_2Si, and PtSi are marked by arrows.

relative to the height of Pt signal of pure Pt, can be calculated from their composition and the stopping cross section factor of Pt in the corresponding compound. They are marked in Fig. 4.1 as a reference.

Pt does not form carbides so that the carbon must segregate out somewhere. For the backscattering spectra, the carbon signal is too weak to be seen superimposed as it is over the Si signal of the substrate. The depth concentration profile of carbon can be obtained by secondary ion mass spectrometry and will be discussed in section 4.1.4. The backscattering spectrum of the 1000°C-annealed sample has a wide low-energy-edge tail in the Pt signal due to the rough surface (see section 4.1.3.) and is not shown in Fig. 4.1.

4.1.2. X-ray diffraction

The x-ray diffraction spectra of the as-deposited sample and samples after 30-min annealing at 500°C, 600°C, 900°C, or 1000°C are shown in Fig. 4.2. Diffraction peaks of pure Pt are observed for the as-deposited SiC/Pt sample, as well as the sample annealed at 450°C for 30 min. For the sample annealed at 500°C for 30 min, the diffraction spectrum is quite different from that of the as-deposited sample. We designate the main product phase as monoclinic Pt_3Si. However, due to the similar lattice spacing, there may also exist a minor amount of un-reacted Pt or other Pt-silicides (e.g., $Pt_{12}Si_5$) in the sample. Tetragonal Pt_2Si is observed in the samples annealed at 600-900°C.

These compounds (Pt_3Si and Pt_2Si) have compositions which are consistent with the backscattering analysis. After annealing at 1000°C for 30 min, both tetragonal Pt_2Si and orthorhombic PtSi exist in the sample.

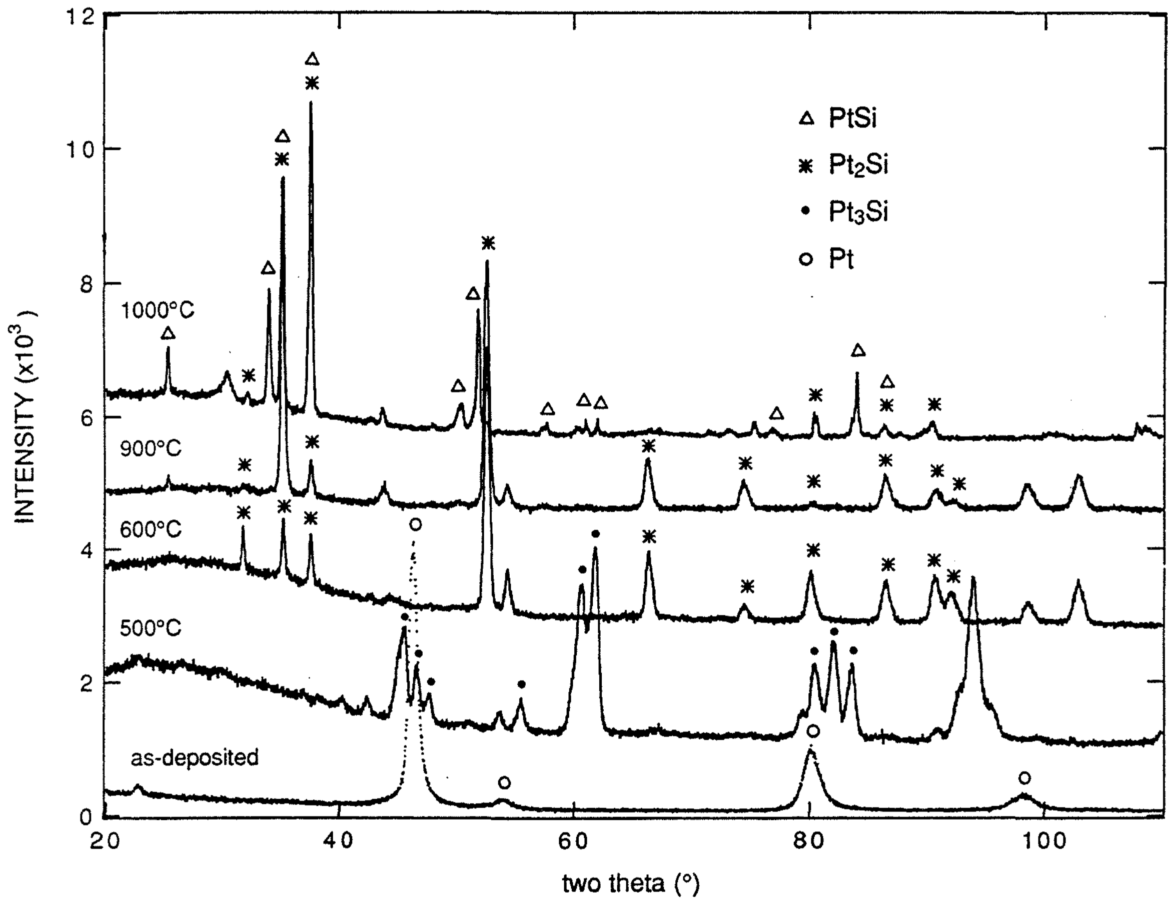

Fig. 4.2 X-ray diffraction (Co-Kα radiation) spectra of <β-SiC>/Pt samples before and after annealing at 500°C, 600°C, 900°C or 1000°C for 30min.

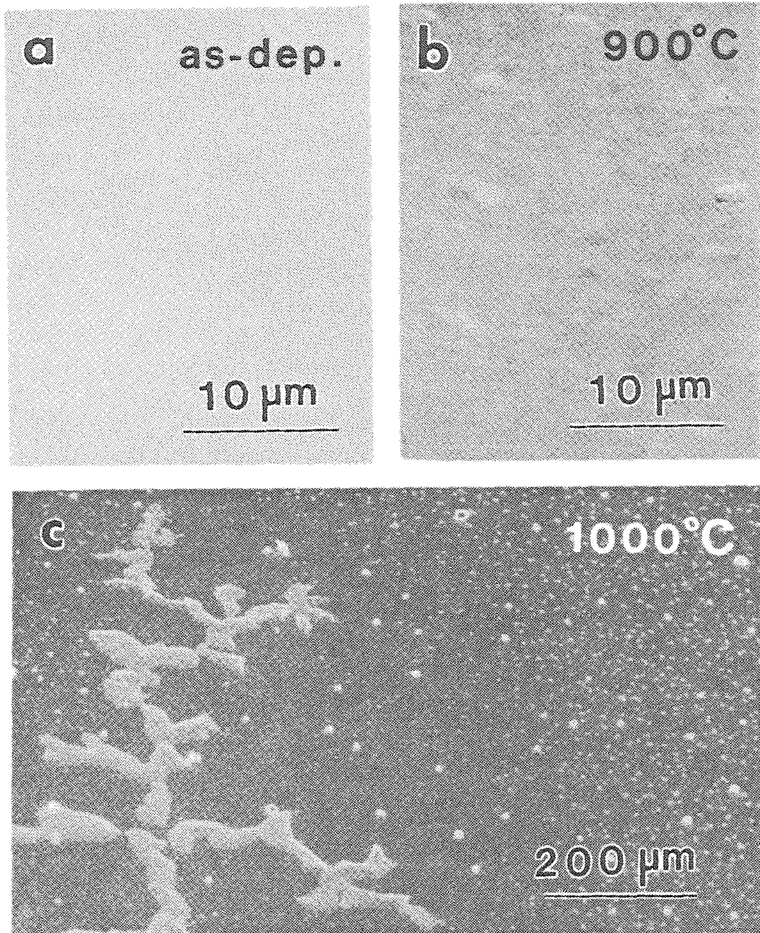

Fig. 4.3 Scanning electron micrographs of <β-SiC>/Pt samples (a) before, and after annealing at (b) 900°C, 30 min; (c) 1000°C, 30 min.

4.1.3. Scanning electron microscopy

Scanning electron microscipy reveals that the surface of the as-deposited SiC/Pt sample is smooth and featureless (Fig. 4.3a). Small hillocks appear on the surface of the 900°C annealed sample (Fig. 4.3b). After annealing at 1000°C for 30 min, blisters, and 100 μm-sized dendrite-like hillocks reminiscent of a solidified liquid are randomly distributed on the sample surface (Fig. 4.3c). There is indeed a eutectic at about 980°C between Pt_2Si and PtSi in the Pt-Si system [1].

4.1.4. Secondary ion mass spectrometry

Figure 4 shows the depth profiles of Pt, Si and C obtained by secondary ion mass spectrometry for the samples before and after annealing at 450°C or 900°C for 30 min. The as-deposited Pt film contains a minor amount of carbon (Fig. 4.4a) which may originate from contamination during or after the metal deposition. After annealing at 450°C for 30 min (Fig. 4.4b), the SiC-Pt interface is still sharp, but concentration of Si in the Pt film is higher than it is in the as-deposited sample. The incorporation of Si in the Pt film is related with the rapid transformation of Pt to Pt_3Si at 500°C and will be discussed later.

At 900°C, similar to the backscattering spectrum, a double-layer structure is observed in the secondary ion mass spectrum (Fig. 4.4c). The surface layer is a Pt-Si layer with a minor amount of carbon. The layer near the substrate contains Pt, Si and C. The existence of carbon in this lower layer diminishes the height of the Pt signal near the substrate region in the corresponding backscattering spectrum of the 900°C-annealed sample (Fig. 4.1).

4.1.5. Cross-sectional transmission electron microscopy

Figure 4.5 shows the bright-field cross-sectional transmission electron micrographs of the SiC/Pt samples before (a), and after annealed for 30 min at 400°C (b), 450°C (c), 500°C (d), 600°C (e), and 900°C (f). The as-deposited Pt layer has a columnar structure with grain

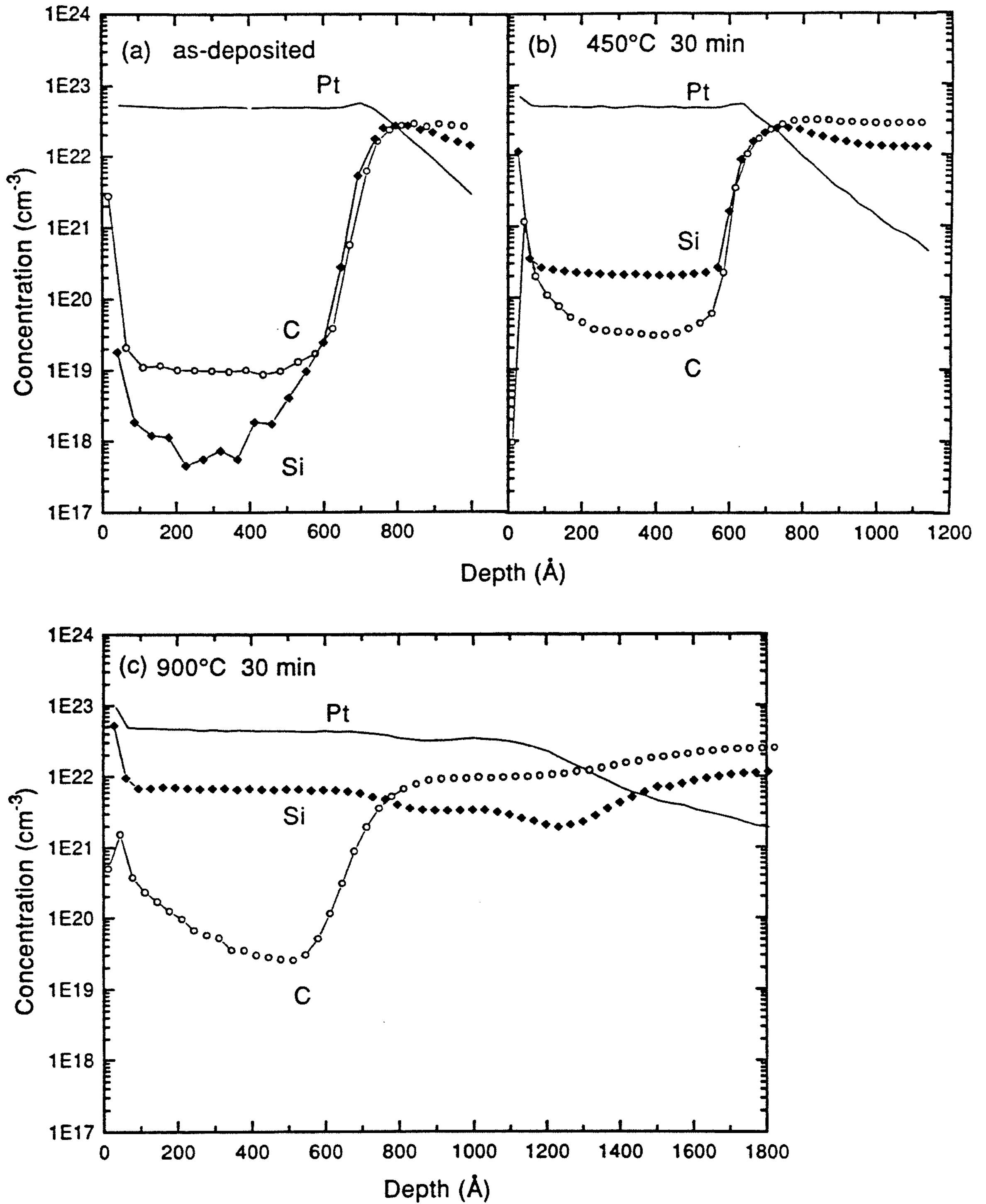

Fig. 4.4 Depth concentration profiles of Pt, Si and C by secondary ion mass spectrometry for <β-SiC>/Pt samples (a) before, and after annealing at (b) 450°C, or (c) 900°C for 30 min.

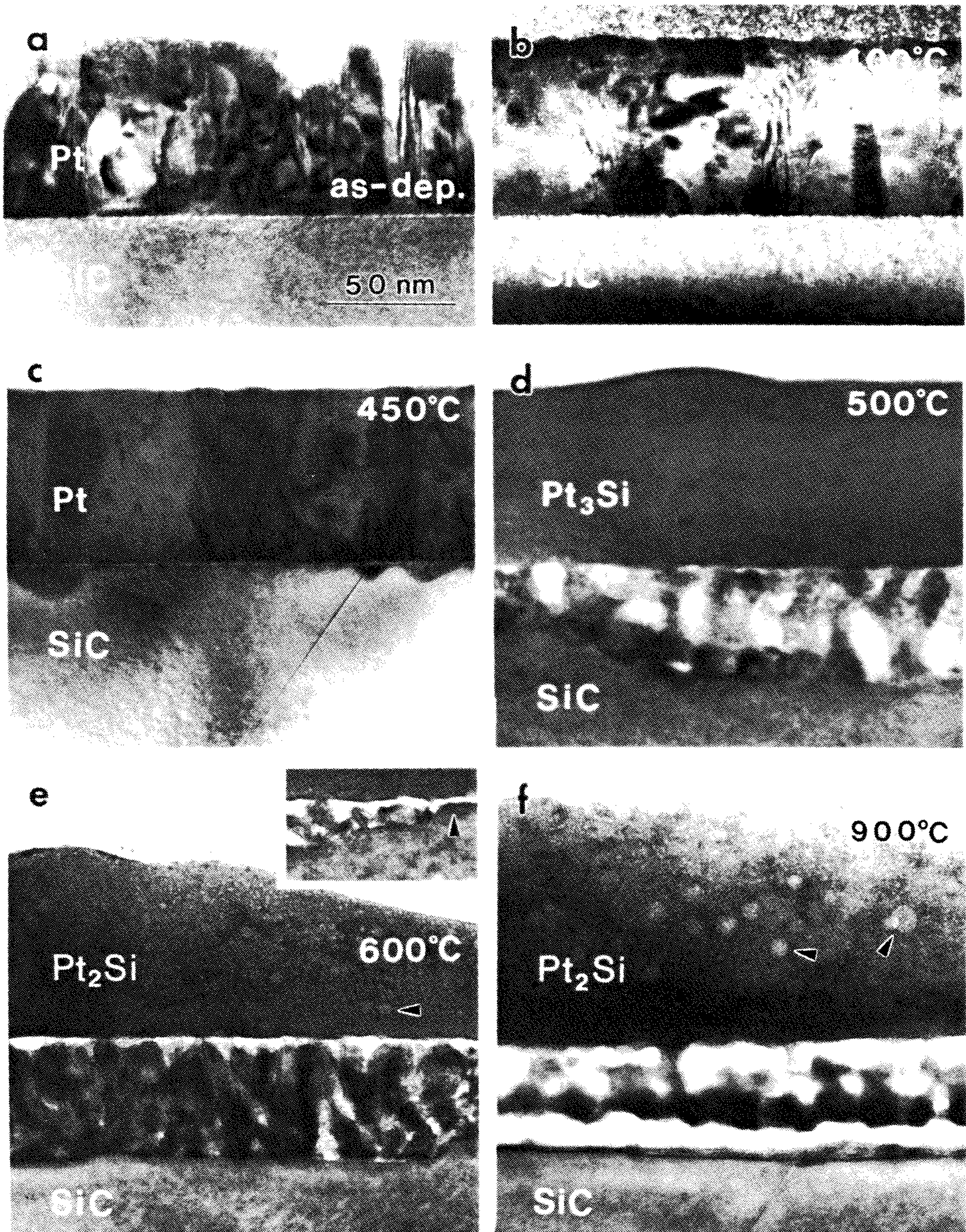

Fig. 4.5 Bright-field cross-sectional transmission electron micrographs of <β-SiC>/Pt samples (a) before, and after annealing for 30 min at (b) 400°C, (c) 450°C, (d) 500°C, (e) 600°C, (f) 900°C. The incident electron beam direction is along the $<110>_{SiC}$ zone axis. All micrographs have the same scale as labeled in (a). The arrows in (e) and (f) indicate the spherically contrasted features in the Pt_2Si layer.

widths of less than half of the film thickness. A light-contrast native oxide (and/or hydrocarbon contamination) layer sits at the interface. Electron beam diffraction reveals that the columnar grains in the as-deposited sample possess a slightly preferred orientation, which is: $\{111\}_{Pt}//\{001\}_{SiC}$. After annealing at 400 or 450°C, the columnar grain structure of the Pt layer is preserved and the texture is enhanced. In the sample heated at 450°C for 30 min, secondary ion mass spectrometry reveals that there is in fact some Si incorporated in the Pt film. Also, an interfacial disturbance with small nuclei penetrating down to the SiC substrate is observed at that temperature (Fig. 4.5c).

The morphology of the sample annealed at 500°C for 30 min changes drastically (Fig. 4.5d). A well-delineated double-layer structure has developed. The bottom layer is laterally nonuniform and consists of a mixture of amorphous (lightly contrasted) and crystalline (dark-contrasted) materials. The upper layer consists of large grains with lateral dimension exceeding 300 nm (by dark-field image). The thickness of the layer is about the same as that of as-deposited Pt layer and the boundaries between two grains are mostly perpendicular to the substrate. This implies that these large grains of the upper layer may have coalesced from the original columnar grains. Convergent beam diffraction shows that the phase of these large grains is Pt_3Si.

The double-layer structure observed at 500°C is still present at 600°C (Fig. 4.5e). These two layers are separated by a sharp interface which corresponds to the original SiC-Pt interface because in some regions it is seen that the bottom layer thins down to zero and merges with the sharp original interface where the SiC is intact (inset of Fig. 4.5e). This observation proves that the reaction proceeds on both sides of the original interface. The upper layer is now (at 600°C) Pt_2Si identified by convergent beam diffraction.

The morphology of the double-layer structure changes a little from 600°C to 900°C (Fig. 4.5f). At 900°C, the upper layer consists of Pt_2Si grains with lateral dimension larger

than 1000 nm (by dark-field image) and increases in thickness. The distribution of the amorphous and crystalline phases in the bottom layer becomes regular and the interface between the upper and the bottom layer is no longer as sharp as it is at 500 or 600°C.

For the samples annealed at 500-900°C, energy-dispersive analysis of x-rays shows that both the upper layer and the dark contrasted region of the bottom layer contain Pt and Si for all samples, establishing that both Si and Pt diffuse across the original SiC-Pt interface during the reaction. The beryllium window on the x-ray detector of our system precludes the detection of elements lighter than sodium. However, when the electron beam is moved from the dark contrasted region to the lightly contrasted region, the Pt and Si signal are significantly reduced. Since secondary ion mass spectrometry shows that a substantial amount of carbon exists near the substrate for the 900°C-annealed sample, we conclude that the dark-contrasted crystallites are mainly Pt-silicide(s) and the lightly-contrasted material is principally carbon. A lamellar structure is observed in some of the lightly contrasted regions by high-resolution imaging. The lamellar structure is a typical structure of graphite [2]. The carbon precipitates therefore consist of amorphous carbon or lamellar graphite.

Some features of spherical contrast (arrows in Fig. 4.5e, f) are seen in the upper layer of the samples annealed 600°C and 900°C. This kind of contrast is typical of voids or material regions containing elements much lighter than the matrix. Secondary ion mass spectrometry does not show a substantial amount of carbon in the surface layer of the 900°C-annealed sample (Fig. 4.4c). The features are therefore more likely to be voids than carbon clusters.

These facts are entirely consistent with the backscattering spectra that suggest a bilayered configuration at 500-900°C (Fig. 4.1), and a presence of both Si and Pt throughout these two layers. The backscattering analysis in effect proves that the structural features

revealed in the cross-sectional micrographs of Fig. 4.5 are typical for the interface as a whole, including the uneven lateral thickness of the lower layer.

High-resolution transmission electron microscopy was employed to explore the initial solid-state SiC-Pt interaction at a very fine scale. Fig. 4.6 shows the cross-sectional, high-resolution micrographs of the SiC/Pt samples before (a), and after annealing at 300°C for 2 h (b), 400°C for 30 min (c), and 450°C for 30 min (d). In all of these micrographs, the contrast of the Pt layer is much darker than that of the SiC substrate; the micrographs are intentionally printed lightly in order to reveal the lattice fringes of the Pt grains.

A few isolated amorphous clusters are seen dispersed along the interface of the as-deposited SiC/Pt sample (Fig. 4.6a). They most probably correspond to the native oxide (and/or hydrocarbon contamination) on the surface of the SiC substrate. After annealing at 300°C for 2 h, a distinct but discontinuous amorphous layer is observed (Fig. 4.6b). It is impossible to tell whether this is the native oxide layer or the very initial interaction between Pt and SiC. After annealing at 400°C for 30 min, a very distinct and continuous 2.5 nm-thick amorphous layer is present at the interface (Fig. 4.6c). The contrast of this amorphous layer is not laterally uniform in the micrograph. Instead, it is alternately dark- and bright-contrasted along the lateral direction. This alternate dark and bright contrast strongly suggests that the amorphous interlayer is a mixture of Pt and Si or C formed by interdiffusion. Also, $\{111\}_{Pt}$ lattice fringes that are parallel to the substrate can be clearly seen. They confirm the presence of a preferential orientation (already seen in the as-deposited Pt film) observed by electron diffraction.

The amorphous interlayer maintains about the same thickness when a new phase starts to nucleate as Fig. 6d shows for the sample annealed at 450°C for 30 min. The same cross-sectional morphology is observed after annealing at 400°C for 2 h. The new crystalline phase evidently grows in contact with the Pt layer, through the amorphous interlayer, and penetrates

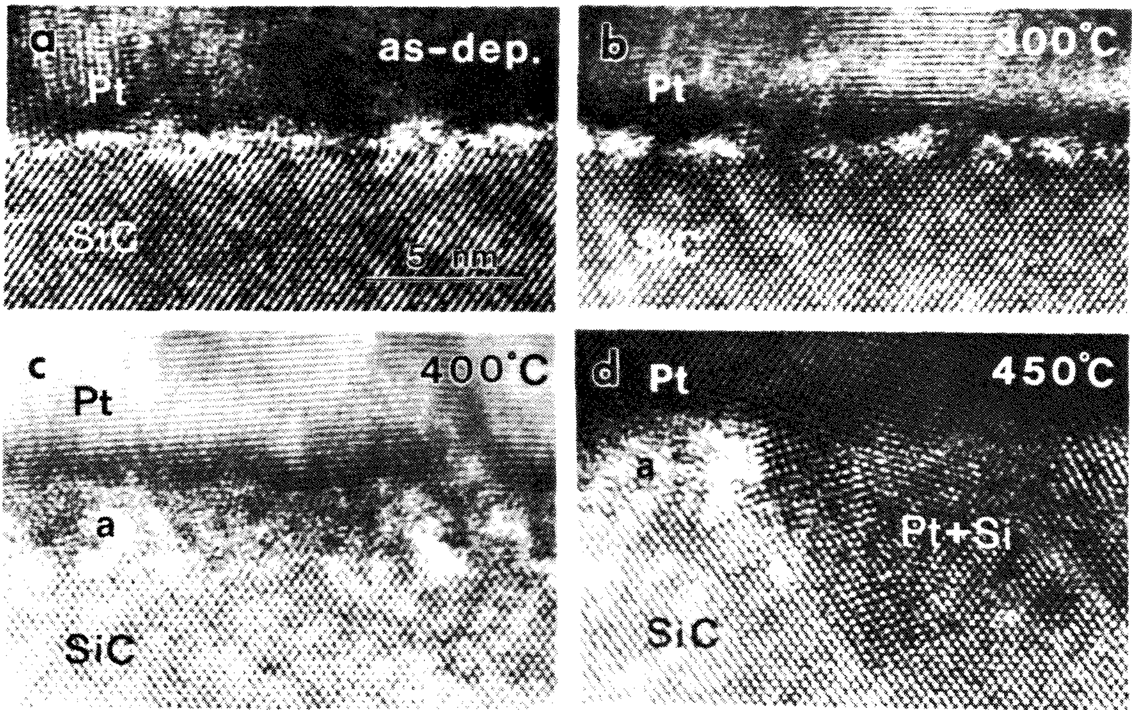

Fig. 4.6 High-resolution cross-sectional transmission electron micrographs of <β-SiC>/Pt samples (a) before, and after annealing at (b) 300°C for 2 h, (c) 400°C for 30 min, and (d) 450°C for 30 min. The incident electron beam direction is along the <110>$_{SiC}$ zone axis. All micrographs have the same scale as labeled in (a).

down into the SiC substrate. The nuclei tend to have lattices aligned in the same direction as their adjacent Pt grains. The SiC lattice fringes are disturbed inside the nuclei.

4.2 Thermodynamic Considerations

The thermodynamic stability of a metal-compound semiconductor system can be predicted by the corresponding phase diagram. In the case of Pt-Si-C, an approximate phase diagram has been established experimentally by heating bulk quantities of platinum silicides and SiC with carbon and examining the phases formed during cooling from above the liquidus temperatures [3]. This approximate Pt-Si-C phase diagram is reproduced in Fig. 4.7. According to the phase diagram, the final equilibrium phases should be PtSi, SiC and carbon for a thin Pt film deposited on a SiC substrate. Our x-ray diffraction result for the SiC/Pt sample annealed at 1000°C for 30 min shows product phases of PtSi and Pt_2Si. Although no secondary ion mass spectra were taken, we believe that carbon precipitates also exist in the 1000°C-annealed sample, as they do in the samples annealed at 500-900°C we analyzed. Upon annealing at 1000°C for 30 min, the system has thus evidently not reached its thermodynamic equilibrium state yet because Pt_2Si still exists. Further annealing is apparently necessary to transform the residual Pt_2Si to PtSi and reach thermodynamic equilibrium.

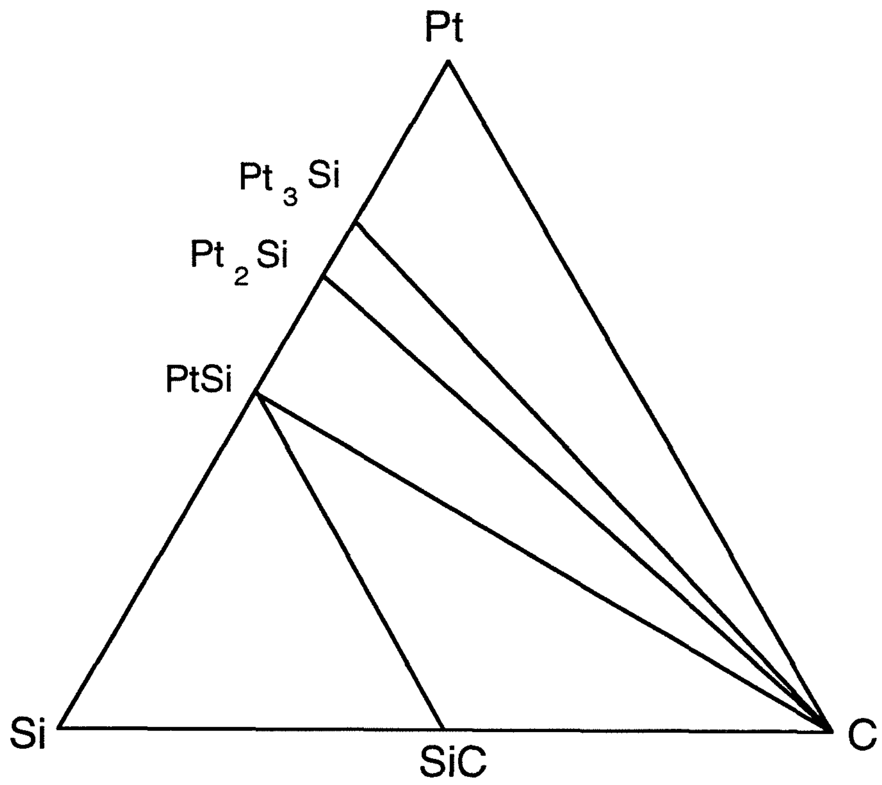

Fig. 4.7 A reproduced ternary Pt-Si-C phase diagram from Ref. 3.

4.3 Formation of Carbon Precipitates

Pt does not form any compound with carbon so that carbon is expected to segregate out when Pt reacts with SiC and forms silicide(s). Carbon-like precipitates begin to be visible after 2 h at 450°C. At T≥500°C (Fig 5d-f), the bottom layer contains significant amounts of amorphous or lamellar-structured material, which are the typical structural forms for amorphous carbon or graphite. This finding is consistent with the results obtained for solid-state reactions of bulk Pt and SiC [4], where it is found that alternating layers of silicide and carbon form in the reaction zone.

In fact, all near-noble metals form stable silicides but do not form carbides. The formation of silicides and carbon precipitates is also observed for the solid-state reactions between SiC and Pt [4], Ni [4, 5] or Co [4, 6]. The microstructure and chemical composition of the metal-semiconductor interface are crucial for the electrical performance of the metal contacts. From the present study of the thermal reaction sequence of a thin Pt film with β-SiC, it is not surprising that the barrier height of Pt Schottky contacts is found to change with increasing annealing temperature [7]. Due to the similar chemical reactivity of the near-noble metals, the electrical performance of Ni, Co, Pd ... contacts on SiC may be also thermally unstable.

4.4 Interdiffusion Between SiC and Pt Upon Annealing

By secondary ion mass spectrometry, it is found that a small amount of Si is distributed throughout the Pt film when the sample is annealed at 450°C (Fig. 4.4b). Because the Pt film has a columnar grain structure, Si atoms may first diffuse along the grain boundaries, possibly followed by a lateral diffusion into the Pt lattice. The overall concentration of ~ 1 at.% Si extracted from the secondary ion mass spectrum at 450°C is

roughly consistent with the bulk solid solubility of Si in Pt (maximum of 1.4 at.% at 830°C [1]). Between 450 and 500°C and 30 min annealing, most of the Pt overlayer transforms quite suddenly to Pt_3Si. Formation of this Pt_3Si layer at 500°C involves both fast diffusion (to reach the composition of Pt:Si=3:1) and grain growth. The mechanism of this transformation remains unknown.

The upper layer transforms to Pt_2Si at 600°C while the lower layer remains the carbon-silicide mixed structure. Since we know that the sharp interface between the upper and lower reacted layers corresponds to the original interface, the amount of Pt that remains in the upper reacted layer can be obtained from the backscattering spectra. We find that about 76±5% of the Pt stays in the upper layer of the 500°C-annealed sample and that 68±5% of the Pt remains in the upper layer of the 600°C-annealed sample (Fig. 4.1). The original Pt thickness is 70 nm. When 76% of Pt reacts with SiC and forms Pt_3Si at 500°C, the thickness of the resulting Pt_3Si layer expected from bulk density consideration is 68 nm. When 68% of Pt reacts with SiC and forms Pt_2Si at 600°C, the expected thickness of the Pt_2Si layer is 71 nm. These thicknesses are consistent with the cross-sectional micrographs where the upper reacted layer maintains roughly the same thickness as the original Pt thickness (~ 70 nm) in the 500°C- or 600°C-annealed sample (Fig. 4.5a, d and e).

Because the amount of Pt that remains in the upper layer is known, one can evaluate the amount of Si that has to diffuse into it to form Pt_3Si above the interface at 500°C (or to form Pt_2Si at 600°C) and the amount of Pt that has diffused across the interface to form platinium silicides below it. One finds that the ratio of these amounts is close to unity, at either 500°C or 600°C. Both Pt and Si diffuse across the original SiC-Pt interface during the solid-state reaction up to 600°C, and neither of them is dominant. In contrast, for the Si-Pt system, Pt is the dominant diffusion species during Pt_2Si formation [8] while Si is the dominant diffusion species during PtSi growth [9].

At 600 or 900°C, many spherically contrasted features, most likely voids, appears in the upper Pt_2Si layer. Their occurrence coincides with the transformation of Pt_3Si to Pt_2Si. These voids may thus arise from the condensation of vacancies that accompany the diffusion of Pt down to the SiC substrate. At 900°C, the voids have grown in size and the lower reacted layer has shrunk (Fig. 4.5f), as if there were a transport of vacancies from the lower layer to the upper layer. Most of the carbon precipitates are now graphitic instead of amorphous compared with the 600°C-annealed sample. The large number and size of the voids increases the thickness of the Pt_2Si layer to about 100 nm.

4.5 Formation of the Amorphous Interlayer

It has long been suggested that there possibly exists initially a thin amorphous layer at the metal-semiconductor interface [10]. A 3-nm-thick amorphous intermixed layer is indeed observed in the as-deposited Pt on Si [11] or GaAs [12] substrate. In our case of the SiC-Pt reaction, a distinct amorphous layer about 2.5 nm thick is observed at the SiC-Pt interface after annealing at 400°C for 30 min (Fig. 4.6c). The formation of the amorphous layer is evidently kinetically permissible in this system, although it is thermodynamically metastable [13] so that a crystalline phase will nucleate during the subsequent annealing. This occurs at 450°C for 30 min or at 400°C for 2 h. A new phase nucleates adjacent to the Pt layer and penetrates into or across the amorphous layer towards the SiC while the undisturbed amorphous interlayer between the newly-formed nuclei maintains the same thickness (Fig 4.6d). After 450°C for 2 h (micrograph not shown), the size of the nuclei becomes large enough to permit their analysis by energy-dispersive analysis of x-rays. We find that both Pt and Si are in the nuclei. They are thus formed mainly by the diffusion of Pt into the SiC substrate.

REFERENCES (Chapter 4)

1. T. B. Massalski, editor-in-chief, *Binary Alloy Phase Diagrams* (ASM International, Metal Park, OH, 1990), second edition.
2. K. C. Thompson-Russell and J. W. Edington, in *Monograph in Practical Electron Microscopy for Materials Science*, edited by J. W. Edington, vol. 5, p. 21, Philips Technical Library, Holland, 1977.
3. A. W. Searcy and L. N. Finnie, J. Am. Ceram. Soc. 45, 268 (1962).
4. T. C. Chou, A. Joshi, and J. Wadsworth, J. Mat. Res. 6, 796 (1991).
5. R. C. J. Schiepers, F. J. J. van Loo, and G. de With, J. Am. Ceram. Soc. 71, C-284 (1988).
6. L. M. Porter, Ph.D. Thesis, p. 110, North Carolina State University, 1993.
7. N. A. Papanicolaou, A. Christou, and M. L. Gipe, J. Appl. Phys. 65, 3526 (1989).
8. K. Affolter, X.-A. Zhao, and M-A. Nicolet, J. Appl. Phys. 58, 3087 (1985).
9. J. E. McLeod, M. A. E. Wandt, R. Pretorious and C. M. Comrie, J. Appl. Phys. 72, 2232 (1992).
10. R. M. Walser and R. W. Bené, Appl. Phys. Lett. 28, 624 (1976).
11. J. R. Abelson, K. B. Kim, D. E. Mercer, C. R. Helms, R. Sinclair and T. W. Sigmon, J. Appl. Phys. 63, 689 (1988).
12. D-H. Ko and R. Sinclair, J. Appl. Phys. 72. 2036 (1992).
13. K. N. Tu and S. R. Herd, Phys. Rev. B, 43, 1198 (1991).

Chapter 5
Reaction of Ta Thin Film With Single Crystalline (001) β-SiC

5.1 Reaction Characterization

5.1.1 Backscattering spectrometry

Figure 5.1 shows the backscattering spectra for the SiC/Ta samples before and after annealing at 900°C for 1 h, 1000°C for 1 h and 1100°C for 30 min. The total counts of the Ta signals in all spectra were kept constant based on the assumption that no Ta is lost during annealing. The spectra of the samples annealed at 600-800°C for 1 h overlap perfectly with that of the as-deposited sample and are not shown. There is thus no detectable reaction by backscattering spectrometry between Ta and SiC upon annealing for 1 h up to 800°C. At 900°C, a significant reduction of the Ta signal height is observed in conjunction with the appearance of a small step in the Si signal near the substrate region that indicates the formation of Ta-Si compound(s). A reduction of the Ta signal height throughout the whole Ta layer means that another element is incorporated uniformly throughout that layer. If the element were Si, its signal in the 1.4 to 1.7 MeV range should rise above the background signal to about 10% of the height at 1.3 MeV, corresponding to about 15 at.% Si in the Ta layer. No such increase in the Si signal is observed. The element incorporated in the Ta layer is thus most certainly carbon, in which case the atomic concentration must approach 25 at.%. The carbon signal is too weak to be seen superimposed as it is over the Si signal of the substrate, but it is resolved by secondary ion mass spectrometry (see 5.1.3).

The backscattering profile of the Ta signal for the sample annealed at 1000°C for 1 h has three steps with the lowest signal height in the mid-layer (Fig 5.1, circle line). A Si signal step is shown at backscattering energies between 1.37 and 1.57 MeV. From the energy loss, this Si step matches the middle Ta layer from 2.4 to 2.6 MeV. By the height

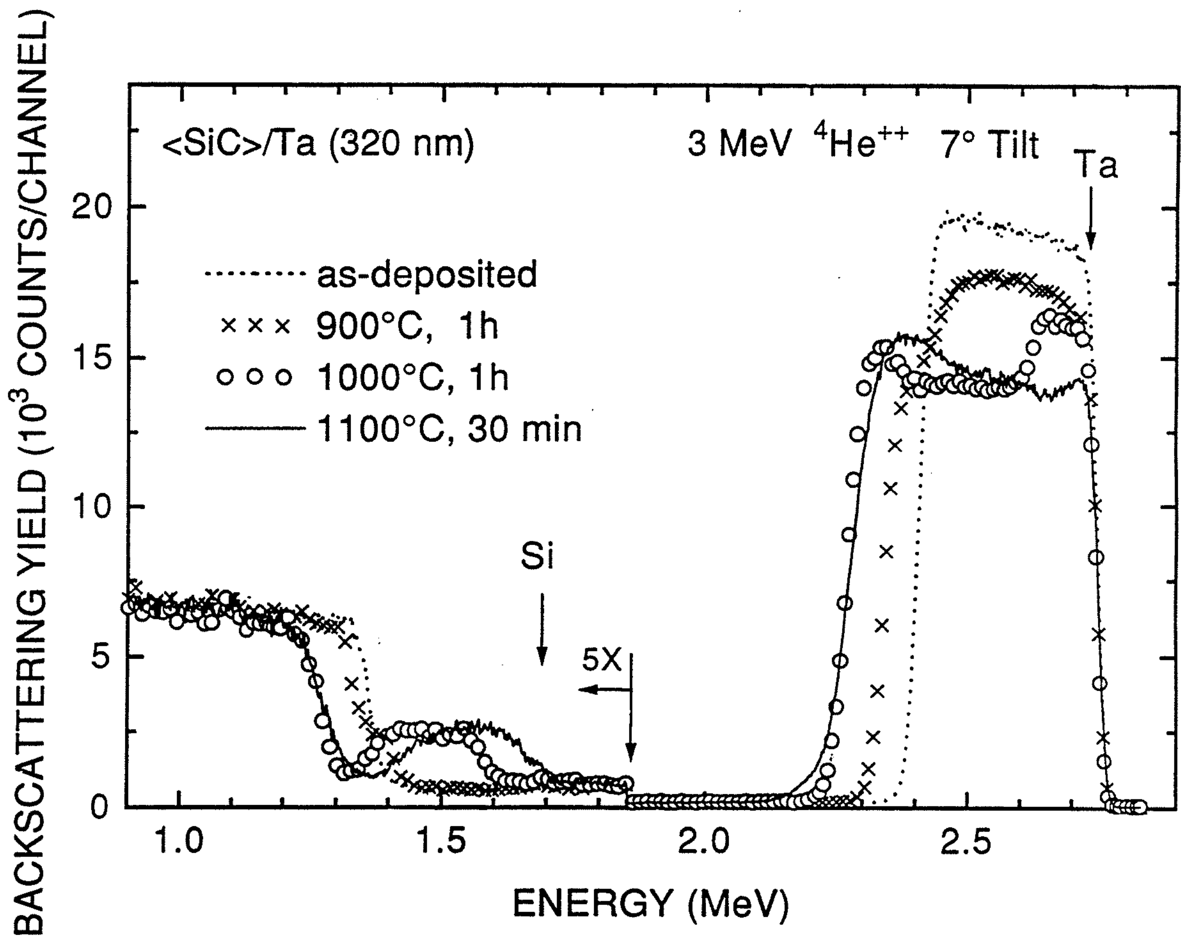

Fig. 5.1 3 MeV $^4He^{++}$ backscattering spectra of <β-SiC>/Ta samples before and after vacuum annealing at 900°C for 1 h, 1000°C for 1 h and 1100°C for 30 min. The samples were tilted by 7° against the incident beam direction. The scattering angle of the detected particles is 170°.

ratio of the Si signal to the Ta signal in that mid-layer, an atomic ratio of Si/Ta ~0.62 is extracted for that layer. For the whole reacted layer, the average Si/Ta ratio is ~0.32, obtained by integrating the total number of counts of the Si signal and the Ta signal. Since the carbon signal of this sample cannot be resolved by backscattering spectrometry, the full composition for each sublayer in the reacted zone is not available. Data presented in sections 5.1.3 and 5.1.4 reveal that the middle layer actually consists structurally of two distinct sublayers of nearly identical atomic composition.

In the sample annealed at 1100°C for 30 min, the layered structure is no longer distinct. Si is concentrated near the surface of the reacted layer but the overall Si/Ta ratio (~0.33) changes insignificantly in comparison with that of the 1000°C/1 h-annealed sample. The backscattering spectrum of the sample annealed at 1200°C for 1 h is not shown because it is uninformative due to the lateral nonuniformity of the reacted layer (see Figs. 5.5 and 5.6).

5.1.2 X-ray diffraction

The x-ray diffraction spectra of the samples before and after annealing at 900°C, 1000°C, 1100°C and 1200°C are shown in Fig. 5.2. X-ray diffraction reveals that both pure Ta (bcc) and impurity-stabilized β-Ta (tetragonal) exist in the as-deposited SiC/Ta sample. From the full width at the half maximum of the $(211)_{Ta}$ peak ($2\theta = 83°$), the grain size of the as-deposited Ta layer is about 14 nm.

At 900°C, diffraction peaks of Ta_2C and metastable Ta_5Si_3 develop. The Ta_2C phase here is a disordered phase of the Fe_2N structure type and the metastable Ta_5Si_3 phase is a carbon-stabilized phase with hexagonal Mn_5Si_3 structure (referred to as Ta_5Si_3:C from here on). Because some of the lattice spacings of Ta and β-Ta are similar to those of Ta_2C, there may be a minor amount of unreacted Ta or β-Ta in the sample as well. In fact, the

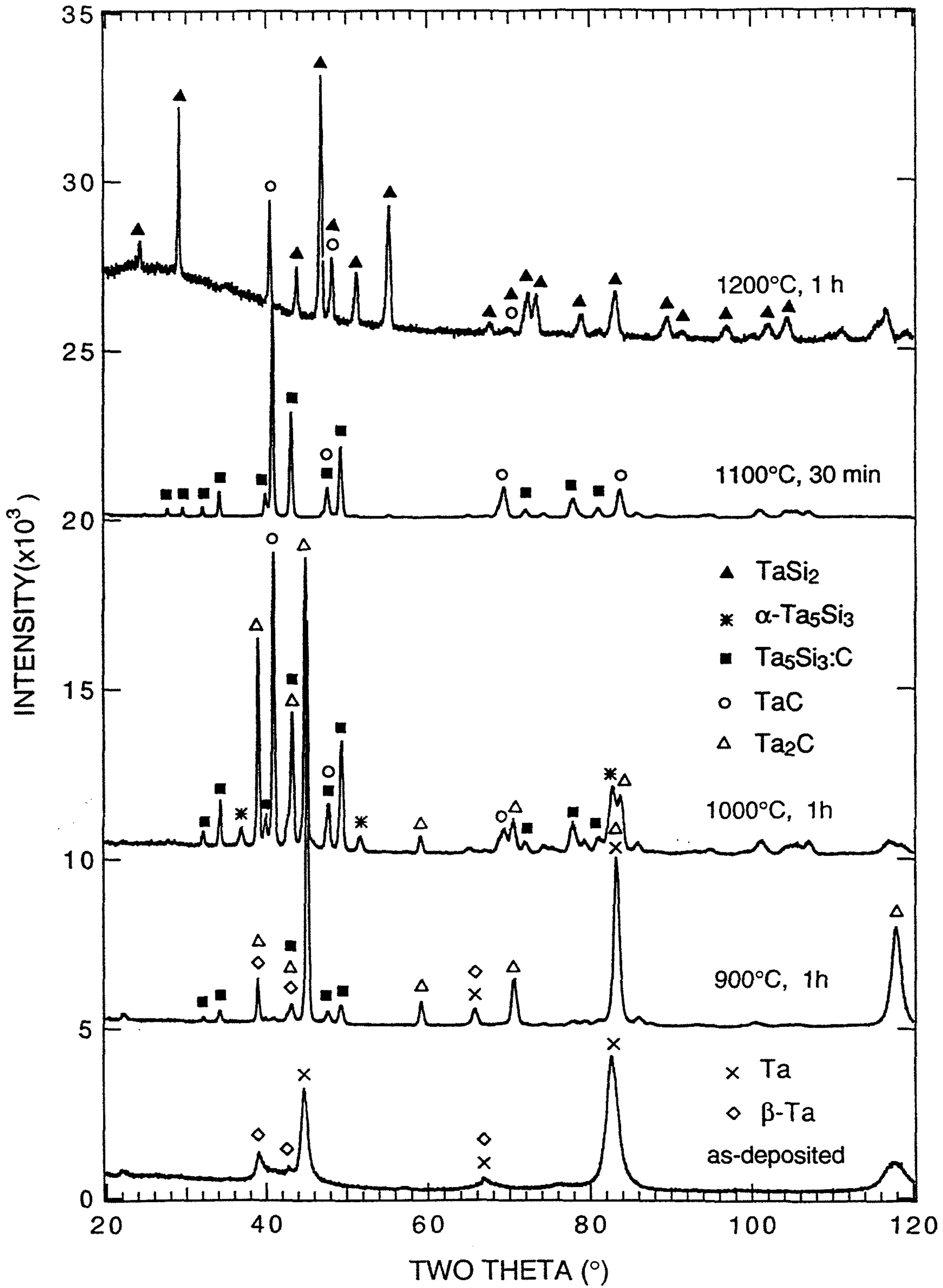

Fig. 5.2 X-ray diffraction spectra for Co-Kα radiation of <β-SiC>/Ta samples before and after annealing at 900°C for 1 h, 1000°C for 1 h, 1100°C for 30 min and 1200°C for 1 h.

backscattering spectrum shows that the carbon incorporated in the Ta layer is about 25 at.%, which is below the homogeneity range of Ta_2C (29-33 at.% of C [1]). It is thus clear that there must be unreacted Ta or β-Ta in the reacted layer.

The phases formed in the samples annealed at 1000°C for 1 h are Ta_2C, TaC, Ta_5Si_3:C and a little of α-Ta_5Si_3. The Ta_5Si_3:C and α-Ta_5Si_3 phases must correspond to the "mid-layer" seen by backscattering spectrometry whose Si/Ta atomic ratio is about 0.6. After annealing at 1100°C for 30 min, the product phases are TaC and Ta_5Si_3:C. The Ta_2C and α-Ta_5Si_3 phases disappear upon this heat treatment. After annealing at 1200°C for 1 h, diffraction peaks of TaC and $TaSi_2$ are observed. Since TaC and $TaSi_2$ are the final equilibrium products predicted by the phase diagram (see below), the SiC-Ta system has thus reached its equilibrium state after annealing at 1200°C for 1 h.

5.1.3 Secondary ion mass spectrometry

Figure 5.3 shows the depth profiles of Ta, Si and C before (a), and after annealing at (b) 900°C/1 h, (c) 1000°C/1 h, and (d) 1100°C/30 min obtained by secondary ion mass spectrometry. The carbon and Si shown in the Ta layer of the as-deposited sample (Fig. 5.3a) are attributed to contamination during profiling. The sluggish fall of Ta seen in the SiC region is an artifact from the low sputtering rate of Ta in comparison with those of silicon and carbon.

After annealing at 900°C for 1 h (Fig. 5.3b), a Si step appears near the substrate, consistent with the result of backscattering spectrometry. A similar step is present in the carbon profile, which additionally displays a minimum midway to the surface. The phase(s) in contact with the SiC substrate should be Ta_5Si_3:C, and maybe Ta_2C as well. Ta_2C should be the compound on the surface. The high carbon concentration near the surface (compared to that of Si) strongly implies that carbon is the dominant moving species at 900°C.

For the 1000°C/1 h-annealed sample (Fig. 5.3c), a well-defined, four-layered structure is observed in the depth profiles. The main elemental components of the sublayers, from

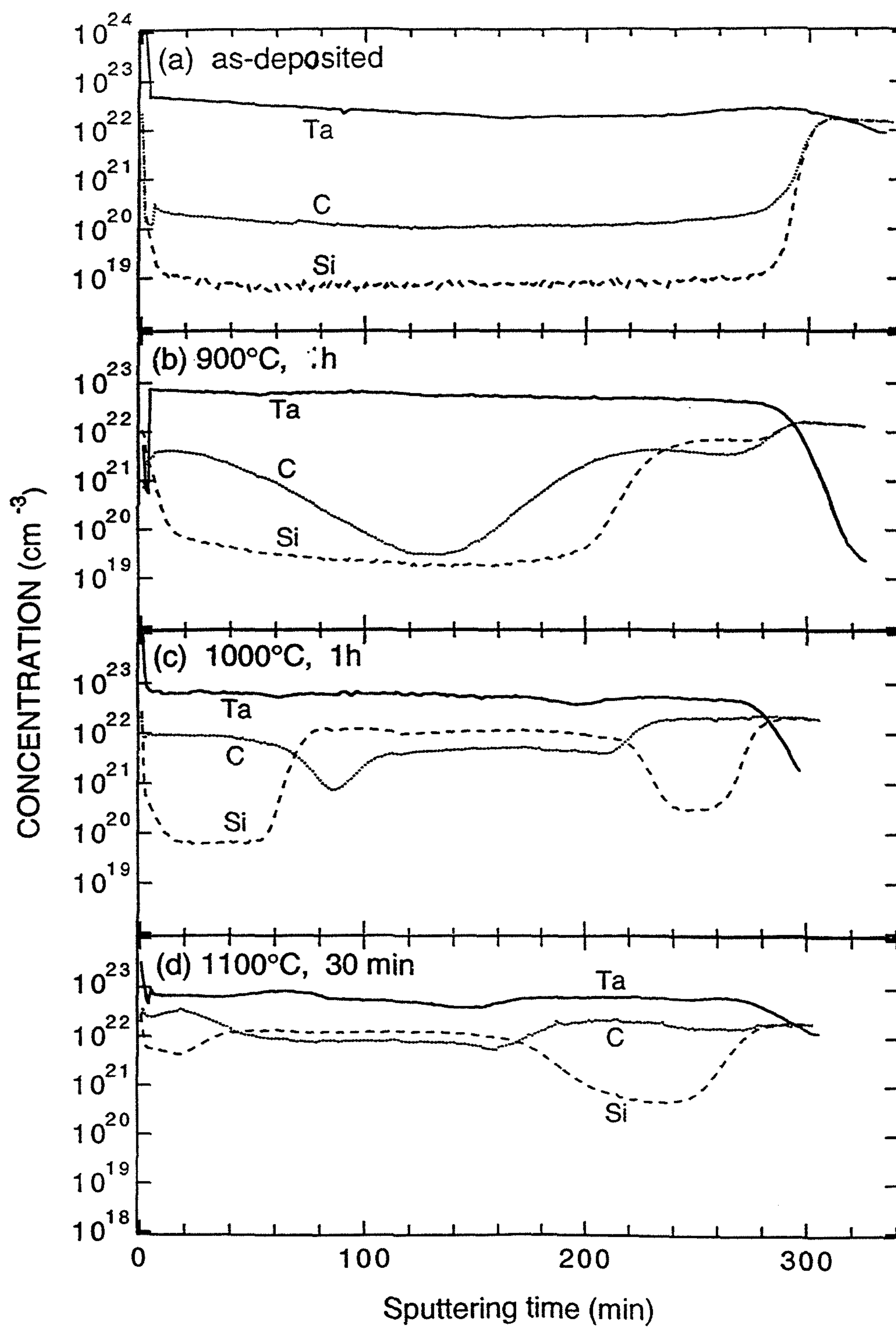

Fig. 5.3 SIMS depth profiles of Ta, Si and C for <β-SiC>/Ta samples (a) before, and after annealing at (b) 900°C for 1 h, (c) 1000°C for 1 h, and (d) 1100°C for 30 min.

the substrate to the surface, are Ta-C, Ta-Si-C, Ta-Si, and Ta-C. A comparison with the result of x-ray diffraction shows that the phases of these four sublayers should correspondingly be TaC, Ta_5Si_3:C, α-Ta_5Si_3 and Ta_2C. Upon annealing at 1100°C for 30 min (Fig. 3d), the bottom TaC layer broadens and the top Ta-C layer now contains a notable amount of Si. The remainder of the reacted layer is Ta_5Si_3:C. The sublayers are not clearly defined and there may exist two-phase regions.

5.1.4 Cross-sectional transmission electron microscopy

Figure 5.4a is a cross-sectional transmission electron micrograph of the sample annealed at 1000°C for 1 h. Part of the surface of the reacted layer has been milled away during sample preparation. A horizontal line marks its original position. Interfaces are similarly highlighted. A micrograph of improved clarity for the region near the SiC substrate is shown in Fig. 5.4b. The SiC substrate in that figure is so thin that its contrast is very light. In agreement with the result of secondary ion mass spectrometry, the cross-sectional morphology of the sample shows four sublayers in the reaction zone. The sequence and thicknesses are, from the SiC substrate to the surface and by comparison with the x-ray diffraction and SIMS results, TaC(110nm)/Ta_5Si_3:C(235nm)/α-Ta_5Si_3(40nm) /Ta_2C(110nm).

The TaC and Ta_2C layers have grains of a size comparable to their layer thickness (~100 nm). The interface between the TaC layer and the SiC substrate is sharp and laterally very uniform. On the other hand, the Ta_5Si_3:C grains are small and equiaxial in the region next to the TaC layer, then become elongated towards to the surface. In the α-Ta_5Si_3 layer, the grains get small again. There are lightly-contrasted, bubble-like features distributed in the Ta_5Si_3:C and α-Ta_5Si_3 grains. Near the TaC/Ta_5Si_{33}:C interface, large, rounded features (30-60 nm in diameter) with very light contrast are observed. The lightly-contrasted features are usually voids or objects of light-mass elements. It is difficult to unambiguously identify these features due to the complexity of the cross-sectional sample. The comparison with the

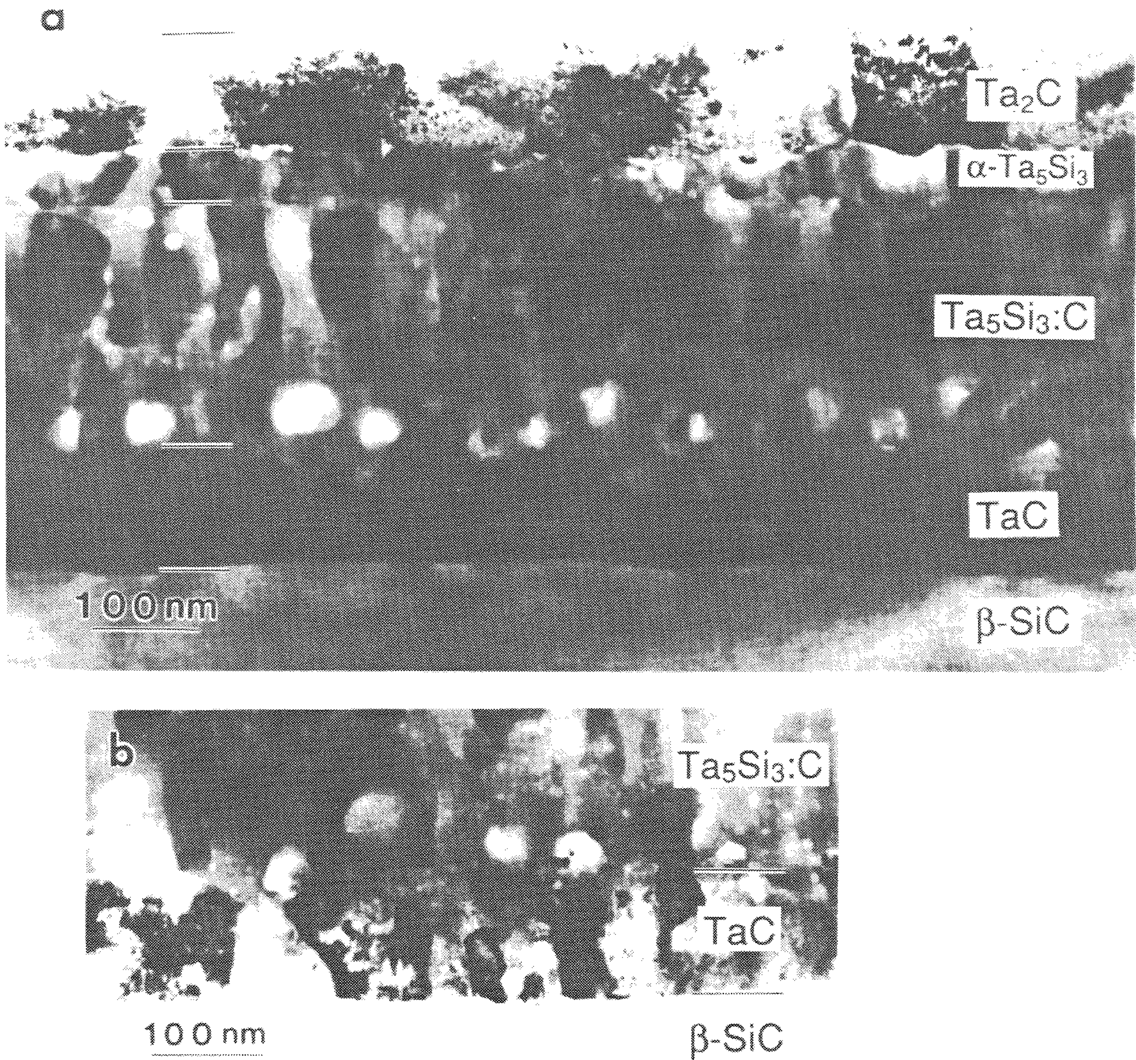

Fig. 5.4 (a) A bright-field cross-sectional transmission electron micrograph of the <β-SiC>/Ta sample after annealing at 1000°C for 1 h; (b) another micrograph on a thin area near the SiC substrate of the same sample shown in (a). The horizontal lines in the figures mark the position of the interfaces and of the surface.

cross-sectional scanning electron micrograph of the 1100°C/30 min sample (Fig. 5.6a) shows that the large, rounded features are, in fact, voids.

5.1.5. Scanning electron microscopy

Figure 5.5 (a), (b), (c), and (d) are scanning electron micrographs of the surface morphology of the SiC/Ta samples before and after annealing at 1000°C for 1 h, 1100°C for 30 min and 1200°C for 1 h, respectively. The surfaces of the as-deposited and 1000°C-annealed samples are smooth and featureless. After annealing at 1100°C for 30 min, some hillocks appear on the surface with diameters of about 1-2.5 μm. The surface of the 1200°C-annealed sample appears dull to the eye. The scanning electron micrograph suggests that the reacted layer agglomerates during that heat treatment. Energy-dispersive spectrometry shows that the agglomerates consist mainly of Ta and Si. In the remaining matrix areas, the Ta signal is also detected, but the Si signal is diminished. Carbon is significant only in the matrix areas. The agglomerates therefore are $TaSi_2$, and the matrix area should be TaC.

Figure 5.6 (a) and (b) are cross-sectional scanning electron micrographs of the SiC/Ta samples after annealing at 1100°C for 30 min and 1200°C for 1 h, respectively. The hillocks seen on the surface of the 1100°C/30 min sample (Fig. 5.5c) reveal themselves as a buckling of a part of the reacted layer. This buckling initiates at a depth within the reacted layer below which the reacted layer is still intimately in contact with the SiC substrate. A row of voids is observed in that still adhering part of the reacted layer. They are located at about one third of the total layer thickness from the SiC interface, which identifies them as the large, rounded features observed at the TaC-Ta_5Si_3:C interface in the cross-sectional transmission electron microsgraph of the 1000°C/ 1 h sample (Fig. 5.4). We therefore identify those large, rounded features as voids, too.

The cross section of the sample annealed at 1200°C for 1 h (Fig. 5.6b) shows that the grains of the reacted layer are about 0.5-1 μm in size with voids in between. The SiC

(a) as-deposited

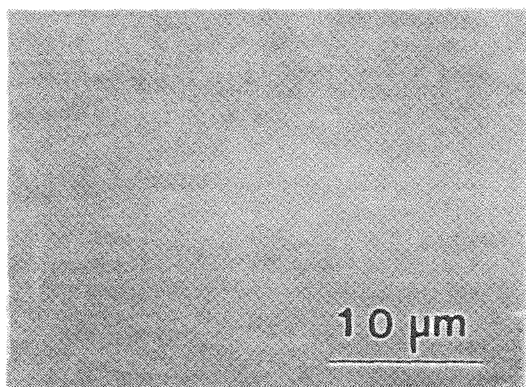

(b) 1000 °C, 1 h

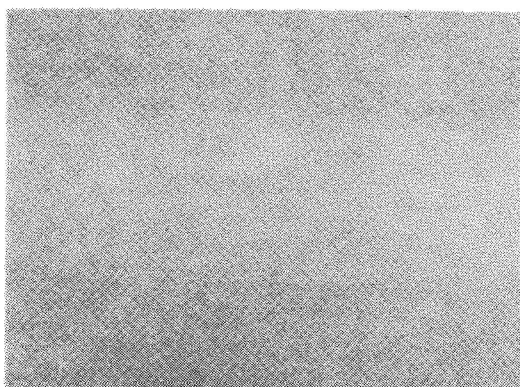

(c) 1100 °C, 30 min

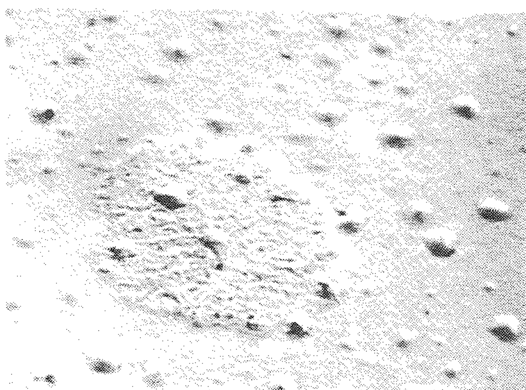

(d) 1200 °C, 1h

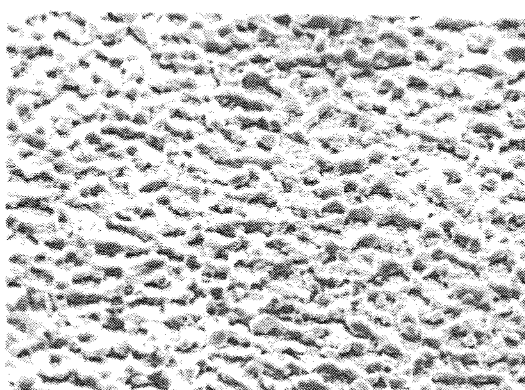

Fig. 5.5 Scanning electron micrographs on the surface of the <β-SiC>/Ta samples before (a), and after annealing at (b) 1000°C for 1 h, (c) 1100°C for 30 min, and (d) 1200°C for 1 h. The scale marked in (a) also applies to (b), (c) and (d).

(a) 1100°C, 30 min

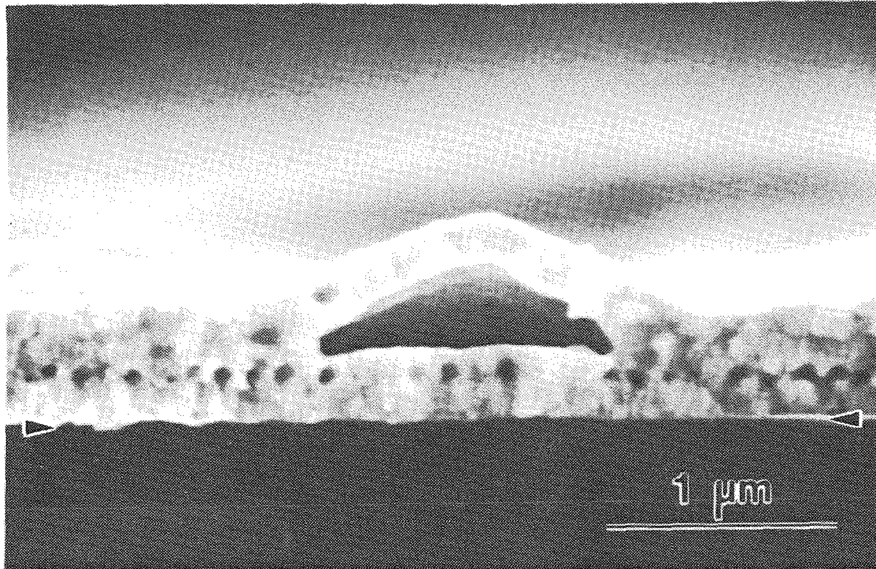

(b) 1200°C, 1h

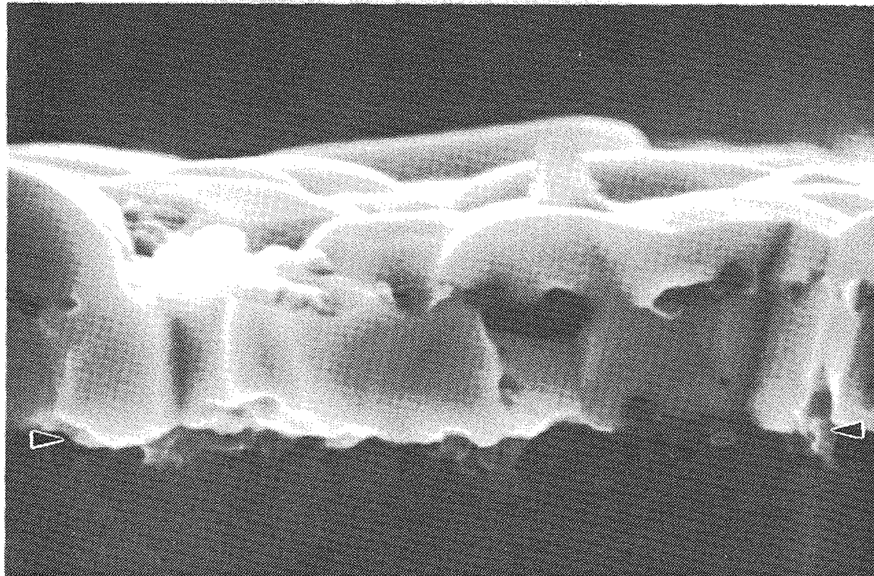

Fig. 5.6 Scanning electron micrographs on the cross section of the <β-SiC>/Ta samples after annealing at (a) 1100°C for 30 min and (b) 1200°C for 1 h. The interface between the SiC substrate and the reacted layer is marked by arrows. The scale marked in (a) also applies to (b).

interface is now laterally quite irregular. Voids are also present at the interface or in the SiC substrate.

The evolution of the thermal reaction between Ta and β-SiC is summarized in Table 5.1 which lists the phases and the layer sequences of the reaction products observed before and after annealing at 800-1200°C.

Table 5.1 Evolution of the thermal reaction between Ta and β-SiC before and after annealing at 800-1200°C.

Temperature / time	Phases and the layer sequence
as-deposited	<β-SiC> ∣ Ta
800°C / 1 h	<β-SiC> ∣ Ta
900°C / 1 h	<β-SiC> ∣ Ta_5Si_3:C & Ta_2C ∣ β-Ta & Ta_2C
1000°C / 1 h	<β-SiC> ∣ TaC ∣ Ta_5Si_3:C ∣ α-Ta_5Si_3 ∣ Ta_2C
1100°C / 0.5 h	<β-SiC> ∣ TaC & Ta_5Si_3:C
1200°C / 1 h	<β-SiC> ∣ TaC & $TaSi_2$

5.2 Thermodynamic Considerations

The solid-state reaction between tantalum and SiC is expected to be complex because Ta forms both very stable carbides and silicides. As always, a phase diagram is essential to properly interpret the results of such a reaction. Figure 5.7 is the 1000°C isothermal section of the Ta-Si-C phase diagram experimentally determined by Schuster [2]. This isothermal section applies at temperatures up to 1823°C because the tie lines appear unchanged in the 1823°C isothermal section published by Brewer and Krikorion [3]. The Ta-SiC interface

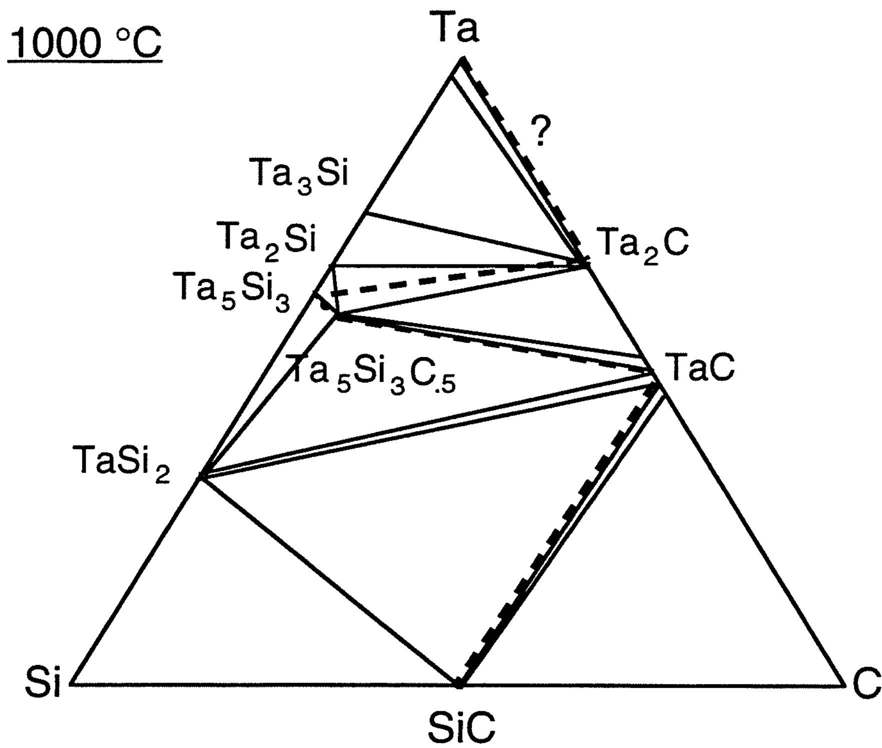

Fig. 5.7 The 1000°C isothermal section of the Ta-Si-C ternary phase diagram [2]. The diffusion path for the reaction between Ta and SiC by annealing at 1000°C for 1 h is drawn by the dashed line.

is thermodynamically unstable because there is no tie line between Ta and SiC. With a thin Ta film deposited on a thick SiC substrate, the equilibrium phases are TaC, $TaSi_2$ and unreacted SiC. This final state is reached by annealing at 1200°C for 1 h. The only ternary compound indicated in the isothermal section is $Ta_5Si_3C_{0.5}$. This compound has the Mn_5Si_3-structure type and the lattice parameters are similar to those of the carbon-stabilized Ta_5Si_3:C phase observed in our experiment. We therefore believe that they are the same compound except that the actual carbon content in our film is uncertain; that is why we describe it as Ta_5Si_3:C.

5.3 Diffusion Path at 1000 °C

After annealing at 1000°C for 1 h, the whole Ta layer (320 nm) reacts and a four-layered structure of the form β-SiC/TaC/Ta_5Si_3:C/α-Ta_5Si_3/Ta_2C is observed. Nb, which is of the same transition metal group as Ta, is reported to form a SiC/(NbC+Nb_5Si_4C)/Nb_5Si_3/Nb_2C/Nb structure after annealing a 1 μm Nb film on α-SiC at about 1100°C [4]. With a 1 μm-thick Ta film deposited on α-SiC, the whole Ta layer had reacted and resulted in a layered structure of SiC/Ta-C/Ta-Si-C/Ta-C upon annealing at 1100°C for 4 h although the product phases were not clearly identified [5]. These results indicate that formation of the multilayered structure may be a general trend for the thermal reaction of the vanadium group metals (V, Nb and Ta) with SiC.

The β-SiC/TaC/Ta_5Si_3:C/α-Ta_5Si_3/Ta_2C structure can be represented by a diffusion path on the Ta-Si-C phase diagram (the dashed line in Fig. 5.7). The diffusion path connects the product compounds in the sequence in which they appear in the diffusion zone of a diffusion couple [6-8]. A dashed line parallel to a tie line represents an interface between two phases in local equilibrium [6, 7]. In Fig. 5.7, the dashed line that connects Ta and Ta_2C has a question mark because Ta was not positively identified by x-ray diffraction after 900°C

annealing. This path is the probable one, however, because Ta_3Si was never detected. The entire diffusion path indicates that all interfaces except that between α-Ta_5Si_3 and Ta_2C are in local thermodynamic equilibrium. The presence of the α-Ta_5Si_3 phase is thus kinetically induced and may be absent under slightly altered annealing conditions. It would be worthwhile to study the diffusion path on a bulk SiC-Ta diffusion couple and compare it with the present results.

5.4 Formation of Voids

Voids are observed both in the 1000°C-annealed sample (Fig. 5.4) and the 1100°C-annealed sample (Fig. 5.6a). The presence of the voids, combined with the intrinsic or thermal stresses induced by reaction or annealing, often result in the buckling of thin-film layers [9]. This is the reason why "hillocks" are observed on the surface of the 1100°C/30 min sample.

The reason for the formation of the voids is not clear. One possibility is that they originate by condensation of vacancies that form due to strong dissimilarities in moving rates of the diffusing species (Kirkendall effect). At 1000°C, since the average atomic ratio of Si/Ta for the whole reacted layer is known by backscattering spectrometry (Si/Ta ~ 0.32) and the initial Ta thickness is 320 nm, the thickness of the SiC substrate that has been consumed can be calculated and is 117 nm, assuming that no Si or carbon is lost during annealing. The original SiC-Ta interface thus roughly coincides with the TaC-Ta_5Si_3:C interface at 1000°C, where the voids are concentrated. There probably is a meaning to this observation, but without knowing which species moves, how in what medium, we cannot identify a specific cause.

REFERENCES (Chapter 5)

1. T. B. Massalski, editor-in-chief, *Binary Alloy Phase Diagrams*, second edition, ASM International, Metal Park, OH, 1990.
2. J. C. Schuster, J. Chim. Phys., 90, 373 (1993).
3. L. Brewer and O. Krikorion, J. Electrochem. Soc., 103, 38 (1956).
4. T. C. Chou, A. Joshi, and J. Wadsworth, J. Vac. Sci. Technol., A9, 1525 (1991).
5. A. Joshi, H. S. Hu, L. Jesion, J. J. Stephens, and J. Wadsworth, Metall. Trans. 21A, 2829 (1990).
6. J. B. Clark, ASTM Trans., 227, 1250 (1963).
7. J. S. Kirkaldy and L. C. Brown, Can. Met. Quart., 2, 89 (1963).
8. F. J. J. van Loo, Prog. Solid St. Chem. 20, 47 (1990).
9. A. G. Evans and J. W. Hutchinson, Int. J. Solids Structures 20, 455 (1984).

Chapter 6
Measurement of Contact Resistivity

6.1 Contact Resistivity Measurement with Circular Patterns

An ohmic metal-semiconductor contact may be defined as a metal-semiconductor interface whose voltage drop is small compared to that which is present in the active region of the device. The parameter that characterizes an ohmic contact is its contact conductivity σ_c, which is the conductance of the contact per unit area. The reciprocal of σ_c, the contact resistivity, ρ_c, is the quantity commonly quoted, usually in units of Ωcm^2. For integrated-circuits techonology, it is important to have reliable methods of measuring the contact resistivity. The subject is thoroughly discussed in Refs. 1 and 2.

A technique based on the transmission line model is widely used because of its convenience. Its simplest implementation is a linear configuration, which requires the fabrication of a structure that confines the current to a one-dimensional flow pattern [3]. An implementation that exploits the circular symmetry of a current that flows out from a point to infinity in a thin conducting sheet eliminates the necessity to fabricate a structure that defines the current pattern [4]. This circular pattern is advantageous for measurement of the contact resistivity of metal films on refractory semicondutors, for example, diamond [5, 6] and SiC [7-9], because the current-confining structure required for the one-dimensional implementation (mesa or geometrically confined doping) cannot be made easily on these refractory semiconductors.

The circular pattern used in the present study and its dimensions are shown in Fig. 6.1a. The contacts are named radially outwards as C0, C1, and C2, representing the inner dot, the intermediate ring, and the outer ring, respectively. The voltage on each contact is correspondently referred to as V_0, V_1, and V_2. Since the contacts are circularly symmetrical, the pattern of current flow between two contacts should be circularly symmetrical when the

contacts are equipotential surfaces. The resistances between the inner two contacts and the outer two contacts, called R_1 and R_2, respectively, can be obtained by measuring the voltage drop between the two contacts with point probes. The contact resistivity is obtained from these two measurements and the circular transmission line model [4].

This picture is correct only *if the bulk resistivity of the metal contact is zero.* In practice, when C0 is grounded (V_0=0), V_1 changes from N to P, as shown schematically in Fig. 6.1b, and is symmetrical with respect to the NOP axis. The difference of V_1(N) and V_1(P) could be as large as 20% of V_1(N), depending on the metal used for the ring contact, its thickness, and the magnitude of the current. A non-constant potential drop is also seen between C1 and C2 when the current passes through these two contacts. If the metal contact is covered by a thick layer of a good conductor such as Au or Al, the potential drop along the ring can be minimized because the resistance for the current that flows in the ring is reduced. If this layer is applied prior to a thermal annealing, it may completely alter the SiC-metal reaction. If the layer is deposited after all the heat treatments, another photolithographic step becomes necessary and compromises the simplicity of the technique.

In the next section, we derive an analytic expression for the angular dependence of the potential distribution of the circular rings when they have finite bulk resistances. When the angular dependence of the potential distribution along a ring is known, the resistance between the contacts that would be measured with a circularly symmetrical current flow, $R_{1,sym}$ and $R_{2\ sym}$, can be extracted. The contact resistivity is then calculated from $R_{1,\ sym}$ and $R_{2\ sym}$ with the circular transmission line model [Ref. 4, Appendix II].

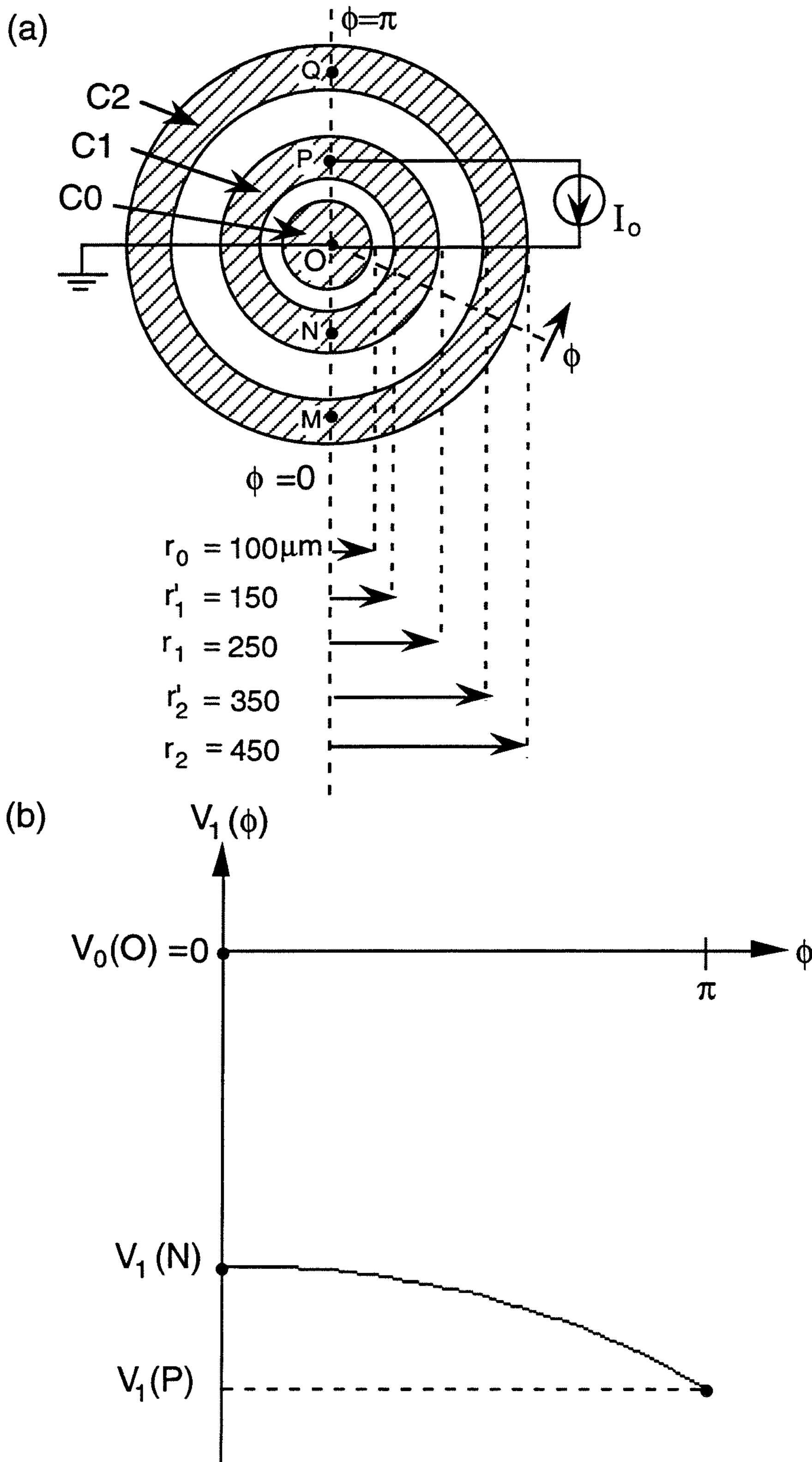

Fig. 6.1 (a) Circular contact pattern used in the present study. (b) The potential distribution, $V_1(\phi)$, along the first ring with the current source set up as shown in (a).

6.2 Effect of the Finite Metal Resistance - A Resistance Network Model

We divide the circular structure into infinitesimal wedges. Each wedge between C0 and C1 and each small sector of C1 are modeled by a resistor as shown in Fig. 6.2a. A polar coordinate is used with the origin at the center of the pattern and $\phi=0$ at the 6 o'clock position if the constant current, I_o, is fed into C1 with a current probe at the 12 o'clock position. We consider two-dimensional current flow only. Let $G_{1,sym}= 1/R_{1,sym}$ be the conductance between C0 and C1 when the current flows circularly symmetrical from C0 to C1. For that case, the conductance of each small wedge between C0 and C1 is G'_1, which is a conductance per radian, and

$$G'_1= G_{1,sym}/2\pi= 1/(2\pi R_{1,sym}). \tag{1}$$

Each small sector of C1 is represented by a small resistor of resistance R'_{m1},

$$R'_{m1}= R_{m1}/2\pi, \tag{2}$$

where R_{m1} is resistance of the whole metal ring for a current that flows along and within the ring.

The resistor network of Fig. 6.2a can be converted to a ladder network by connecting the nodes which are symmetrical to the NOP axis (A and A*, B and B*, ...). The resulting ladder network is shown in Fig. 6.2b and simplified to Fig. 6.2c. When C0 is grounded ($V_0(\phi)=0$, for all ϕ), the voltage drop $V_1(\phi)$ and the current $I_1(\phi)$ now follow the differential equations of variable ϕ for a transmission line,

$$\begin{aligned} \frac{dV_1}{d\phi} &= -I_1(\phi)\frac{R'_{m1}}{2} \\ \frac{dI_1}{d\phi} &= -V_1(\phi)2G'_1 \end{aligned}, \tag{3}$$

with the boundary conditions

$$I_1(0) = 0 \text{ and } I_1(\pi) = I_o . \tag{4}$$

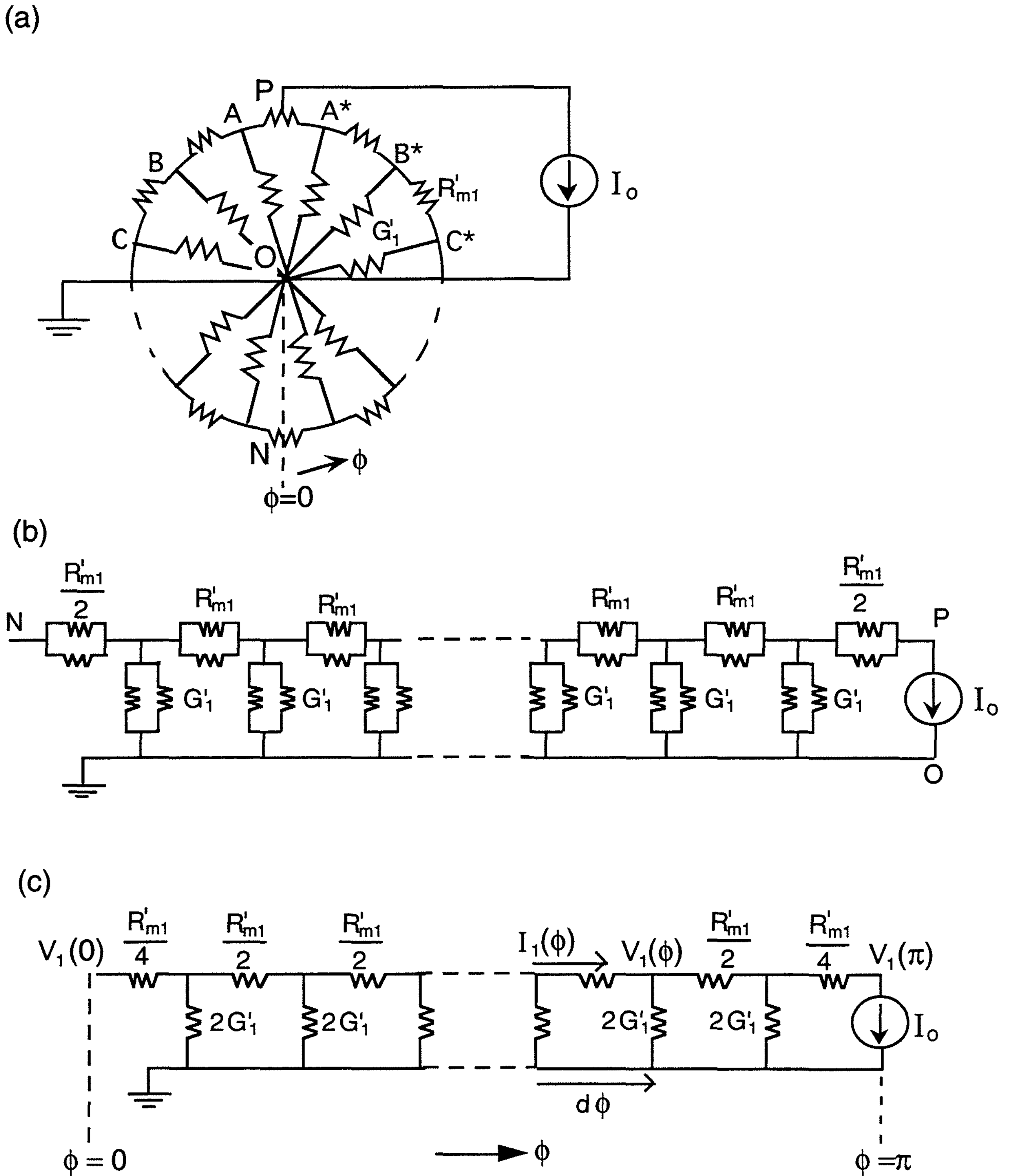

Fig. 6.2 (a) A network of resistors that models the region between the inner dot C0 and the intermediate ring C1 of the circular pattern Fig. 6.1a. (b) and (c) Ladder networks that are equivalent to the circular network of (a).

The solution of the current flow $I_1(\phi)$ is

$$I_1(\phi) = (I_o / \sinh \eta\pi)\sinh \eta\phi \,, \tag{5}$$

where $$\eta^2 = R'_{m1} G'_1 \,. \tag{6}$$

The voltage difference between C1 and C0 is $V_{10}(\phi)=V_1(\phi)-V_0(\phi)$ ($V_0(\phi)=0$)

$$V_{10}(\phi) = V_1(\phi) - V_0(\phi) = -\frac{dI_1}{d\phi}\cdot\left(\frac{1}{2G'_1}\right) = -(\lambda I_o / 2\sinh \eta\pi)\cosh \eta\phi \,, \tag{7}$$

where $$\lambda^2 = R'_{m1} / G'_1 \,. \tag{8}$$

Therefore, the finite resistance of the ring causes the potential defference between C0 and C1 to follow a *cosh* function of angle ϕ. The potential distribution sketched in Fig. 6.1b is in fact, very close to a cosh function.

The average of $V_{10}(\phi)$ is

$$\langle V_{10}\rangle = \frac{1}{\pi}\int_0^{\pi} V_{10}(\phi)d\phi = -(I_o / 2\pi)(\lambda / \eta) = -\frac{I_o}{2\pi G'_1} = -I_o R_{1,sym} = V_{10,sym} \,. \tag{9}$$

From eqs. (7) and (9),

$$V_{10}(\pi) / V_{10}(0) = \cosh \eta\pi \tag{10}$$

and $$V_{10,sym} / V_{10}(0) = \sinh \eta\pi / \eta\pi = \frac{\sinh\left(\cosh^{-1}\left(\frac{V_{10}(\pi)}{V_{10}(0)}\right)\right)}{\cosh^{-1}\left(\frac{V_{10}(\pi)}{V_{10}(0)}\right)} \,. \tag{11}$$

Note that when $R'_{m1} \rightarrow 0$, then $\eta \rightarrow 0$ and $V_{10}(0) = V_{10}(\pi) = V_{10,sym}$. This means that in the limiting case of zero resistance of the ring, the potential on the ring will be a constant.

By defining $R_1(0) = V_{10}(0) / I_o$ and $R_1(\pi) = V_{10}(\pi) / I_o$, the resistance between C0 and C1 in the case of circularly symmetrical current flow thus is

$$R_{1,sym} = V_{10,sym} / I_o = R_1(0)\frac{\sinh\left(\cosh^{-1}\left(\frac{R_1(\pi)}{R_1(0)}\right)\right)}{\cosh^{-1}\left(\frac{R_1(\pi)}{R_1(0)}\right)} \,. \tag{12}$$

Therefore, by the measurements of $R_1(0)$ and $R_1(\pi)$, $R_{1,sym}$ can be extracted from Eq. (12).

To calculate the angular dependence of the potential drop between C1 and C2, a similar circular network of resistors and its equivalent ladder network is used (Fig. 6.3). G'_2 and R'_{m2} have definitions similar to those of G'_1 and R'_{m1}.

$$G'_2 = G_{2,sym}/2\pi = 1/(2\pi R_{2,sym}) \tag{13}$$

$$R'_{m2} = R_{m2}/2\pi \tag{14}$$

The differential equations for the double transmission line shown in Fig. 2b are

$$\begin{aligned} \frac{dV_1}{d\phi} &= -I_1(\phi)\frac{R'_{m1}}{2} \\ \frac{dV_2}{d\phi} &= -I_2(\phi)\frac{R'_{m2}}{2} \\ -\frac{dI_1}{d\phi} = \frac{dI_2}{d\phi} &= -(V_2(\phi)-V_1(\phi))2G'_2 \end{aligned} \tag{15}$$

with boundary conditions of

$$\begin{aligned} I_1(0) = 0, I_1(\pi) = -I_o \\ I_2(0) = 0, I_2(\pi) = I_o \end{aligned} . \tag{16}$$

The solutions for the potential difference between C1 and C2 at angle ϕ is $V_{21}(\phi)$

$$V_{21}(\phi) = V_2(\phi) - V_1(\phi) = -(\lambda' I_o / 2\sinh\eta'\pi)\cosh\eta'\phi \tag{17}$$

where $$\eta'^2 = (R'_{m1} + R'_{m2})G'_2, \quad \lambda'^2 = (R'_{m1} + R'_{m2})/G'_2 . \tag{18}$$

Again, the average of $V_{21}(\phi)$ over ϕ ($0 \le \phi \le \pi$) is equal to the voltage difference between C1 and C2 that would be observed with a circularly symmetrical current flow.

$$\langle V_{21}\rangle = \frac{1}{\pi}\int_0^\pi V_{21}(\phi)d\phi = -(I_o/2\pi)(\lambda'/\eta') = -\frac{I_o}{2\pi G'_2} = -I_o R_{2,sym} = V_{21,sym} \tag{19}$$

(a)

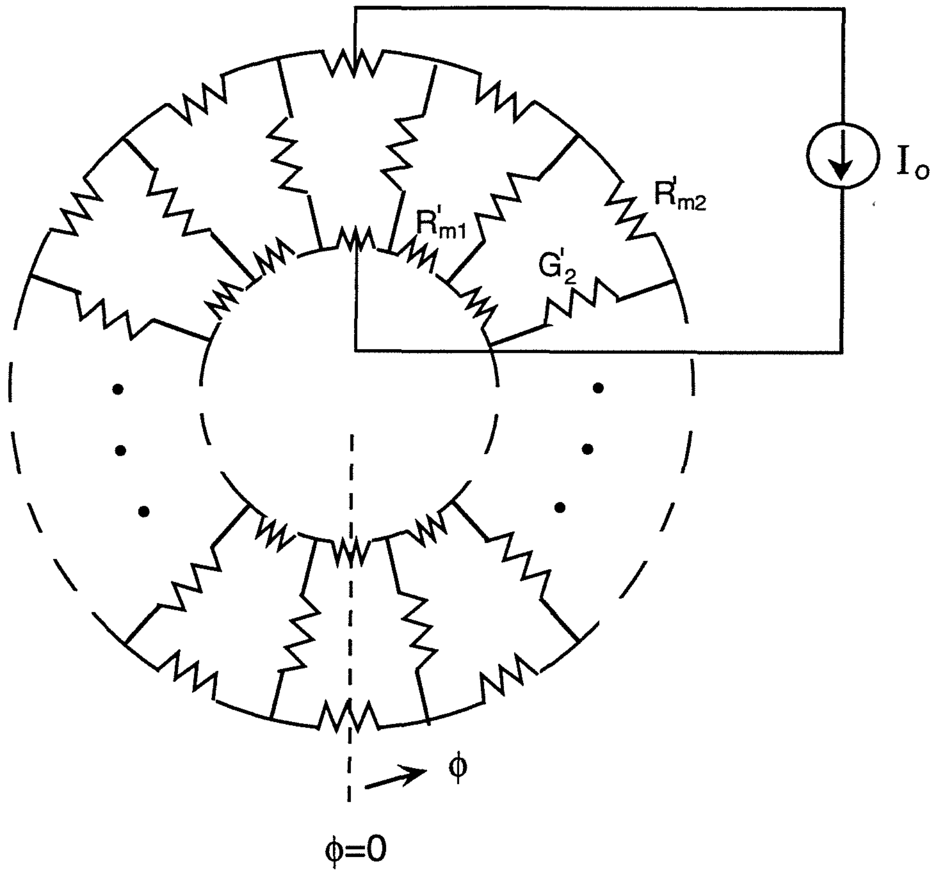

(b)

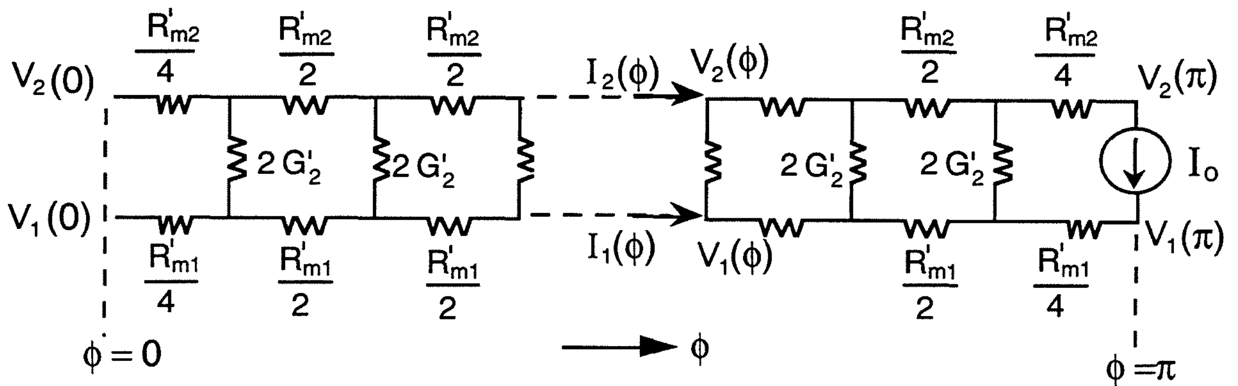

Fig. 6.3 (a) A network of resistors that models the region between the intermediate ring C1 and the outer ring C2 of the circular pattern of Fig. 6.1a. (b) A ladder network that is equivalent to the circular network of (a).

The relations between $V_{21}(0)$, $V_{21}(\pi)$ and $V_{21,sym}$ are

$$V_{21}(\pi) / V_{21}(0) = \cosh \eta' \pi \tag{20}$$

$$V_{21,sym} / V_{21}(0) = \sinh \eta' \pi / \eta' \pi = \frac{\sinh(\cosh^{-1}(\frac{V_{21}(\pi)}{V_{21}(0)}))}{\cosh^{-1}(\frac{V_{21}(\pi)}{V_{21}(0)})} . \tag{21}$$

As $R_{1,sym}$, $R_{2,sym}$ also can be obtained from the measurements of $R_2(0)$ and $R_2(\pi)$ by the definition of $R_2(0) = V_{21}(0) / I_o$ and $R_2(\pi) = V_{21}(\pi) / I_o$, and the equation of

$$R_{2,sym} = V_{21,sym} / I_o = R_2(0) \frac{\sinh(\cosh^{-1}(\frac{R_2(\pi)}{R_2(0)}))}{\cosh^{-1}(\frac{R_2(\pi)}{R_2(0)})} . \tag{22}$$

By measuring the potential difference between C0 and C1, or between C1 and C2, at two particular positions ($\phi=0$ and $\phi=\pi$), $R_{1,sym}$ or $R_{2,sym}$, can be extracted with Eqs. (16) and (22). This procedure is schematically shown in Fig. 6.4.

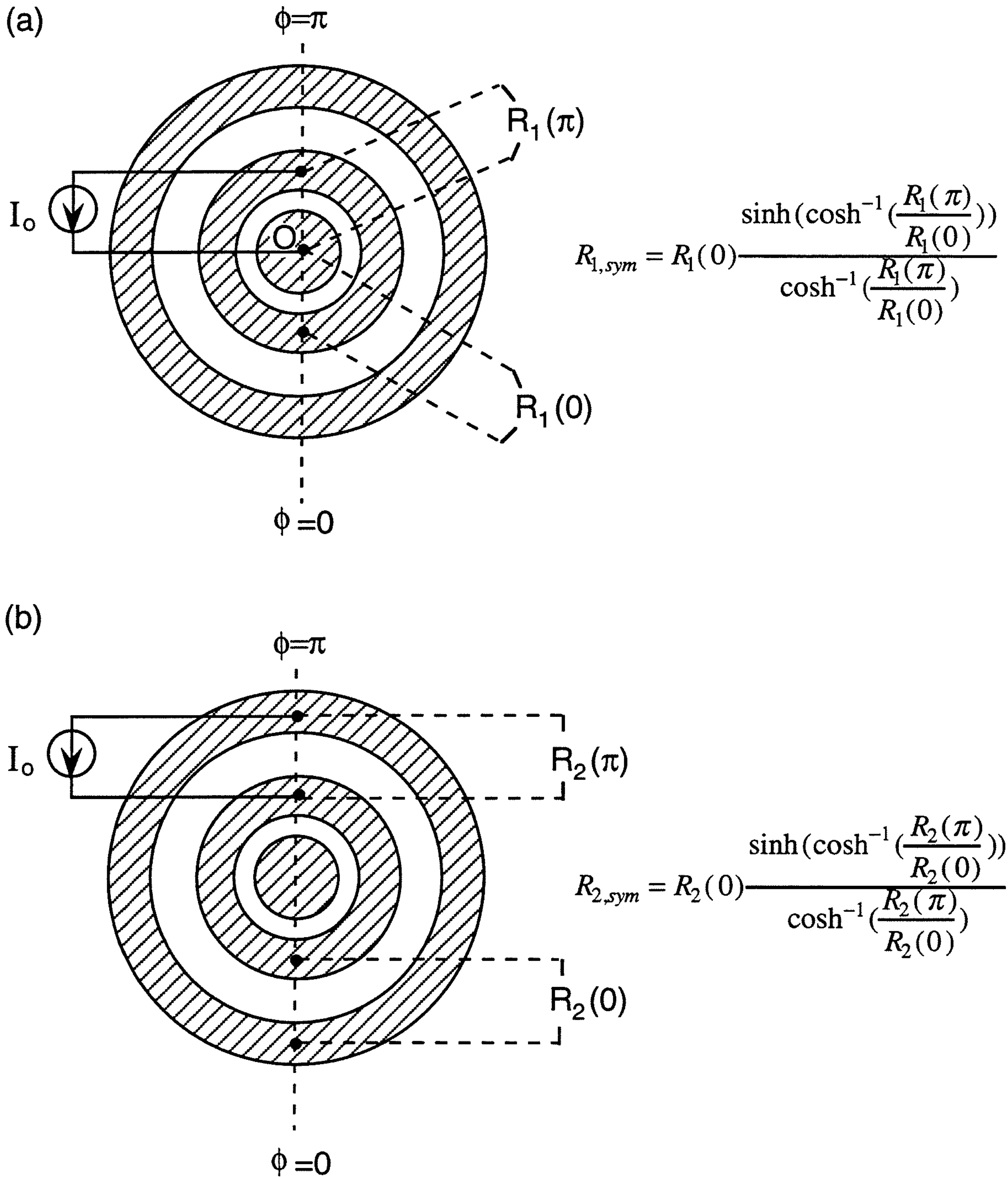

Fig. 6.4 (a) Setup and formulae to obtain $R_{1,sym}$ from the measurement of resistances $R_1(0)$ and $R_1(\pi)$ between C0 and C1. (b) Setup and formulae to obtain $R_{2,sym}$ from the measurement of resistances $R_2(0)$ and $R_2(\pi)$ between C1 and C2.

6.3 Extracting Contact Resistivity With the $R_{1,sym}$ and $R_{2,sym}$ Obtained From the Resistance Network Model

Following the procedure shown in Fig. 6.4, the resistance between the contacts that would be measured with a circularly symmetrical current flow, $R_{1,sym}$ and $R_{2,sym}$, can be obtained. Extraction of the contact resistivity ρ_c from the measured $R_{1,sym}$ and $R_{2,sym}$ requires the circular transmission line model which correlates these quantities by modelling the metal-semiconductor contact as a transmission line.

The original circular transmission line model was proposed by Reeves [4]. In Ref. 4, the sheet resistance of the semiconductor below the contact, R_{sk}, is a quantity distinguished from the normal sheet resistance of the semiconductor between the contact, R_{sh}. There thus are three unknows, ρ_c, R_{sk}, and R_{sh}, in the differential equations implemented by the circular transmission line model. It thus requires three measurements, $R_{1,sym}$, $R_{2,sym}$ and the end resistance R_E (the voltage at the end of the contact divided by the incoming current at the front of the contact), to solve the unknowns. In practice, R_E is generally a small quantity and is difficult to measure accurately due to the finite resistance of the metal contact, even for the small contact pads of linear patterns. Without measuring R_E , ρ_c can be solved from only $R_{1,sym}$ and $R_{2,sym}$ by assuming that R_{sh}=R_{sk}=R_s. The assumption of R_{sh}=R_{sk} is surely valid for the as-deposited metal contacts. For the annealed contacts, the assumption of R_{sh}=R_{sk} is still reasonable as soon as the doped semiconductor layer does not fully react with the metal film.

By assuming R_{sh}=R_{sk}=R_s, a mathematical correlation between $\{R_{1,sym}, R_{2,sym}\}$ and $\{\rho_c, R_s\}$ can be derived following the procedures shown in Ref. 4. However, the resulting functions are quite different from that of between $\{R_{1,sym}, R_{2,sym}, R_E\}$ and $\{\rho_c, R_{sk}, R_{sh}\}$ in Ref. 4. We thus carried out the mathematics of deriving the correlation between $\{R_{1,sym}, R_{2,sym}\}$ and $\{\rho_c, R_s\}$ in Appendix II, which also illustrates the details of the circular

transmission line model. As shown in Appendix II, under the assumption of $R_{sh}=R_{sk}=R_s$, the key quantity to obtain the contact resistivity is the ratio of $R_{1,sym}/R_{2,sym}$. A small uncertainty in $R_{1,sym}/R_{2,sym}$ will result in a significant error of ρ_c and R_s (see Fig. A-II.3), Therefore, without a correct and consistent technique to measure $R_{1,sym}$ and $R_{2,sym}$ in the circular contact pattern, the contact resistivity obtained from the circular transmission model calculation will be very inaccurate. The following is a practice example to demonstrate the importance of the resistance network model on the contact resistivity measurement.

The contact resistivity of the sputter-deposited Ta films on n-type, single crystalline (001) β-SiC are measured with circular patterns. β-SiC substrates of two different doping concentrations are used in the experiment. One is the as-grown SiC with a non-intensional doping concentration of ~10^{17} cm^{-3}. Another one is additionally implanted with nitrogen to a doping concentration of $5\times10^{19}cm^{-3}$ in the first 250 nm. Before the contact patterns were made, the sheet resistances of the substrates are measured by four-point probe and the value is about 250 Ω/sq for the non-intensionally doped SiC and 125 Ω/sq for the nitrogen implanted SiC. The resistances between two contacts are obtained from the slope of the I-V curve (I=1-80 mA). $R_1(0)$, $R_1(\pi)$, $R_2(0)$ and $R_2(\pi)$ are measured following the set up shown in Fig. 6.4. $R_{1,\,sym}$ and $R_{2,\,sym}$ are then calculated from formulae shown in Fig. 6.4 as well. The values of $R_1(0)$, $R_1(\pi)$, $R_2(0)$, $R_2(\pi)$, $R_{1,\,sym}$ and $R_{2,\,sym}$ for the Ta contacts on two different SiC substrates are listed in Table 6.1. ρ_c and R_s are calculated from the R_1/R_2 ratios obtained from $R_1(0)$, $R_1(\pi)$, $R_2(0)$ and $R_2(\pi)$, or from $R_{1,sym}$ and $R_{2,sym}$. The results are listed in Table 6.2 for the non-intensionally doped SiC and Table 6.3 for the nitrogen implanted SiC.

As shown in Tables 6.2 and 6.3, the R_1/R_2 ratios are obtained by $R_1(0)/R_2(\pi)$ or $R_1(\pi)/R_2(\pi)$ are out of range for extracting the ρ_c and R_s (explained in the Appendix II). Therefore, if the R_1 and R_2 were measured by randomly putting down the voltage and current probes, it is quite possible that no ρ_c and R_s values can be obtained from the measured R_1/R_2

value. From $R_1(0)/R_2(0)$ and $R_1(\pi)/R_2(0)$, the calculated ρ_c values are generally greater than that of calculated from $R_{1,\,sym}/R_{2,\,sym}$. The order of difference depends on the materials being used. However, only the R_s extracted from $R_{1,hsym}$ and $R_{2,sym}$ is closed to the value measured by four-point probe before the contact patterns were made. Since the test patterns are not heat treated, the R_s value should not differ from that of the blank substrate. This agreement on the R_s value strongly confirms the applicability of the resistor-network model.

For the Ta contacts on the non-intensionally doped SiC, the ρ_c extracted from $R_{1,sym}/R_{2,sym}$ is about half or one order in magnitude lower than that extracted from $R_1(0)/R_2(0)$ or $R_1(\pi)/R_2(0)$. But, the difference is almost three orders in magnitude for the Ta contacts on the nitrogen implanted SiC. The effect of the finite metal resistance on the nitrogen implanted SiC is more significant than the non-intensionally doped SiC because the sheet resistance of the former is smaller than the latter. Consequently, the deviation between R(0) and R(π) of the nitrogen implanted SiC is lager than that of the non-intensionally doped SiC.

Table 6.1 Measured $R_1(0)$, $R_1(\pi)$, $R_2(0)$ and $R_2(\pi)$, and the calculated $R_{1,\,sym}$ and $R_{2,\,sym}$ for the as-deposited Ta contacts on the non-intensionally doped and nitrogen implanted SiC substrates.

SiC substrate	non-intensionally doped ($n=10^{17}\ cm^{-3}$)		nitrogen implanted ($n=5\times10^{19}\ cm^{-3}$)	
	R1	R2	R1	R2
R(ϕ=0) (Ω)	18.5	12.35	7.35	4.83
R(ϕ=π) (Ω)	20.0	17.95	9.07	10.03
R_{sym} (Ω)	19.0	14.17	7.92	6.47

Table 6.2 ρ_c and R_s calculated from $R_1(0)$, $R_1(\pi)$, $R_2(0)$ and $R_2(\pi)$, or from $R_{1,sym}$ and $R_{2,sym}$ for the as-deposited Ta contacts on the non-intensionally doped SiC (R_{sh} ~ 250 Ω/sq).

	R_1 / R_2	R_s (Ω/sq.)	ρ_c (Ωcm^2)
$R_1(0)/R_2(0)$	1.498	177	3.7×10^{-4}
$R_1(0)/R_2(\pi)$	1.03	—	—
$R_1(\pi)/R_2(0)$	1.619	158	7.7×10^{-4}
$R_1(\pi)/R_2(\pi)$	1.114	—	—
$R_{1,sym}/R_{2,sym}$	1.34	234	8×10^{-5}

("—": R_1/R_2 is out of range)

Table 6.3 ρ_c and R_s calculated from $R_1(0)$, $R_1(\pi)$, $R_2(0)$ and $R_2(\pi)$, or from $R_{1,sym}$ and $R_{2,sym}$ for the as-deposited Ta contacts on the nitrogen implanted SiC (R_{sh} ~ 125 Ω/sq).

	R_1 / R_2	R_s (Ω/sq.)	ρ_c (Ωcm^2)
$R_1(0)/R_2(0)$	1.521	68	2×10^{-4}
$R_1(0)/R_2(\pi)$	0.733	—	—
$R_1(\pi)/R_2(0)$	1.878	49	8×10^{-4}
$R_1(\pi)/R_2(\pi)$	0.904	—	—
$R_{1,sym}/R_{2,sym}$	1.244	119	7×10^{-7}

("—": R_1/R_2 is out of range)

6.4 Contact Resistivities of Re, Pt and Ta Films on n-type β-SiC

We have measured contact resistivities of Re, Pt and Ta films, on both nonintentionally doped and nitrogen-implanted (001) β-SiC substrates, upon annealing in vacuum at 500 and 900 °C for 30 min (also at 1000 and 1100 °C for Ta films on nitrogen-implanted SiC) using a test pattern of concentric contacts from which data were extracted according to the improved transmission line model discussed in previous sections.

The dashed lines in Fig. 6.5 shows the contact resistivity of the 300 nm Re and 320 nm Ta films on the non-intentionally doped β-SiC substrates (carrier concentration ~ 10^{17} cm^{-3}). The 200 nm Pt film yields non-ohmic contacts regardless of the heat treatment. The as-deposited Ta and Re films are ohmic with contact resistivities of 5×10^{-5} Ωcm^2 and 4×10^{-4} Ωcm^2, respectively. Upon annealing at 500 °C for 30 min, the resistivity of Ta increases to 1×10^{-4} Ωcm^2 while that of Re decreases slightly to 2.5×10^{-4} Ωcm^2. Both Ta and Re contacts become non-ohmic after 30 min at 900°C.

On the nitrogen-implanted β-SiC substrates (carrier concentration ~ 5×10^{19} cm^{-3}), the as-deposited Ta, Pt, and Re contacts are all ohmic (Fig. 6.5, solid lines). The contact resistivity of the as-deposited Ta contact is 7×10^{-7} Ωcm^2, stays about the same at 500°C (~5×10^{-7} Ωcm^2) and degrades to 1.6×10^{-6} Ωcm^2 at 900 °C. At 1000 °C for 1 h, the contact resistivity rises yet further to 4.3×10^{-6} Ωcm^2. After annealing at 1100 °C, the I-V measurement is linear, but R_1 or R_2 vary by more than 100% from one pattern to another and some of the R_1/R_2 ratios actually lead to physically meaningless values. The as-deposited Re contact has a high resistivity of 1×10^{-4} Ωcm^2 but decreases to 1×10^{-5} Ωcm^2 at 500 °C and to 1×10^{-5} Ωcm^2 at 900 °C. The contact resistivity of the as-deposited Pt contacts is 6×10^{-6} Ωcm^2 and degrades to 1×10^{-5} Ωcm^2 at 500 °C. The Pt contacts on the nitrogen-implanted β-SiC are no more ohmic when annealed at 900 °C for 30 min.

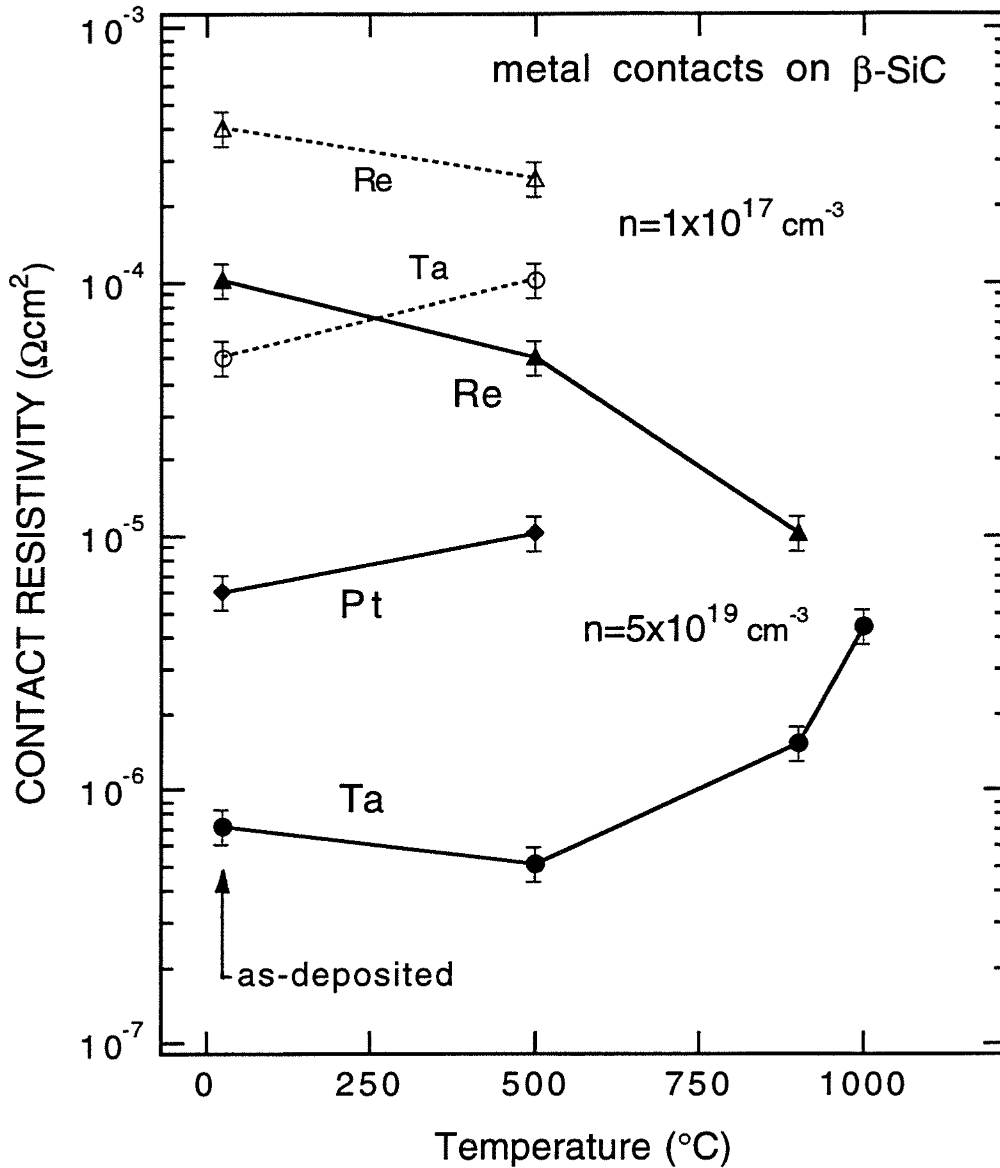

Fig. 6.5 Contact resistivities of films of Re (300 nm) and Ta (320 nm) on non-intentionally doped SiC (dashed lines) and of Re (300 nm), Pt (200 nm) and Ta (320 nm) on nitrogen-implanted SiC (solid lines) as-deposited and after annealing for 30 min in vacuum (1 h for 1000 °C).

6.5 Comparison of Contact Resistivity Results with the Interfacial Reactions Results

Rhenium does not react with SiC up to 1100 °C [Chapter 3]. Based simply on its thermodynamic inertness, the electrical behavior of the Re contact on SiC would be expected not to change with heat treatment, yet major changes are observed. This means that minute changes at the interface can significantly alter the electronic characteristic of the interface. It also means that the following discussion is considered conjectural.

Platinum was found to be a Schottky contact on both β-SiC [10] and 6H-SiC [11] of electron concentration of 10^{16}-10^{17} cm^{-3}. The non-ohmic behavior of the Pt contacts we observed on the non-intentionally doped SiC is consistent with the results in the literature. The Pt contact on the nitrogen-implanted SiC is ohmic, perhaps due to the tunneling across an electronic barrier. Upon annealing at 500 °C, platinum forms an interfacial layer about 45 nm thick of mixed silicide and carbon [Chpater 4]. Both the Pt-silicide and the carbon are in contact with the substrate. This new interface degrades the contact resistivity (Fig. 4). Upon annealing at 900 °C, the phases in the silicide-and-carbon mixed layer become stratified, with a continuous carbon layer in direct contact with SiC. This carbon layer thus results in a non-ohmic contact.

A thin Ta film starts to react with SiC at 900 °C and forms Ta_2C and carbon-stabilized Ta_5Si_3 at the interface [Chpater 5]. A multilayered structure with a laterally uniform TaC layer in contact with the SiC substrate is then formed at 1000 °C. For the Ta films deposited on the nitrogen-implanted SiC, the contact resistivity starts to increase at 900 °C, and increases further at 1000 °C. The reaction at the interface therefore degrades the contact resistivity, but the TaC layer formed at the interface still has quite a low contact resistivity. After annealing 1100 °C, voids of size more than 1 μm are observed in the reacted layer [Chapter 5]. The reacted layer above the voids buckles and forms hillocks on the surface. This irregular

structure of the reacted layer is probably responsible for the erratic resistance measurements we obtained. For the Ta contacts deposited on the non-intentionally doped SiC, the increase of the resistivity upon annealing at 500 °C and non-ohmic behavior at 900 °C cannot be simply explained by the interfacial reactions.

REFERENCES (Chapter 6)

1. S. S. Cohen and G. Sh. Gildenblat, *Metal-Semiconductor Contacts and Devices, VLSI Electronics Microstructure Science*, Vol. 13, edited by N. G. Einspruch, Chap. 4, Academic Press, New York, 1986.
2. D. K. Schroder, *Semiconductor Material and Device Characterization,* Chap. 3, John Wiley and Sons, New York, 1990.
3. H. H. Berger, Solid-St. Electron. 15, 145 (1972).
4. G. K. Reeves, Solid-St. Electron, 21, 801 (1978).
5. C. A. Hewett, J. R. Zeidler, M. J. Taylor, C. R. Zeisse, and K. L. Moazed, in *New Diamond Science and Technology*, p. 1107, Materials Research Society, Pittsburgh, PA, 1991.
6. V. Venkatesan, D. M. Malta, K. Das, and A. M. Belu, J. Appl. Phys. 74, 1179 (1993).
7. J. B. Petit and M. V. Zeller, Mat. Res. Soc. Symp. Proc., Vol. 242, p. 567, Materials Research Society, Pittsburgh, PA, 1992.
8. J. Crofton, J. M. Ferrero, P. A. Barnes, J. R. Williams, M. J. Bozack, C. C. Tin, C. D. Ellis, J. A. Spitznagel, and P. G. McMullin, in *Amorphous and Crystalline Silicon Carbide IV*, edited by C. Y. Yang, M. M. Rahman, and G. L. Harris, p. 176, Springer-Verlag, Berlin, 1992.
9. J. Crofton, P. A. Barnes, J. R. Williams, and J. A. Edmond, Appl. Phys. Lett. 62, 384 (1993).
10. N. A. Papanicolaou, A. Christou, and M. L. Gipe, J. Appl. Phys. 65, 3526 (1989).
11. L. M. Porter, R. C. Glass, R. F. Davis, J. S. Bow, M. J. Kim, and R. W. Carpenter, Mat. Res. Soc. Symp. Proc., Vol. 282, p. 471, 1993.

Chapter 7
Further Thoughts

In this research project, we have established a detailed understanding of the phases that appear, and their interfacial distribution as single crystaline β-SiC reacts with thin metal films upon vacuum annealings at various temperatures. As shown in the thesis, the thermal reactions of the metal-Si-C ternary systems are complex, especially when the metal can form both stable silicides and carbides (e.g., Ta-SiC system). From the metallugical point of view, the next step of investigation will be:

(1) Search for the general pattern of the reaction between SiC and transition metals and its connetion, if any, with the periodic table of elements.

(2) Study the evolution of a reaction at a constant temperature for various durations.

(3) Try to determine activation energies of the growth of the whole reaction zone as well as each sublayers when a multilayered structure exists.

(4) Perform maker experiments to clarify what species move.

(5) Compare thin-film and bulk reaction couples.

Also, the chemical reactions at the metal-SiC interface discussed in this thesis strictly apply only to single crystal β-SiC substrate. It would be interesting to establish if, and if so, how they would differ for other polytypes, for polycrystalline, and for amorphous SiC substrates. The change of the internal energy and entropy between polymorphic phases are ordinarily quite small, so that the reaction of polytypes other than β-SiC should be similar. For the polycrystalline and amorphous SiC substrates, the presence of grain boundaries and the increased internal energy of SiC may also alter the outcome.

For the electrical behaviour, minor changes at the SiC/metal or SiC/compound interface can have major effects on the electronic properties. It is clear that detailed studies

on the atomic level of the interface are required to further the understanding of the electronic characteristics of metal contacts on SiC. In this respect, SiC follows the general patterns observed for all semiconductors.

Unlike the sensitivity of the electronic characteristic to the minute atomic structure, the mechanical behavior of the SiC-metal joints should have a significant and clear connection with the phases and their microstructures present at the interface. Stress, adhesion and ductivity tests on the metal-SiC interface are interesting not only for metal-matrix composites application, but for the microelectronics application as well.

Summary and Conclusions

Experiments and thermodynamic theory both prove that Re does not react with SiC. This finding holds at least up to 1100 °C.

The solid-state reaction that evolves between a thin Pt film and a single-crystalline (001) β–SiC substrate upon annealing at various temperature is complex. A thin amorphous interlayer forms between Pt and SiC at 400 °C. At 500 °C and above, the reaction develops an upper silicide layer and a lower mixed carbon and silicide layer. Both Pt and Si diffuse during the reaction. Experimental results indicate that to reach the final metallurgical stable state by furnace annealing, it may require prolonged heat treatments at temperatures below that of eutectic at 980 °C.

For heat treatment of 1 h in vacuum, a tantalum film begins to react with a (001) β-SiC substrate at 900 °C and maintains a sharp, planar interface up to 1000 °C. The layer in immediate contact with SiC at that point is polycrystalline TaC. This compound and that time-temperature window of thermal annealing are thus those of particular interest for electronic applications. The presence of voids within the reacted layer at 1100 °C may have deleterious consequences for the mechanical properties of the contact that needs to be addressed.

Contact resistivities of thin metal films on SiC depend on the carrier concentration of the SiC substrate, on the metal species, and on thermal annealing. The doping level of the SiC substrate is the primary factor in determining the ohmicity of the contacts. In this respect SiC acts like Si, which suggests that similar barrier height and depletion-layer concepts may apply in both cases. With this assumption, our results would indicate that carbon has an electronic barrier to SiC that is higher than those of Pt or Pt-silicides, and that Ta has the lowest, and that

it is less than those of its carbides. The case of Re shows, however, that minor changes at the SiC-metal interface can have major effects on its electronic properties. In this respect also, our results follow a pattern that is typical for all metal-semiconductor interfaces.

Appendix I

Work published by Jen-Sue Chen

1. J. S. Chen, E. Kolawa, C. M. Garland, and M-A. Nicolet, *Epitaxial growth of GaAs by solid-phase transport*, Appl. Phys. Lett. 59, 1597 (1991).

2. J. S. Chen, E. Kolawa, R. P. Ruiz, and M-A. Nicolet, *Interfacial reactions of Ag thin films on (001) GaAs*, Mat. Res. Soc. Symp. Proc. Vol. 221, p. 355, Material Research Society, Pittsburgh, 1991.

3. J. S. Chen, E. Kolawa, C. M. Garland, M-A. Nicolet, and R. P. Ruiz, *Microstructure of polycrystalline* $CuInSe_2$*/Cd(Zn)S heterojunction solar cells*, Thin Solid Films 219, 183 (1992).

4. J. S. Chen, E. Kolawa, R. P. Ruiz, and M-A. Nicolet, *Stable Pt/Ge/Au ohmic contact to n-GaAs with a Ta-Si-N diffusion barrier*, Mat. Res. Soc. Symp. Proc. Vol. 300, p. 255, Materials Research Society, Pittsburg, 1993.

5. J. S. Chen, E. Kolawa, M-A. Nicolet, and F. S. Pool, *Thermal reaction of Ta thin films with polycrystalline diamond*, Thin Solid Films 236, 72 (1993).

6. J. S. Chen, E. Kolawa, M-A. Nicolet, L. Baud, C. Jaussaud, R. Madar, and C. Bernard, *Stability of rhenium thin films on single crystal (001)* β*-SiC*, J. Appl. Phys. 75, 897 (1994).

7. J. S. Chen, E. Kolawa, and M-A. Nicolet, *Interfacial reaction of Pt thin films on single-crystal (001)* β*-SiC*, 1993 Microbeam Analysis Society Annual Meeting.

8. J. S. Chen, E. Kolawa, M-A. Nicolet, R. P. Ruiz, L. Baud, C. Jaussaud, and R. Madar, *Solid-state reaction of Pt thin film with single-crystal (001)* β*-SiC*, J. Mat. Res., 9, 648 (1994).

9. J. S. Chen, E. Kolawa, M-A. Nicolet, and R. P. Ruiz, *Ohmic contacts to n-GaAs with a Pt/Ge/Au contacting layer and a Ta-Si-N barrier: electrical and metallurgical characteristics*, J. Appl. Phys. 75, 7373 (1994).

10. J. S. Chen, E. Kolawa, M-A. Nicolet, R. P. Ruiz, L. Baud, C. Jaussaud, and R. Madar, *Reaction of Ta thin film with single-crystal (001) β-SiC*, to be published in J. Appl. Phys., August, 1994.

11. J. S. Chen, A. Bächli, M-A. Nicolet, L. Baud, C. Jaussaud, and R. Madar, *Ta, Re, and Pt ohmic contacts to n-type β-SiC*, European Materials Research Society Spring Meeting, Strasbourg, France, May 24-27, 1994. To be published in Materials Science and Engineering B.

12. J. S. Chen, A. Bächli, M-A. Nicolet, L. Baud, C. Jaussaud, and R. Madar, *Solid-state reaction of Ti thin film with single crystalline (001) β-SiC*, High-Temp. Electronics Conference, Charlotte, NC, June 5-10, 1994.

13. J. S. Chen, E. Kolawa, and M-A. Nicolet, *Cu/In deposited at room temperature: morphology, phases and reactions*, Solar Cells 30, 451 (1991).

14. E. Kolawa, P. J. Pokela, J. S. Reid, J. S. Chen, M-A. Nicolet, and R. Ruiz, *Sputtered Ta-Si-N diffusion barriers in Cu metallizations for Si*, IEEE Electron Device Letters, 12, 309 (1991).

15. E. Kolawa, J. S. Chen, J. S. Reid, P. J. Pokela, and M-A. Nicolet, *Ta based Diffusion barrier in Si/Cu metallizations*, J. Appl. Phys. 70, 1369 (1991).

16. E. Kolawa, P. J. Pokela, J. S. Reid, J. S. Chen, and M-A. Nicolet, *Amorphous Ta-Si-N Diffusion Barriers in Si/Al and Si/Cu metallizations,* J. Appl. Surf. Sci. 53, 373 (1991).

17. J. S. Reis, J. S. Chen, E. Kolawa, A. Sherman, M-A. Nicolet, and R. Ruiz, *A comparison between CVD and sputtered TiN diffusion barriers in Cu and Al metallizations for Si*, Mat. Res. Soc. Symp. Proc. 221 (1991).

18. S. Raud, J. S. Chen, and M-A. Nicolet, *Influence of oxygen on diffusion in the Cu/Mo/Au system*, Appl. Phys. A 52, 151 (1991).

19. W-S. Liu, J. S. Chen, M-A. Nicolet, V. Arbet-Engels, and K. L. Wang, *Instability of a* $Ge_xSi_{1-x}O_2$ *film on* Ge_xSi_{1-x}, J. Appl. Phys. 72, 4444 (1992).

20. J. S. Reid, R. P. Ruiz, E. Kolawa, J. S. Chen, J. Madok, and M-A. Nicolet, *Ta-Si-N and Si_3N_4 encapsulants for InP*, Mat. Res. Soc. Symp. Proc. 262, 1079 (1992).

21. W. S. Liu, J. S. Chen, and M-A. Nicolet, *Nanocrystalline Ge in SiO_2 by annealing of $Ge_xSi_{1-x}O_2$ in hydrogen*, Appl. Phys. Lett. 62, 3321 (1993).

22. W. S. Liu, J. S. Chen, D. Y. C. Lie, and M-A. Nicolet, *A Ge epilayer of high quality on a Si substrate by solid phase epitaxy*, Appl. Phys. Lett. 63, 1405 (1993).

23. X. Sun, E. Kolawa, J. S. Chen, J. S. Reid, and M-A. Nicolet, *Properties of reactively sputter-deposited Ta-N thin films*, Thin Solid Films 236, 347 (1993).

24. A. Bächli, J. S. Chen, R. P. Ruiz, and M-A. Nicolet, *Solid-state reaction of Tungsten thin films with polycrystalline diamond*, Materials Research Society, 1994 spring meeting.

25. A. Bächli, J. S. Chen, R. P. Ruiz, and M-A. Nicolet, *Solid-state reaction of thin Mo films with polycrystalline diamond*, High-Temp. Electronics Conference, Charlotte, NC, 1994.

Appendix II

Contact Resistivity Measurement Using a Circular Transmission Line Model of Homogeneous Substrate Sheet Resistance

As mentioned in Chapter 6, the contact resistivity ρ_c can be extracted from the measured resistance between the circular contacts ($R_{1,sym}$, $R_{2,sym}$) by applying the circular transmission line model. In this appendix, the mathematical correlation between "$R_{1,sym}$, $R_{2,sym}$" and "ρ_c, R_s" is derived using circular transmission line model with the assumption that the semiconductor substrate has a unique value of sheet resistance either under (R_{sk}) or between (R_{sh}) the contacts, i.e., $\mathbf{R_{sh}=R_{sk}=R_s}$.

In Fig. A-II.1, the cross section of the circular contact pattern shows that the resistance between two contacts is composed of the bulk semiconductor resistance between the contacts and two contact resistances at the metal-semiconductor interface.

$$R_{1,sym} = R_A + (R_{C0} + R'_{C1}) \tag{A-II.1}$$

$$R_{2,sym} = R_B + (R_{C1} + R'_{C2}) \tag{A-II.2}$$

R_A and R_B are the resistance of the bulk semiconductor between the contacts,

$$R_A = \frac{R_s}{2\pi}\ln\frac{r_1'}{r_0} \quad and \quad R_B = \frac{R_s}{2\pi}\ln\frac{r_2'}{r_1}\ . \tag{A-II.3}$$

The equivalent circuits for circular contacts implemented by the transmission line model is schematically shown in Fig. A-II.2. R_{C0}, R'_{C1}, R_{C1} and R'_{C2} are obtained from the circular transmission line model and are functions of the contact resistance ρ_c and the sheet resistance of the semiconductor R_s. The series resistance element under the contact becomes $\frac{R_s \cdot dx}{2\pi x}$ and the conductance element is $\frac{2\pi x \cdot dx}{\rho_c}$. The basic transmission line equations are

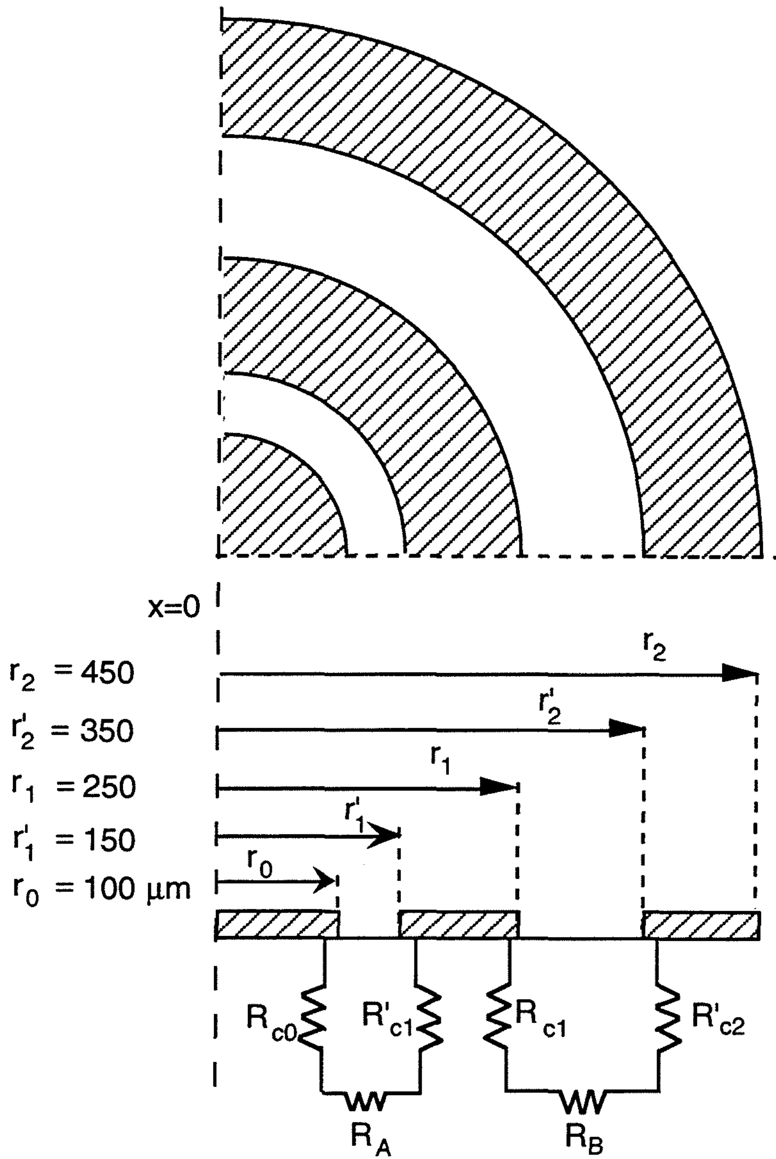

Fig. A-II.1 The circular contact pattern (one quarter) and its cross section showing the dimensions and the resistance conponents.

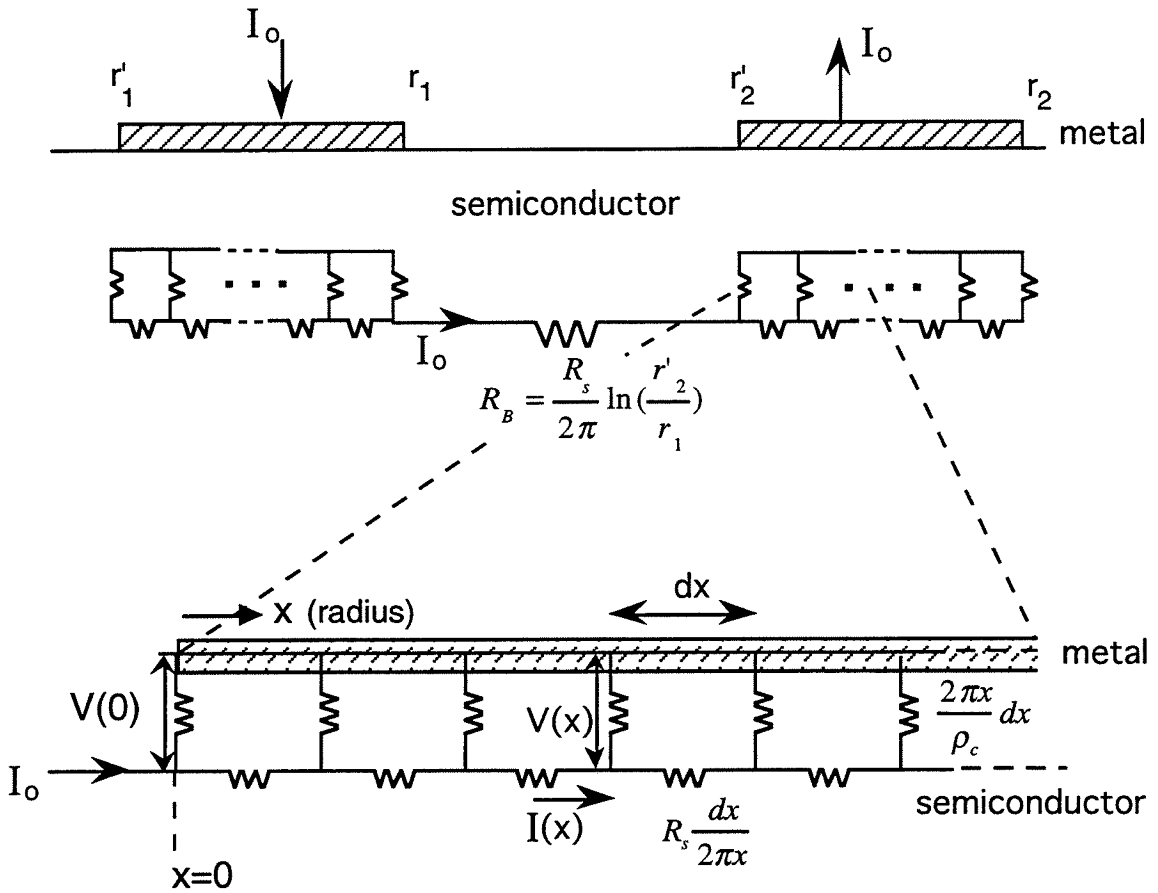

Fig. A-II.2 The equivalent circuits of the metal-semiconductor contact implemented by the circular transmission model.

$$\frac{dV}{dx} = -\frac{I(x)R_s}{2\pi x} \quad and \quad \frac{dI}{dx} = -\frac{V(x)2\pi x}{\rho_c}, \qquad \text{(A-II.4)}$$

where I(x) and V(x) represent the current flowing beneath the contact at x and the voltage drop across the contact interface at x (see Fig. A-II.2).

The solution to the differential equation of V(x) is

$$V(x) = aI_0(\alpha x) + bK_0(\alpha x) \qquad \text{(A-II.5)}$$

where $\alpha^2 = R_s/\rho_c$; I_0 and K_0 are zeroth order modified Bessel functions of the first and second kind, respectively. I(x) is obtained simply by differentiating V(x).

By setting the appropriate boundaries to the solutions of V(x) and I(x), R_{C0}, R'_{C1}, R_{C1} and R'_{C2} are then formulated as functions of α ($\alpha^2 = R_s/\rho_c$) and R_s (see details in Ref. 1). After knowing R_{C0}, R'_{C1}, R_{C1} and R'_{C2}, $R_{1,sym}$ and $R_{2,sym}$ can be formulated as

$$R_{1,sym} = \frac{R_s}{2\pi}\ln\frac{r_1'}{r_0} + \frac{R_s}{2\pi\alpha r_0}[E(r_0) + \frac{r_0}{r_1'}\cdot\frac{A(r_1,r_1')}{C(r_1,r_1')}] \qquad \text{(A-II.6)}$$

$$R_{2,sym} = \frac{R_s}{2\pi}\ln\frac{r_2'}{r_1} + \frac{R_s}{2\pi\alpha r_0}[\frac{r_0}{r_1}\cdot\frac{B(r_1,r_1')}{C(r_1,r_1')} + \frac{r_0}{r_2'}\cdot\frac{A(r_2,r_2')}{C(r_2,r_2')}] \qquad \text{(A-II.7)}$$

where A, B, C, and E stand for some combinations of modified Bessel functions

$A(r, x)=I_1(\alpha r)\ K_0(\alpha x) + I_0(\alpha x)\ K_1(\alpha r)$

$B(r, x)=I_1(\alpha x)\ K_0(\alpha r) + I_0(\alpha r)\ K_1(\alpha x)$

$C(r, x)=I_1(\alpha r)\ K_1(\alpha x) - I_1(\alpha x)\ K_1(\alpha r)$

$E(r)=I_0(\alpha r)\ /\ I_1(\alpha r)$.

The unknown R_s is eliminated when $R_{1,sym}$ is divided by $R_{2,sym}$.

$$\frac{R_{1,sym}}{R_{2,sym}} = \phi'(\alpha r_0) = \frac{\frac{1}{2\pi\alpha r_0}[E(r_0) + \frac{r_0}{r_1'}\cdot\frac{A(r_1,r_1')}{C(r_1,r_1')}] + \frac{1}{2\pi}\ln\frac{r_1'}{r_0}}{\frac{1}{2\pi\alpha r_0}[\frac{r_0}{r_1}\cdot\frac{B(r_1,r_1')}{C(r_1,r_1')} + \frac{r_0}{r_2'}\cdot\frac{A(r_2,r_2')}{C(r_2,r_2')}] + \frac{1}{2\pi}\ln\frac{r_2'}{r_1}}. \qquad \text{(A-II.8)}$$

$\phi'(\alpha r_0)$ is a function of αr_0 and decreases monotonically with the increasing of α. Fig. A-II.3a shows the plot of $\phi'(\alpha r_0)$ vs. αr_0 for r_0, r'_1, r_1, r'_2 and r_2 of the values shown in Fig. A-II.1. From $\phi'(\alpha r_0)$, one can obtain α when $R_{1,sym}/R_{2,sym}$ is measured. Note that when the contact resistivity approaches zero, $R_{1,sym}$ and $R_{2,sym}$ have contributions from the resistance of the semiconductor only. Therefore, if $\rho_c \to 0$, then $\alpha \to \infty$ and

$$\lim_{\alpha \to \infty} \phi'(\alpha r_0) = (\ln \frac{r'_1}{r_0}) / (\ln \frac{r'_2}{r_1}) = 1.205 \qquad \text{(A-II.9)}$$

(for r_0=100 μm, r'_1=150 μm, r_1=250 μm, r'_2=350 μm and r_2=450 μm).

Any measurement resulting in a value of $R_{1,sym}/R_{2,sym}$ smaller than 1.205 is thus physically meaningless.

From Eq. (A-II.6),

$$\frac{R_{1,sym} 2\pi}{R_s} = \Delta'(\alpha r_0) = \frac{1}{\alpha r_0}[E(r_0) + \frac{r_0}{r_1} \cdot \frac{A(r_1, r'_1)}{C(r_1, r'_1)}] + \ln \frac{r'_1}{r_0}. \qquad \text{(A-II.10)}$$

Since $\alpha^2 = R_s/\rho_c$, Eq. (A–II.10) can be rewritten as

$$\frac{\rho_c}{R_{1,sym}} = \frac{2\pi}{\Delta'(\alpha r_0)\alpha^2} = \theta'(\alpha r_0). \qquad \text{(A-II.11)}$$

$\theta'(\alpha r_0)$ is also a function of αr_0 and decreases monotonically with the increasing of α. From the measured $R_{1,sym}/R_{2,sym}$, the solution of α is obtained from $\phi'(\alpha r_0)$ and $\theta'(\alpha r_0)$ is also known. ρ_c is thus obtained from the product of $R_{1,sym} \cdot \theta'(\alpha r_0)$. Fig. A-II.3b shows the plot of $\rho_c = R_{1,sym} \cdot \theta'(\alpha r_0)$ vs. αr_0, for $R_{1,sym}$=5 Ω and $R_{1,sym}$=20 Ω. Comparing Fig. A-II.3a and Fig. A-II.3b, one sees the dramatic change in ρ_c, when $R_{1,sym}/R_{2,sym}$ varies. Therefore, if $R_{1,sym}$ and $R_{2,sym}$ are not measured correctly, there could be an error of one to three orders of magnitude for the calculated ρ_c.

REFERENCE

1. G. K. Reeves, Solid-State Electronic 23, 487 (1980).

Captions for figures on next page:

Fig. A-II.3 (a) The plot of function $\phi'(=R_1/R_2)$ vs. the parameter αr_0.

(b) The plot of function $R_1\theta'(=\rho_c)$ vs. the parameter αr_0.

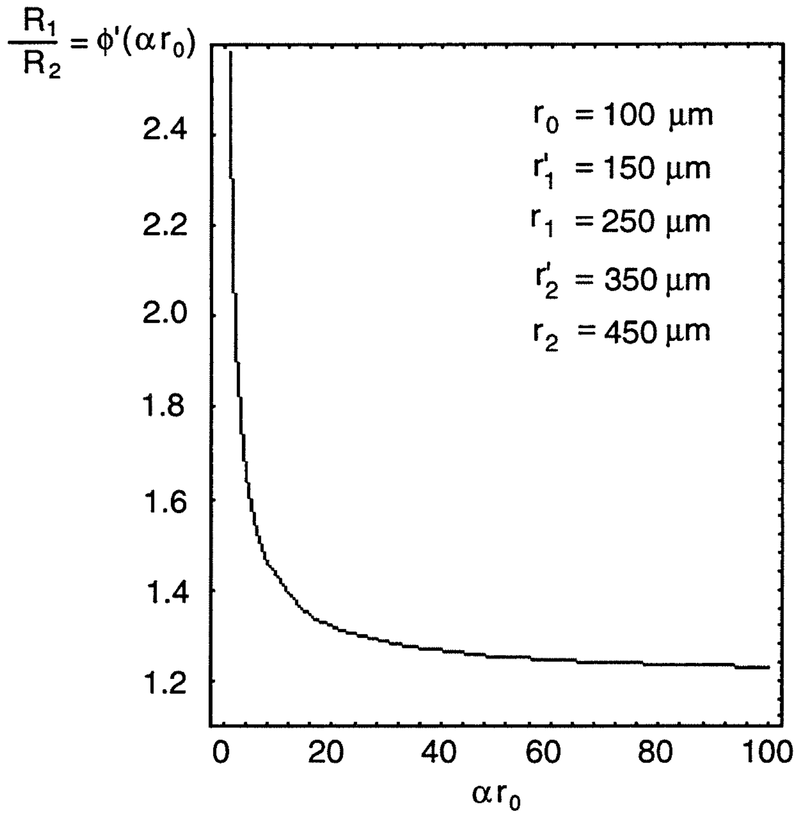
$\frac{R_1}{R_2} = \phi'(\alpha r_0)$
2.4
2.2
2.0
1.8
1.6
1.4
1.2
r_0 = 100 μm
r'_1 = 150 μm
r_1 = 250 μm
r'_2 = 350 μm
r_2 = 450 μm
0
20
40
60
80
100
αr_0

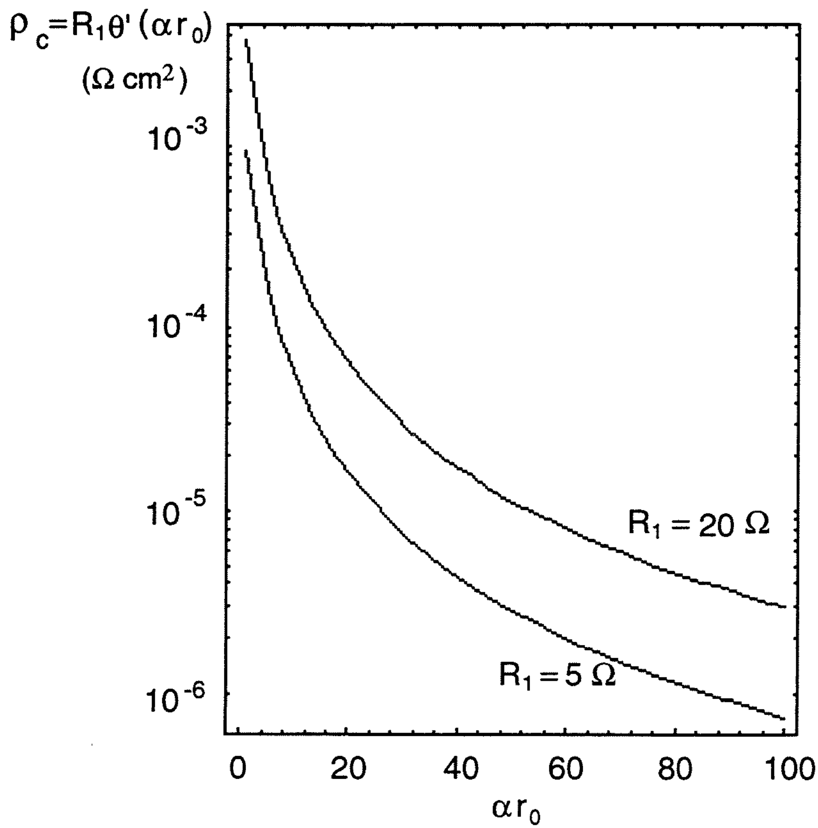
$\rho_c = R_1\theta'(\alpha r_0)$
(Ω cm^2)
10^{-3}
10^{-4}
10^{-5}
10^{-6}
$R_1 = 20\ \Omega$
$R_1 = 5\ \Omega$
0
20
40
60
80
100
αr_0